



Mid-infrared Supercontinuum light sources For food control applications

Kwarkye, Kyei

Publication date:
2021

Document Version
Publisher's PDF, also known as Version of record

[Link back to DTU Orbit](#)

Citation (APA):
Kwarkye, K. (2021). *Mid-infrared Supercontinuum light sources For food control applications*. Technical University of Denmark.

General rights

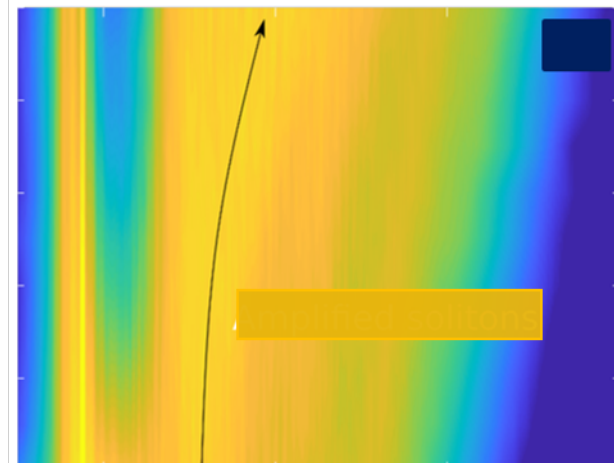
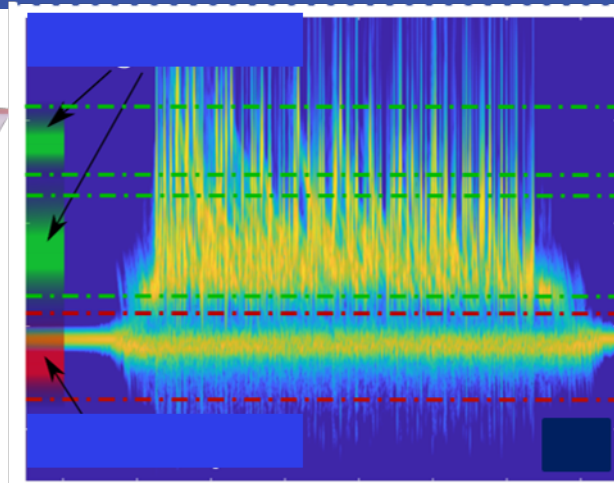
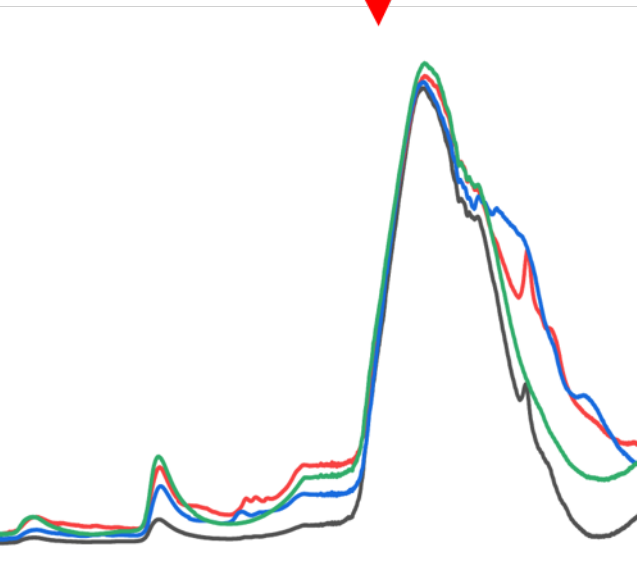
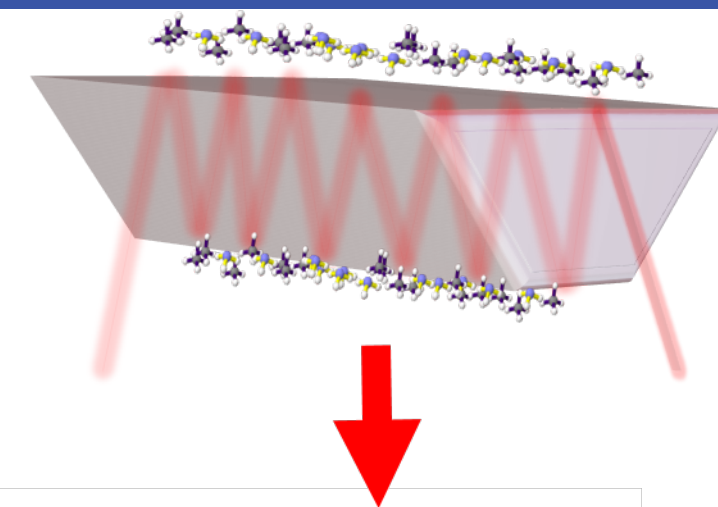
Copyright and moral rights for the publications made accessible in the public portal are retained by the authors and/or other copyright owners and it is a condition of accessing publications that users recognise and abide by the legal requirements associated with these rights.

- Users may download and print one copy of any publication from the public portal for the purpose of private study or research.
- You may not further distribute the material or use it for any profit-making activity or commercial gain
- You may freely distribute the URL identifying the publication in the public portal

If you believe that this document breaches copyright please contact us providing details, and we will remove access to the work immediately and investigate your claim.

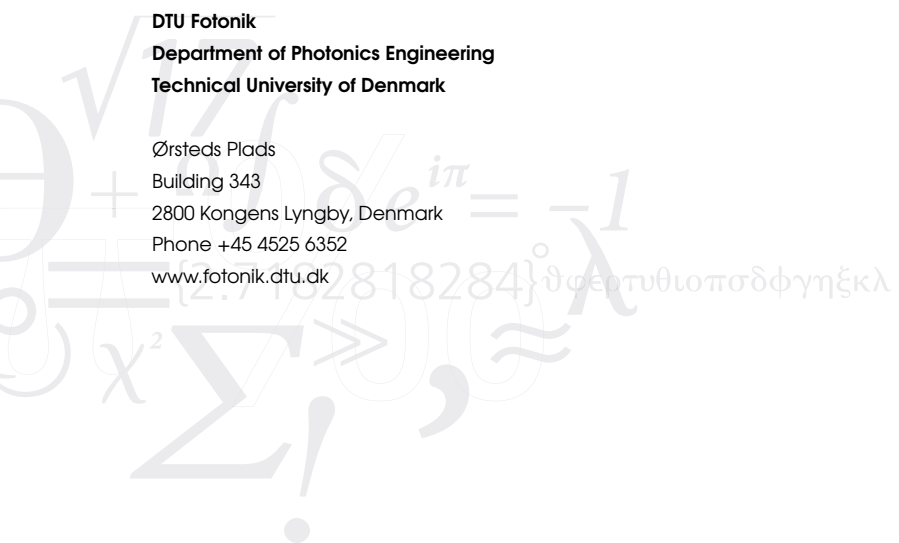
Mid-infrared Supercontinuum light sources For food control applications

Ph.D. Thesis
Kyei Kwarkye



DTU Fotonik
Department of Photonics Engineering
Technical University of Denmark

Ørsted's Plads
Building 343
2800 Kongens Lyngby, Denmark
Phone +45 4525 6352
www.fotonik.dtu.dk



Summary

The advent of spectroscopy by Sir Isaac Newton by observing that white light from the sun can be separated into its constituent colors has found many applications in Scientific research. This observation has been so crucial in fields like color vision and thus, we can say color discrimination and vision is a crude form of spectroscopy. Spectroscopy can simply be described as the absorption of electromagnetic spectral components after interaction with a sample. The inception of spectroscopy has mostly been used to study absorption, scattering, and emission of a limited portion (ultraviolet, visible, infrared) of the broad electromagnetic spectrum but has been expanded to include other components (X-rays, microwaves radio waves) as well as energetic particles like electrons and ions. The infrared part of the electromagnetic spectrum offers a unique advantage as most molecules exhibit distinct absorption fingerprints in this region. The current configuration to probe such absorption fingerprints require broadband thermal light sources whose brightness is much lower especially in the infrared region and also not being spatially coherent. These two disadvantages limit the manipulation of light from these emitters for applications that require simple but efficient instrumentation. This dissertation presents a much more convenient technique of generating broadband, high power, compact light source from the tip of an optical fiber in a process known as supercontinuum generation.

Supercontinuum generation relies on an intense narrow linewidth laser to generate new colors of light after propagation through an optical fiber. This novel process relies on complex nonlinear processes as well as absorption emission processes provided by the specialty fibers used in the generation. Scaling the bandwidth, making an all compact, and improving the noise dynamics of supercontinuum sources has been a major challenge due to the complex processes leading to the generation and inherent limitations of the medium in which the spectrum is being generated. In this work, we present the theory of supercontinuum generation as well as a novel cascading technique to scale up the bandwidth and average power whiles we reduce the relative intensity noise of the spectrum generated. We find the appropriate pumping scheme relevant for improving the supercontinuum light generated. We also show a compact supercontinuum light source which extends the spectrum far into the mid-infrared to approximately $10\ \mu\text{m}$. The supercontinuum source is finally applied in spectroscopy to monitor food adulteration.

Dansk Resumé (Danish Summary)

Fremkomsten af spektroskopi af Sir Isaac Newton ved at observere, at hvidt lys fra solen kan adskilles i dets sammensatte farver, har fundet mange anvendelser i videnskabelig forskning. Denne observation har været afgørende inden for områder som farvesyn, og derfor kan vi sige, at farvediskrimination og syn er en rå form for spektroskopi. Spektroskopi kan beskrives som absorptionen af elektromagnetiske spektrale komponenter efter interaktion med en prøve. Fra første færd er spektroskopi for det meste blevet brugt til at studere absorption, spredning og emission i en begrænset del (ultraviolet, synlig, infrarød) af det brede elektromagnetiske spektrum, men er blevet udvidet til at omfatte andre komponenter (røntgenstråler, mikrobølgeradiobølger) såvel som energiske partikler som elektroner og ioner. Den infrarøde del af det elektromagnetiske spektrum giver en unik fordel, da de fleste molekyler udviser forskellige absorptionsfingeraftryk i denne region. Den nuværende konfiguration til at undersøge sådanne absorptionsfingeraftryk kræver bredbandede, termiske lyskilder, hvis lysstyrke er meget lav, især i det infrarøde område og heller ikke er rumligt kohærent. Disse to ulemper begrænser manipulationen af lys fra disse lyskilder til applikationer, der kræver enkel, men effektiv instrumentering. Denne afhandling præsenterer en meget mere bekvem teknik til at generere en bredbåndet, kompakt lyskilde med høj effekt fra spidsen af en optisk fiber i en proces kendt som superkontinuumgenerering.

Superkontinuumgenerering er afhængig af en laser med smal linjebredde og høj effekt til at generere nye farver af lys efter udbredelse gennem en optisk fiber. Denne nye proces er afhængig af komplekse ikke-lineære processer såvel som absorptions- og emissionsprocesser i de specialfibre, der anvendes. At øge båndbredden, gøre laseren helt kompakt og forbedre støjdynamikken i superkontinuumkilder er en stor udfordring på grund af de komplekse processer, der skaber superkontinuet samt iboende begrænsninger af mediet, hvor spektret genereres. I denne afhandling præsenterer vi teorien bag superkontinuumgenerering samt en ny kaskadeteknik til at skalere båndbredden og gennemsnitseffekten, mens vi reducerer den relative intensitetsstøj fra det genererede spektrum. Vi finder den passende sammensætning af pumpelaserer, der er relevant for at forbedre det genererede superkontinuumlys. Vi demonstrerer også en kompakt superkontinuum lyskilde, der udvider spektret langt ind i det midt-infrarøde område til ca. $10 \mu m$. Superkontinuumkilden anvendes endelig i spektroskopi til overvågning af forfalskning af fødevarer.

Preface

This dissertation is presented to the P.h.D. school of the Department of Photonics Engineering in partial fulfilment for obtaining a P.h.D. degree from the Technical University of Denmark.

The title of the dissertation is Mid-infrared supercontinuum light sources for food control applications and it documents the research carried out at the Department of Photonics Engineering within the period June 2017 to December 2020. This work has been undertaken with supervisions from Professor Ole Bang (Group leader of the fiber sensors and supercontinuum group) as main supervisor, Dr. Christian Rosenberg Petersen as my co-supervisor. The project is part of the larger consortium for developing novel supercontinuum light sources from UV into infrared region (SUPUVIR). The project has received funding from the European Union's Horizon 2020 research and Innovation program under the Marie Skłodowska-Curie grant agreement No: 722380. The project partners are NKT Photonics, University of Copenhagen, Radboud University and Tampere University of Technology.

Kongens Lyngby, December 17, 2020

A handwritten signature in black ink, appearing to read 'Kyei Kwarkye'. The signature is stylized and somewhat abstract, with a vertical line on the left and several loops and strokes on the right.

Kyei Kwarkye

Acknowledgements

The results which is covered in this work is a product of many days and hours of spending time in the laboratory and in front of my computer. This has been done in close collaboration with so many people whom I'm highly indebted to.

First of all I would like to thank my immediate supervisor Professor Ole Bang who reposed the trust in me and saw me through thick and thin in my stay at DTU. The large degree of freedom that I had at my disposal made me always think outside the box and became semi-independent. Fruitful discussions during our scheduled weekly meetings coupled with monthly group meetings were important times I will always remember. I have tried different ideas, some worked, some didn't but I'm proud of what I made of it. Tapping on his vast theoretical experience and balancing it with experiments were very fruitful.

I would want to also thank my co-supervisor Dr. Christian Rosenberg Petersen for being the immediate coach and who taught me from scratch the principle of MIR SCG. We almost held discussions every single day on matters that bothered my understanding. His help through out my P.hD. I will describe as invaluable and will always be remembered.

I would also want to thank my colleagues whom I used to share the office with (both present and past) where we had very fruitful discussions as well as the intermittent table football games. They are Manoj, Abu, Daena, Rasmus (old), Rasmus (new), Mikkel, Abu, Michael, Ivan, Rune, Getinet. You guys were simply amazing. I learned a lot from you guys be it SCG or life in general.

I would also want to express my deepest gratitude to my collaborators at NKT Photonics, Nanyang University, and the University of Copenhagen whose contribution to my P.hD. made it a successful one. I would also want to than my collaborators at Radbound University specifically to Professor Dr. Frans J.M. Harren for receiving me in his lab. during my research stay abroad. I would also want thank the European Union's Horizon 2020 program and Otto Mønsted foundations for their financial support.

I wish to thank my family and most especially my wife Abigail Oduro who has been there for me all this while not forgetting the long travels she had to make from Ghana to Denmark almost every three months. To all my Ghanaian family in and around Denmark, I say Thank you!!!!

List of Publications

Some of the work presented in this thesis has been published in journals and conference proceedings - the relevant publications are listed below.

Journal Publications

1. Kwarkye K, Jensen M, Dasa MK, Woyessa G, Jain D, Bowen P, Moselund PM, Sidharthan R, Chen S, Yoo S, Petersen CR. Influence of pulse duration and repetition rate on mid-infrared cascaded supercontinuum. *Optics Letters*. 2020 Sep 15;45(18):5161-4.
2. Kwarkye K, Jensen M, Engelsholm RD, Dasa MK, Jain D, Bowen P, Moselund PM, Petersen CR, Bang O. In-amplifier and cascaded mid-infrared supercontinuum sources with low noise through gain-induced soliton spectral alignment. *Scientific Reports*. 2020 May 19;10(1):1-1.

Conference Contributions

1. Kwarkye K, Jensen M, Engelsholm RD, Dasa MK, Jain D, Bowen P, Moselund PM, Petersen CR, Bang O. Low noise in-amplifier and cascaded mid-infrared supercontinuum sources through gain-induced spectral alignment. In *Mid-Infrared Coherent Sources 2020* Mar 23 (pp. MW3C-4). Optical Society of America. (Oral presentation)
2. Kwarkye K, Dasa MK, Adamu AI, Woyessa G, Petersen CR, Engelsen SB, Bang O. Mid-IR supercontinuum based vibrational overtone combination spectroscopy (Conference Presentation). In *Fiber Lasers XVII: Technology and Systems 2020* Mar 11 (Vol. 11260, p. 112601Q). International Society for Optics and Photonics.
3. Kwarkye K, Dasa MK, Engelsholm RD, Gonzalo IB, Jensen M, Jain D, Petersen CR, Bang O. Pulse to pulse characterization of a cascaded intermediate thulium doped supercontinuum source for absorption spectroscopy applications (Conference Presentation). In *Real-time Measurements, Rogue Phenomena, and*

- Single-Shot Applications IV 2019 Mar 4 (Vol. 10903, p. 109030I). International Society for Optics and Photonics.
4. Woyessa G, Dasa MK, Kwarkye K, Petersen CR, Bang O. Long Wavelength Mid-Infrared Supercontinuum Source. InMid-Infrared Coherent Sources 2020 Mar 23 (pp. MW3C-6). Optical Society of America.
 5. Dasa MK, Kwarkye K, Nteroli G, Efunbajo BO, Bondu M, Woyessa G, Israelsen NM, Bradu A, Petersen CR, Moselund PM, Bowen P. High-pulse energy supercontinuum sources for multi-spectral photoacoustic imaging in the near-infrared wavelength region (Conference Presentation). InOptical Biopsy XVIII: Toward Real-Time Spectroscopic Imaging and Diagnosis 2020 Mar 9 (Vol. 11234, p. 112340B). International Society for Optics and Photonics.
 6. Efunbajo OB, Dasa MK, Kwarkye K, Bowen P, Moselund PM, Andersen PE, Bang O. Relative intensity noise dynamics in supercontinuum generation with varying repetition rates for multi-modal imaging applications (Conference Presentation). InOptical Biopsy XVIII: Toward Real-Time Spectroscopic Imaging and Diagnosis 2020 Mar 9 (Vol. 11234, p. 112340H). International Society for Optics and Photonics.
 7. Adamu AI, Dasa MK, Kwarkye K, Woyessa G, Bang O, Markos C. Optical ammonia sensors based on Hollow core fiber and photoacoustic spectroscopy. InLaser Science 2019 Sep 15 (pp. JW4A-64). Optical Society of America.
 8. Dasa MK, Adamu AI, Janting J, Kwarkye K, Markos C, Bang O. Monitoring of ammonia in an aqueous environment using a supercontinuum-based photoacoustic sensing system. InFrontiers in Biological Detection: From Nanosensors to Systems XI 2019 Mar 7 (Vol. 10895, p. 108950L). International Society for Optics and Photonics.

Future Publication

1. The results in Chapter 5 (High repetition rate, stable supercontinuum spectrum up to $10\mu m$) have been submitted for publication before hand in of the theisis.

Contents

Abstract	i
Dansk Resume	ii
Preface	iii
Acknowledgements	iv
Contents	vii
1 Introduction	1
1.1 Scope and Outline of Thesis	4
2 Light-Matter Interaction	9
2.1 Linear Effects of Pulse Propagation in Optical Fibers	9
2.2 Nonlinear Effects of Pulse Propagation in Optical Fibers	25
2.3 Noise measurement with a fast detector and oscilloscope	35
3 Relative Intensity Noise Mitigation in Supercontinuum Sources through cascading scheme	37
3.1 Summary	59
4 Power Spectral Density and Bandwidth Scaling of Supercontinuum sources	61
4.1 Introduction	61
4.2 Summary	73
5 High repetition rate, stable, Supercontinuum Spectrum up to 10 μm	75
6 Application of Supercontinuum Sources in Spectroscopy	87
6.1 Introduction	87
6.2 Measurement Instrumentation	89
6.3 Information in the near and mid-IR region	95
6.4 Multivariate modeling of IR data	96
7 Conclusion and Outlook	101
A Appendix	105
A.1 Statistical Distribution of the RIN and Pulse repetition frequency . . .	105
A.2 Experimental setup for RIN measurement	106
A.3 Splice loss optimization.	107

A.4	Direct absorption measurement of water using relatively long pathlength cuvettes.	108
A.5	Absorption measurement of different kinds of alcohol.	108
	Bibliography	111

CHAPTER 1

Introduction

Supercontinuum generation (SCG) refers to the extreme spectral broadening that occurs when a narrow linewidth high-intensity laser pulse traverses an optical nonlinear medium. The generation of new frequency components is a complex nonlinear interaction of a propagating pulse with the medium as well as absorption/emission processes [1–3]. This is a phenomenon that was first demonstrated by Alfano and Shapiro in 1970 using bulk glass and attributed the broad spectrum achieved to non-degenerate four-photon emission [4]. Afterward, SCG has received widespread investigations in different nonlinear media such as gases, organic and inorganic liquids, solids, just to mention a few [1, 4–7].

The advent of the photonic crystal fibers (PCF) and subsequent fabrication revolutionized SCG as PCF's enhance non-linearities of low loss silica fibers and provides a long interaction length [8, 9]. Moreover, it also offers several degrees of freedom of tailoring the dispersion of the fiber to suit the pump pulse wavelength to exploit the various nonlinear phenomena which determine the coherence, relative intensity noise (RIN), and bandwidth of the SCG [1, 10–13]. The supercontinuum spectra in silica is mostly limited to its transparency window of around $2.4\mu\text{m}$ due to multi-phonon absorption [14, 15]. SCG in silica is a mature technology and as such silica-based supercontinuum sources (SC) are commercially available on the market [16]. Currently, efforts are being made to extend the supercontinuum spectrum into the infrared region where there exist the so-called molecular fingerprints (fundamental and recurring overtones) for the unique characterization of molecules [17–23]. The technology platform for achieving this requires concatenating silica and novel soft glass fibers that extend their transmission above the silica window and pumping at different pulse regimes [10, 24, 25]. Such fibers include fluoride ($ZrF_4 - BaF_2 - LaF_3 - AlF_3 - NaF$ (ZBLAN)), Indium Fluoride (InF_3)), arsenic, and selenide fibers. For example, Christian et.al generated an impressive broadband supercontinuum that spans $1.4 - 13.3\mu\text{m}$ using a step-index chalcogenide fiber [1]. Unfortunately, this broadband spectrum was only limited to an average power of $150\mu\text{W}$ and also he used a bulky optical parametric oscillator as a pump source which makes such a source not useful for real-time applications. Thus, generating broadband, compact, all-fiber, high-power source is imperative for real-time applications.

The compactness of a mid-IR supercontinuum source require the use of off-the shelf standard telecommunication pump diodes using the master oscillator power amplifier (MOPA) configuration which is already a matured technology [19, 25–28].

Additionally, progressively long-wavelength transmitting nonlinear fibers beyond the silica multi-photon absorption edge is needed. The cascading scheme is a novel technique where parameters like mode field diameter (MFD) and soliton order number are matched [29] to achieve effective broadening. Supercontinuum generation using this technique requires pumping the first fiber in the cascade in the anomalous regime which through noise seeded modulation instability leads to the generation of solitons [13, 24]. Such solitons mostly at the red edge of the spectrum will progressively red-shift in subsequent fibers through soliton self-frequency shifting (SSFS) so long as they are above the zero-dispersion wavelengths (ZDW) of the fibers. The fibers in the cascade can either be spliced if they are similar or connectorized if there is a high discrepancy in their thermal properties which is always the case for silica and fluoride fibers [30–32]. Fluoride fibers are soft and fragile and such the cascade is engineered such that the peak power introduced in the first robust silica fiber reduces as one traverses along the cascade. This see a safe operation of laser source well below the damage threshold of these fibers.

The nonlinear dynamics leading to the generation of mid-IR supercontinuum source is mostly initiated by amplification of noise through modulation instability (MI) which breaks the pulses into a sea of solitons and this is seen as spectral fluctuations in the spectra [10, 33–35]. The spectral fluctuations are as a result of collision and energy transfer among the solitons as they undergo SSFS. The spectral fluctuations can either be controlled by under-tapering of the fiber [36], seeding of MI [37] and increasing the repetition rate [38] to average over several pulses. To characterize a broadband spectrum, the pulse-to-pulse spectral energy fluctuations are measured over the entire bandwidth of the spectrum [10, 33, 39]. The ratio of the standard deviation and mean of the fluctuating pulse energy for an ensemble of pulses described as the RIN is used to define the noise performance of the laser. The setup uses fast photodetectors and oscilloscopes that can resolve pulses matched to the repetition rate of the laser source as well as narrow linewidth filters (monochromator) over the spectral region of interest [10, 33]. Other methods like the dispersive Fourier transform technique, where there is a transformation of the spectral profile to a temporal delay [39, 40] has been used to characterize broadband laser sources. In othe instances, people have used electrical spectrum analyzers instead of fast photodetectors [33] to study spectral fluctuations in SC sources but are quite cumbersome to realize for mid-IR SC. Particularly for the dispersive Fourier transform technique, there is the need for a long length of a highly low-loss dispersive optical fiber in the longer wavelength region which is difficult to realize as the technology for drawing such fibers is not matured and still in early stages.

The explosion of the human populace has led to high demand for food especially milk for daily consumption. Adulteration of food has become a menace that has attracted the scientific community in proposing optically fast, robust and reliable techniques for monitoring adulteration and quantitative analysis of food constituents [41, 42]. Food adulteration may include adding low-cost readily available food samples to either increase the volume and lifetimes leading to loss of quality of actual food item. Spectroscopy provides the needed platform to monitor these adulterations in

ascertaining the right constituent concentrations in real-time [43, 44]. Spectroscopy is simply the absorption of some wavelength components of a broadband light source after being transmitted or reflected from a sample. Spectroscopic techniques are mostly non-destructive, fast, environmentally friendly (having not to rely on chemicals), and can probe several quality traits of a sample. A simple spectroscopic setup will require a broadband light source, a dispersive medium, a sample holder, and a photodetector that detects the transmitted photons [45]. This might seem a non-trivial technique but the instrumentation is quite complicated and normally designed to suite the sample and the region in the IR spectrum one would want to probe [41, 46]. The infrared (near-infrared (NIR) and mid-infrared (MIR)) section of the electromagnetic spectrum provides an appropriate platform for measuring absorption in food and many other samples owing to the molecular resonances (fingerprints) that exist in this region. Such resonances include the fundamental stretches (O-H, C-H) and the occurring overtones as well as the combination bands which can be used in both 1 and 2-dimensional quantitative data analysis [47–50].

There are numerous limitations of IR spectroscopy mostly due to the non-matured technology of the building blocks that form part of the instrumentation. One typical example is a point broadband light source that has a high power spectral density (PSD) across the IR spectral range [52]. Conventional spectroscopic setups rely on thermal emitters like the global because they are easy to manufacture, cheap and stable. However, since they emit in all directions (omni-directional), they do not provide a spatially coherent light that is required in spectroscopic instrumentation and thus an aperture is always required to filter out stray light [52]. For interferometric setups, point sources are ideal to make sure parallel light rays enter the interferometer and subsequent into the detector which will not require an aperture to filter all stray light. The inclusion of apertures in commercial spectroscopic instruments inadvertently limits the PSD across the broad spectral range.

The high absorption of water in the infrared region and most especially the fundamental O-H stretches located around 2970 nm makes it extremely difficult to probe aqueous solutions [53, 54]. In most cases, the path length of the absorption cuvette has to be scaled to a few microns for direct transmission measurements to occur in aqueous solutions [54]. This trade-off between PSD and path length poses a challenge when samples being probed have sizes that are approximately the same order as the path length of the containing cell. Thus, a high spectral brightness, coherent light source with a high PSD in the IR region is inevitable for spectroscopy to increase the path length of the containing cell.

From Figure 1.1 we compare the spectral brightness of five different broadband sources [51]. Three of the sources are SC sources from silica, fluoride, and chalcogenide fibers. The other two sources are from a synchrotron and a thermal source (global) mostly found in spectroscopic instrumentation [55]. From the Fig., SC sources are typically limited to a comparatively small bandwidth but tend to exhibit a higher degree of brightness over a large portion of the spectrum. Silica SC is the brightest of all the sources with global being the least bright. It is evident from the figure that the brightness of SC sources does match the synchrotron which is a very expensive

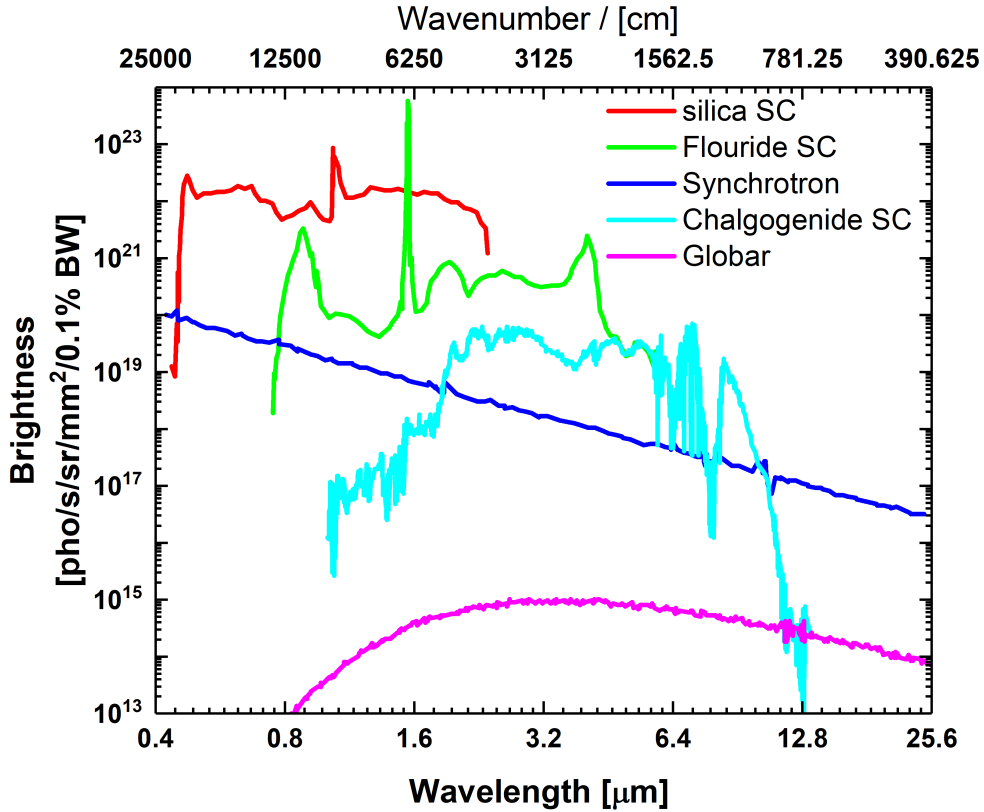


Figure 1.1: A comparison of the spectral brightness SC from silica, fluoride, chalcogenide fibers to a synchrotron and a globar (1500 K blackbody). Figure adapted from [51].

light source both to manufacture and operate and also sits on several kilometers of space. We can therefore do a direct comparison and conclude that SC source is a synchrotron that sits on a bench-top.

1.1 Scope and Outline of Thesis

This aim of the project and dissertation was to research and develop a compact, all-fiber, high power supercontinuum source that span 1000 nm to 4000 nm. Such a source can be realized by employing the cascading scheme where different nonlinear fibers are concatenated to progressively move above the multiphonon absorption edges

of the fibers that form the cascade. Due to the non-linear processes leading to the generation of the spectrum, the spectral fluctuations that are inherent was supposed be characterized and after which mitigated through an in-depth investigation of the nonlinear processes. This will make the source useful for real-time applications. A spectroscopic setup was developed to monitor food adulteration and qualitative analysis of samples like milk and eating oil. A robust data analysis model was developed for the right quantification of the various constituents of samples.

The thesis is organized as follows

Chapter 2: Light-Matter Interaction.

This Chapter is dedicated to understanding the interactions of light with matter and more tailored to the underlying phenomena leading to supercontinuum generation and noise measurement. We first consider the simple fiber geometry and guidance as well as the photonic crystal fiber. We then discuss the pulse propagation in optical fibers and the linear effects that affect the pulse such as dispersion, attenuation, and loss. We also introduce rare-earth-doped fibers mainly for amplification of solitons in SC generation. We continue to discuss the fundamentals of electromagnetism by looking at Maxwell's equations. Afterward, the nonlinear effects of pulse propagation in an optical fiber such as self and cross-phase modulation, four-wave mixing, modulation instability, Raman scattering, and the generation of solitons and dispersive waves are discussed. We also introduce the noise measurement technique used in characterizing broadband sources in especially used in this work in this chapter.

Chapter 3: Relative Intensity Noise Mitigation in Supercontinuum Sources

The cascading scheme is an ideal technique for making a compact, high power, all-fiber mid-IR SC source. But mostly the nonlinear dynamics leading to the generation of the broadband SC is initiated by noise seeded MI. In this chapter, we investigate and propose a technique of aligning the solitons spectrally to mitigate the noise. This Chapter is based on the publication [10]. We start the chapter by discussing the master oscillator power amplifier (MOPA) configuration and discuss the dispersion of fibers used in the generation of the mid-IR SC. We also discuss the experimental setup for quantifying the relative intensity noise (RIN) of our supercontinuum source. We further discuss how the generation of a broadband SC in the first stage of the cascade affects the RIN in the subsequent SC in the cascade. We back the experimental results with theoretical modeling of the noise. We also discuss the absorption/emission contributions from rare-earth-doped thulium fiber which forms an important part of the cascade and discuss the various dynamics arising from gain leading to a high PSD and bandwidth generation.

Chapter 4: Power Spectral Density and Bandwidth Scaling of Supercontinuum Sources.

In this Chapter, we interrogate the most efficient way of generating a high PSD and broad bandwidth mid-IR SC by adjusting the input pulse parameters. We first describe the configuration of the laser source which is based on a directly modulated seed diode with varying pulse duration and repetition rate. The variation in these parameters affects the average power and the peak power achievable by a set of configuration. We relate the variation of the input pulse parameters to the onset of modulation instability which initiates the SC generation. We investigate the change in pulse duration and repetition rate and how it changes the initial spectra which acts as a seed for subsequent spectra. These pulse parameters have a direct bearing on the bandwidth and RIN of the SC generation. We explain the nonlinear effects leading to a low RIN and high bandwidth in a set of laser seed parameters. Moreover, we critically examine the second stage of the cascade by looking at a novel thulium/germanium co-doped fiber which absorbs the residual peak power such that the excess peak power does not damage the soft and fragile fibers in the cascade. We subsequently compare the absorption and performance of this in-house fabricated fiber to the absorption of commercial thulium-doped fiber. This work is based on the publication [19]

Chapter 5: High Repetition Rate, stable Supercontinuum Spectrum up to 10 μm .

This Chapter is dedicated to experimental investigations into making a high repetition rate, stable, and portable SC source that extends the spectrum to about 10 μm by concatenating silica, fluoride, arsenic, and selenide fibers. This source is based on the MOPA configuration discussed earlier. We optimize a high repetition rate source to average several pulses to mitigate the noise which will make the source useful for real applications. We optimize the generation of SC using a piece of Tm and Tm/Ge co-doped fiber. We also investigate the appropriate choice of fibers and fiber length that leads to the efficient generation of mid-IR SC by increasing the bandwidth and average power of the spectrum.

Chapter 6: Application of Supercontinuum Sources in Spectroscopy.

In this Chapter, we use the developed SC source in spectroscopic applications. We investigate the various spectroscopic configuration suitable for the absorption regions we probe. We look into the kind of information (both physical and chemical accessible in both the NIR and MIR region). We delve into normal transmission spectroscopy as well as an attenuated total internal reflection (ATR). We look at the dependence of angle of incidence and wavelength on penetration depth in ATR spectroscopy. We develop spectroscopic models by applying corrections to measured spectra and making spectroscopic interpretation to the measured spectra.

Chapter 7: Conclusions and Outlook

We summarize the results achieved in the previous chapters, the major problems encountered and steps that can be taken to overcome these setbacks to enhance cascaded mid-IR supercontinuum generation in subsequent works.

CHAPTER 2

Light-Matter Interaction

2.1 Linear Effects of Pulse Propagation in Optical Fibers

2.1.1 Fiber Geometry and Guidance

For the various optical fiber types, the simplest is the step-index fiber (SIF) with a circular core and an elevated refractive index n_c enclosed by a circular cladding with a comparatively lower refractive index n_{cl} . Both the core and cladding are made of glass but they can be modified with different glass compositions to achieve the refractive index difference between them. These compositions can either elevate the refractive index of the core or reduce the refractive index of the cladding. The SIF fiber is different from the graded index fiber in that the graded index fiber has a gradual decrease in the refractive index from the center to the core boundary [56]. The main principle behind the light guiding mechanism in waveguides especially optical fibers from a ray optics perspective is total internal reflection (TIR) [57]. Total internal reflection occurs when the incidence angle of light is maximum defined by the Snell's law given by $\sin(\theta_c) = n_c/n_{cl}$. The refractive index difference between the core and cladding defines the ability of the fiber to collect light a property called numerical aperture (NA) defined as

$$NA = \sqrt{n_c^2 - n_{cl}^2} = \sin(\theta_c) \quad (2.1)$$

It is imperative to note that the expression above which defines the NA will not be valid for really high acceptance angles and very small core fibers. The simplest geometry and the light guiding mechanism of the SIF from a ray picture perspective is shown in Figure 2.1. To further understand the guiding properties of a SIF, a rigorous approach which requires solving the wave equation by adopting a scalar approach where it has to be assumed that the fiber is infinitesimally long and has a perfectly cylindrical cross-section. The input electric field propagating in the fundamental mode is assumed to be linearly polarised along the radial coordinate ρ and can then be expressed as

$$\mathbf{E}(\mathbf{r}, t) = \frac{1}{2} \hat{x} [E(\mathbf{r}, t) \exp(-i\omega_0 t) + c.c.] \quad (2.2)$$

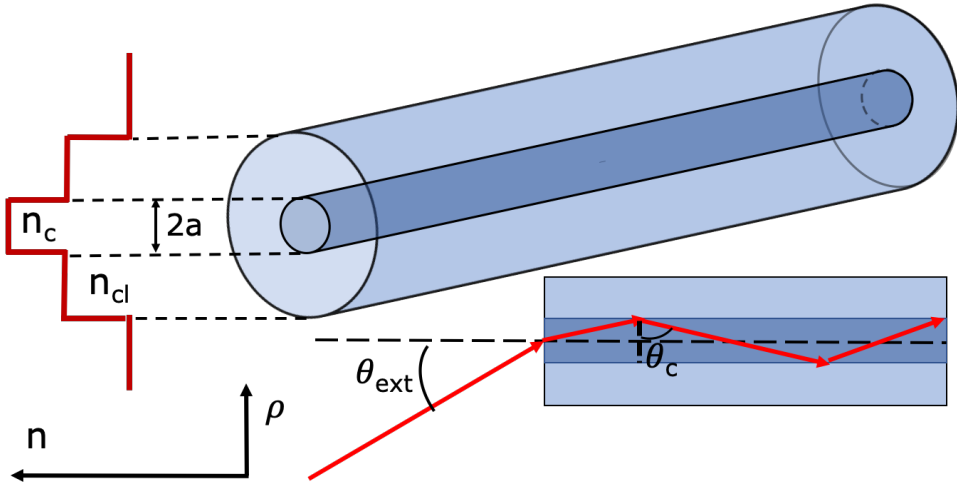


Figure 2.1: A sketch of a cylindrical step index fiber with a core diameter ($2a$) and a refractive index profile (n) as a function of the radial coordinate (ρ). The radial distribution show a core with a higher refractive index and a cladding with a lower refractive index. The guiding mechanism (refraction from the interfaces due to total internal reflection) is also shown beneath, where θ_c is the critical angle and θ_{ext} is the maximum acceptance angle of the fiber.

where $E(\mathbf{r},t)$ is a slowly varying function with time of the propagating pulse relative the carrier frequency w_0 , \hat{x} is the polarization unit vector and c.c is the complex conjugate. Solving the equation by separating the variables we finally arrive at the wave equation of the form

$$\mathbf{E}_A(\mathbf{r}, t) = \hat{x}F(x, y)A(z, t)\exp[i(\tilde{\beta}_0 z - w_0 t)] \quad (2.3)$$

where $F(x,y)$ describes the transverse field distribution of the electric field, $A(z,t)$ is the pulse envelope assumed to be slowly varying along z , $\tilde{\beta}_0$ is the mode propagation constant at a center angular frequency w_0 of the pulse. E_A has been scaled to the actual electric field given by

$$E = \frac{2E_A^2}{\epsilon cn} \quad (2.4)$$

where E is the actual electric field [V/m], ϵ being the vacuum permitivity, n the the refractive index and c the speed of light in vacuum. The instantaneous optical power can thus, be calculated as $|A|^2$.

An optical fiber may support a finite number of guided modes of light whose spatial distribution has been described in equation 2.3 and in order to understand

these supported modes, a solution of the longitudinal components of the electric field along the cylindrical coordinate has to be considered [58]. This is given by

$$\frac{d^2 F}{d\rho^2} + \frac{1}{\rho} \frac{dF}{d\rho} + \left(n^2 k_0^2 - \beta^2 - \frac{m^2}{\rho^2} \right) F = 0 \quad (2.5)$$

where $n = n_c$ is generally complex, however, for mode analysis it is considered that the core is a lossless material and this gives an assumption of the refractive index being real [buck, 56]. The solution in equation 2.5 turns out to be a Bessel function of the first kind in the core region whereas it is a Hankel function that decays into the cladding region. This is solved by applying a continuous electric ($\vec{\mathbf{E}}$) and magnetic ($\vec{\mathbf{H}}$) conditions at the core-cladding interface and also assuming that there is an exponential decay of the condition in the cladding region while we move radially along the fiber leading to an eigenvalue equation defined below.

$$\left[\frac{J'_m}{k_{core} J_m} + \frac{K'_m}{k_{clad} K_m} \right] \left[\frac{J'_m}{k_{core} J_m} + \frac{n_{clad}^2}{n_{core}^2} \frac{K'_m}{k_{clad} K_m} \right] = \left(\frac{m\beta k_0 (n_{core}^2 - n_{clad}^2)}{an_{core} k_{clad}^2 k_{core}^2} \right)^2 \quad (2.6)$$

where $k_{core} = (n_{core}^2 k_0^2 - \beta^2)^{1/2}$, $k_{clad} = \beta^2 - (n_{clad}^2 k_0^2)^{1/2}$ and $k_0 = \omega/c$. The eigenvalue equation has integer solutions m for each β defined as β_{mq} . The distribution of the fiber mode from the equation 2.6 above is thus, the intensity distribution that remains constant upon propagation along the fiber. For a mode to be guided in the fiber the condition $n_{clad} k_0 < \beta < n_{core} k_0$ has to be satisfied. It is imperative to note that the mode in an optical fiber can also be represented by the effective area of the fiber given by the expression

$$A_{eff}(w) = \frac{\left(\iint_{-\infty}^{\infty} |F(x, y, w)|^2 dx dy \right)^2}{\iint_{-\infty}^{\infty} |F(x, y, w)|^4 dx dy} \quad (2.7)$$

One can control the number modes a SIF can support by twerking the fiber parameters as well as the desired wavelength of operation. A very important parameter that determines the number of guided modes is the normalized frequency or the V number which is defined by the sum of the propagation constants k_{core} and k_{clad} embedded in the expression

$$V = k_0 a \sqrt{n_{core}^2 - n_{clad}^2} \frac{2\pi a}{\lambda} NA \quad (2.8)$$

where $k_0 = 2\pi/\lambda$. As can be seen from the the definition of k_0 one would require small core fibers to achieve single mode operation in SIFs. The cut-off wavelength where one can achieve single mode mode operation can be computed using k_0 . When $J_0(V_c) = 0$ there is the smallest solution V_c to the Bessel function which occurs at $V < V_c 2.405$ where the fiber supports only the fundamental mode [59]. For practical realization, the fiber parameters are chosen such that V is very close to V_c . By considering that the difference between the core and cladding refractive indexes is very small assumed to be less than 1, the mode analysis can be simplified by considering the weakly guiding approximation which in principle leads to zero longitudinal components [59].

2.1.2 The Photonic Crystal Fiber

A novel way to achieve a refractive index difference between the core and cladding without the addition of any dopants is what has been realized in the design of photonic crystal fibers (PCF's). The advent of these fibers in the 1970s revolutionized the field of nonlinear optics and more importantly supercontinuum generation [8, 9]. These waveguide designs are quite complicated and therefore the difficulties encountered in fabrication lead to high losses of the fiber [8]. In the 1990s the stack-and-draw method was used to fabricate a low loss PCF with theories predicting that it may be endlessly single-mode at certain wavelengths [8]. The PCF design requires making periodic array of micro-structured capillaries mostly made of air in the cladding along the longitudinal direction of the fiber [8]. Typically, these capillaries have a hexagonal

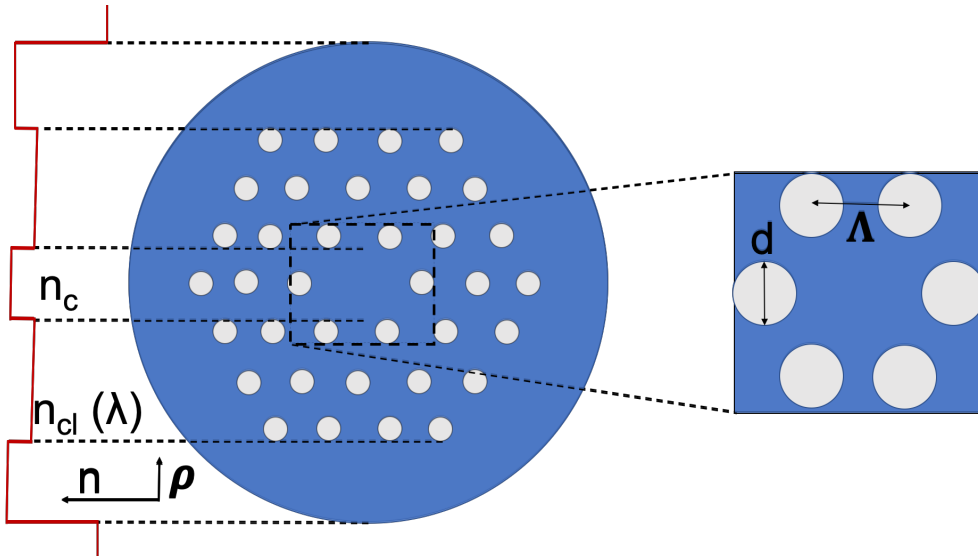


Figure 2.2: Geometry of a PCF which has a single cell core and hexagonal lattice cladding structure made of air capillary cladding. d is the capillary hole diameter and the pitch which is the distance between the center of one capillary to the other indicated as Λ shown in the Fig. The pitch and hole diameter determine the effective refractive index. As indicated on the left, the effective cladding index is lower than the core and it's a function of wavelength.

design with one or more of the holes missing in the center normally referred to as the solid core PCF. Other designs that have hollow-core configuration are available but we will not delve into these designs as they are beyond the scope of this thesis. The refractive index of the cladding can be changed by modifying the hole diameter and

the separation between the holes. The total achieved refractive index of the cladding is normally referred to as the effective refractive index [60]. As can be seen from equation 2.8 defined for SIFs, the effective normalized frequency V_{eff} can also be defined for PCF's as

$$V_{eff} = \frac{2\pi\Lambda}{\lambda} \sqrt{n_{core}^2 - n_{clad,eff}^2} \quad (2.9)$$

where Λ can be approximated as the core radius and $n_{clad,eff}$ is the effective cladding index. The PCF presented above has a missing hole which results in a single-mode operation when $V_{eff} < \pi$ [8, 60]. It is important to note that the holey structure increases the non-linearity of the fiber as well as strong wavelength dependence which cannot be achieved with SIF geometry. Such fibers can guide the fundamental mode without any higher-order mode co-propagating over a broad wavelength range (endlessly single-mode) even at the shorter wavelengths where it will require extremely small core fibers to achieve this with SIF [15, 61]. It can be seen from the equation 2.10 that when $\lambda \rightarrow 0$ V_{eff} approaches a stationary value due to the almost vanishing core-cladding index. For a PCF with triangular design as shown in Figure 2.2, one obtains a single-mode operation when the $d/\Lambda \leq 0.45$ however, in SIFs $V \rightarrow \infty$ for very short wavelengths and makes single-mode operation difficult to achieve at all wavelengths. It is important to note that by changing d and Λ , the dispersion of the fiber can be significantly tuned [62]. The effect of dispersion will be introduced in the next section.

2.1.3 Chromatic Dispersion

Chromatic dispersion describes the frequency dependence of electromagnetic wave interaction with the bound electrons of a dielectric medium. This frequency dependence is normally observed when an electric field is modified as a result of its dependence on the refractive index thereby leading to different frequencies traveling at different speeds. Fundamentally, it arises from the material itself due to oscillating bound electrons being absorbed in the resonant frequencies of the electromagnetic spectrum. This is well defined by Sellmeier's equation as

$$n^2(\omega) = 1 + \sum_{j=1}^m \frac{B_j \omega^2}{\omega^2 - \omega_j^2} \quad (2.10)$$

where ω is the resonance frequency and the magnitude of this resonance is B_j . For silica glass this equation can be written as

$$n^2(\lambda) = 1 + \frac{0.6961663\lambda^2}{\lambda^2 - 0.0684043^2} + \frac{0.4079426\lambda^2}{\lambda^2 - 0.1162414^2} + \frac{0.8974794\lambda^2}{\lambda^2 - 9.896161^2} \quad (2.11)$$

where the wavelength is in microns. Mostly, there is a strong contribution to the dispersion from the waveguide design which is much stronger in PCFs [63]. The effect of chromatic dispersion for a pulse propagating in a fiber can usually be modelled

by Taylor expansion of the coefficient of propagation for a given mode β at a pump center frequency ω_0 in the frequency domain given by

$$\beta(\omega) = n(\omega)\frac{\omega}{c} = \beta_0 + \beta_1(\omega - \omega_0) + \frac{1}{2}\beta_2(\omega - \omega_0)^2 + \dots + \frac{1}{m!}\beta_m(\omega - \omega_0)^m \quad (2.12)$$

where

$$\beta_m = \left(\frac{d^m \beta}{d\omega^m} \right)_{\omega=\omega_0} \quad (m = 0, 1, 2, \dots). \quad (2.13)$$

The important parameters from equation 2.16 are $\beta_1 = 1/\nu_g$ called the group velocity and β_2 the group velocity dispersion (GVD) parameter respectively. The group velocity describes an optical pulse envelope as a packet of waves moving at different group velocities whereas β_2 is the dispersion of the group velocity which mainly contributes to temporal optical pulse broadening in waveguides specifically optical fibers. In practice, the dispersion parameter D is mostly used and this is related to the group velocity dispersion and β_2 as

$$D = \frac{d\beta_1}{d\lambda} = -\frac{2\pi c}{\lambda^2}\beta_2 = -\frac{\lambda}{c}\frac{d^2 n}{d\lambda^2} \quad (2.14)$$

When fibers are pumped in the anomalous regime, ie when $D > 0$, longer wavelengths of the pump travel slower than the shorter wavelengths whereas the opposite holds for pumping in the normal regime as can be seen from Fig. 2.3 [1, 13]. The dispersion parameter is the total sum of the waveguide and material dispersion. In PCF'S one can tailor the dispersion by changing the waveguide properties which involves changing the pitch to hole ratios in those fibers. In SIF's, one can change the design parameters like the core and cladding radius and their refractive indices between them to shift the dispersion. It should be however noted that the PCFs give a much degree of freedom of changing the dispersion due to the vast ways one can change the sizes and distances of the holes and pitches respectively. This tailoring can lead to fibers with no zero-dispersion wavelength (referred to as all-normal dispersion fibers) [64] and those that can have two ZDW's where each of these fiber types provides unique ways of supercontinuum generation [62, 65].

Depending on the propagating pulse parameters, there is a length scale where the dispersion takes effect and dominates known as the dispersion length (L_D) and this should be sufficiently less than the length of the fiber (L), $L \ll L_D$ [59]. The dispersion length is related to the pulse duration T_0 of the propagating pulse, β_2 , by

$$L_D = \frac{T_0^2}{|\beta_2|} \quad (2.15)$$

At the dispersion length, the pulse duration T_0 (measured as $1/e^2$ of the maximum intensity) would have broadened by a factor of $\sqrt{2}$ [59].

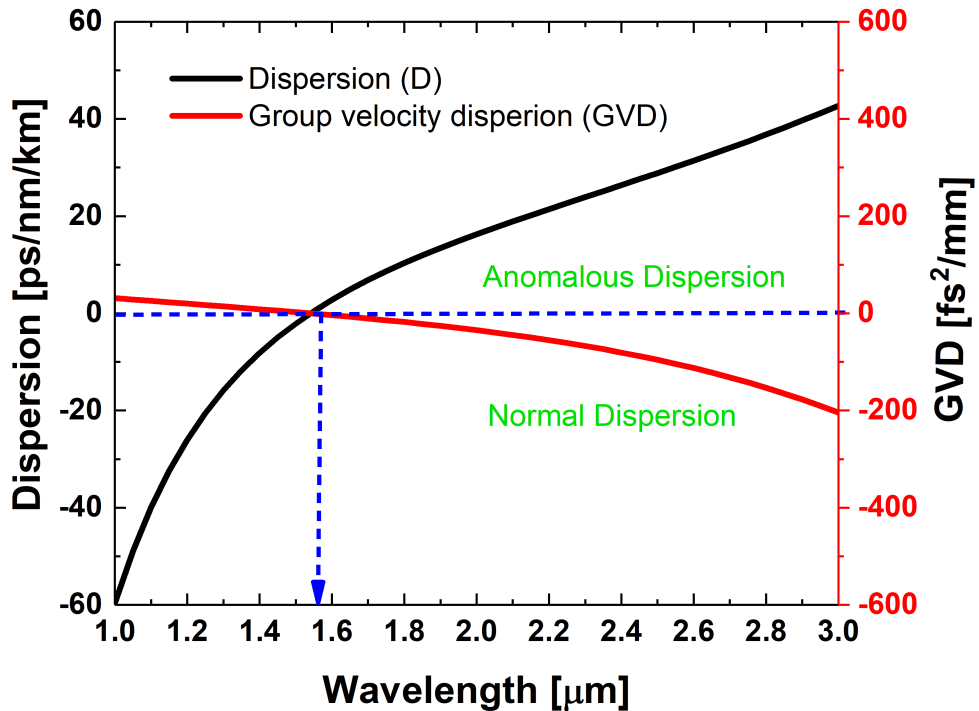


Figure 2.3: A plot of the measured total dispersion parameter D (black) and group velocity dispersion (GVD) (red) of ZBLAN fiber (from FiberLabs) with respect to wavelength. The fiber exhibit a zero-dispersion wavelength (ZDW) of approximately 1580 nm and both β_2 and D vanish at this wavelength. When $D > 0$ we are in the anomalous regime whereas when $D < 0$ we are normal regime.

2.1.4 Optical Attenuation

Supercontinuum generation normally span several octaves and thus, one feature that limits the bandwidth of the SC is optical losses that varies with wavelength. Mostly, the contributing factors to these losses are vibrational and electronic absorption [66]. The vibrational absorption of photons occur at the long wavelength whereas electronic absorption limits short wavelength transmittance. Other contributing factors include scattering within the optical fiber due to imperfection during material processing, fiber fabrication and drawing [67]. Moreover, confinement loss due to leakage of the core mode into the cladding has an impact on the total loss of a fiber. All these losses

are incorporated in the attenuation coefficient as

$$\alpha(\lambda) = A_{ray}/\lambda^4 + A_{imp}(\lambda) + A_{uv}exp(\lambda_{uv}/\lambda) + A_{air}exp(-\lambda_{air}/\lambda) + A_{im}(\lambda) + A_{leak}(\lambda) \quad (2.16)$$

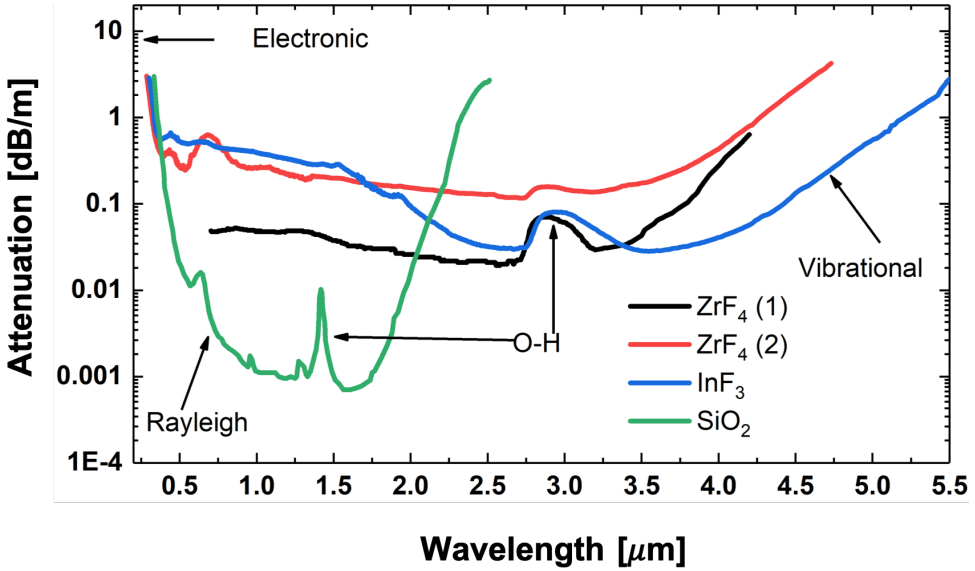


Figure 2.4: The measured attenuation curves of silica, zirconium fluoride (2), indium fluoride (data taken from Thorlabs) and zirconium fluoride (1) (data taken from FiberLabs). The electronic and vibrational loss has been indicated as well as the water absorption due to O-H stretches of the overtones, combination bands, and fundamental, located at 1.4, 1.9, and 2.9 μ m respectively.

where A_{ray} is the loss induced by Rayleigh scattering, A_{imp} is loss as a result of scattering due to imperfection, A_{uv} is the strength of the ultraviolet absorption which scales with the resonance wavelength λ_{uv} , A_{air} is the infrared absorption which also scales with the resonance wavelength λ_{air} , A_{im} is the absorption as a result of impurities and A_{leak} is the loss due to leaking modes from the core to the cladding.

Generally, all these attenuation mechanisms can be categorized as either scattering, absorption, and confinement losses as already indicated in the previous paragraph. In the case of silica, the material absorption and Rayleigh scattering are dominant factors that contribute to its loss. The electronic and vibrational resonances are located in the short and long wavelength regions respectively. This limits the transmittance of silica in the shorter wavelengths to 300 nm and longer wavelengths to 2400 nm as

can be seen from 2.4 and as such other materials whose transmission extends well above that of silica window has to be considered for applications like supercontinuum generation. From Fig. 2.4 ZrF_4 and InF_3 offer a higher transmittance into the infrared (IR) region and even chalcogenide fibers can transmit up to 12000 nm.

Rayleigh scattering is normally caused by density fluctuations as a result of variation in the refractive index [67] which is much smaller than the optical wavelength and scales with λ^{-4} . This loss for fused silica can be expressed as

$$\alpha_{ray}(\lambda) = \frac{A_{ray}}{\lambda^4} \quad (2.17)$$

where $A_{ray} = 1.3 \text{ dB/km}/\mu\text{m}^4$. During the fiber fabrication process, impurities are added to its composition which tend to increase absorption loss. These basic elements include the residual O-H contributions due to water molecules that give a strong absorption at 1400 nm in silica and 2900 for the fluoride fibers. This O-H absorption may come originally from the fiber fabrication process or post fiber processing where water molecules diffuse into the core of the fiber. The magnitude of the contribution of the O-H absorption can be found by approximating it to a Lorentzian profile which assumes the shape

$$\alpha_{O-H}(\lambda) = \frac{A_{O-H}}{1 + \left(\frac{\lambda - 1385 \text{ nm}}{16 \text{ nm}}\right)^2} \quad (2.18)$$

where A_{O-H} is the peak loss value. Another loss that can mostly be observed in microstructured fibers is the confinement loss. This involves leakage of modes from the core to the cladding and consequently being stripped off by the fiber coating which is normally pronounced at longer wavelengths. The geometry of the micro-structured fiber contributes greatly to this loss, for example, in PCF's this loss increases with decreasing core size and increases with decreasing hole size and number of rings in the fiber. The confinement loss can be calculated as

$$A_{leak} = \frac{40\pi}{\lambda(10) \ln} \text{Im}(n_{eff}) \quad (2.19)$$

where $\text{Im}(n_{eff})$ is the imaginary part of the effective refractive index and λ is the wavelength in meters. In this thesis, losses due to confinement were neglected as we mostly used SIF's in our configuration. Typically, the attenuation in fibers is measured by calculating the attenuation coefficient α for an input power P_0 and transmitted power P_{TR} over a length L of the fiber given by

$$P_{TR} = P_0 \exp(-\alpha L), \quad \alpha_{dB} = -\frac{10}{L} \log \left(\frac{P_{TR}}{P_0} \right) = 4.343\alpha \quad (2.20)$$

where α_{dB} is the attenuation per fiber length. This parameter characterizes the performance of the fiber for an input power.

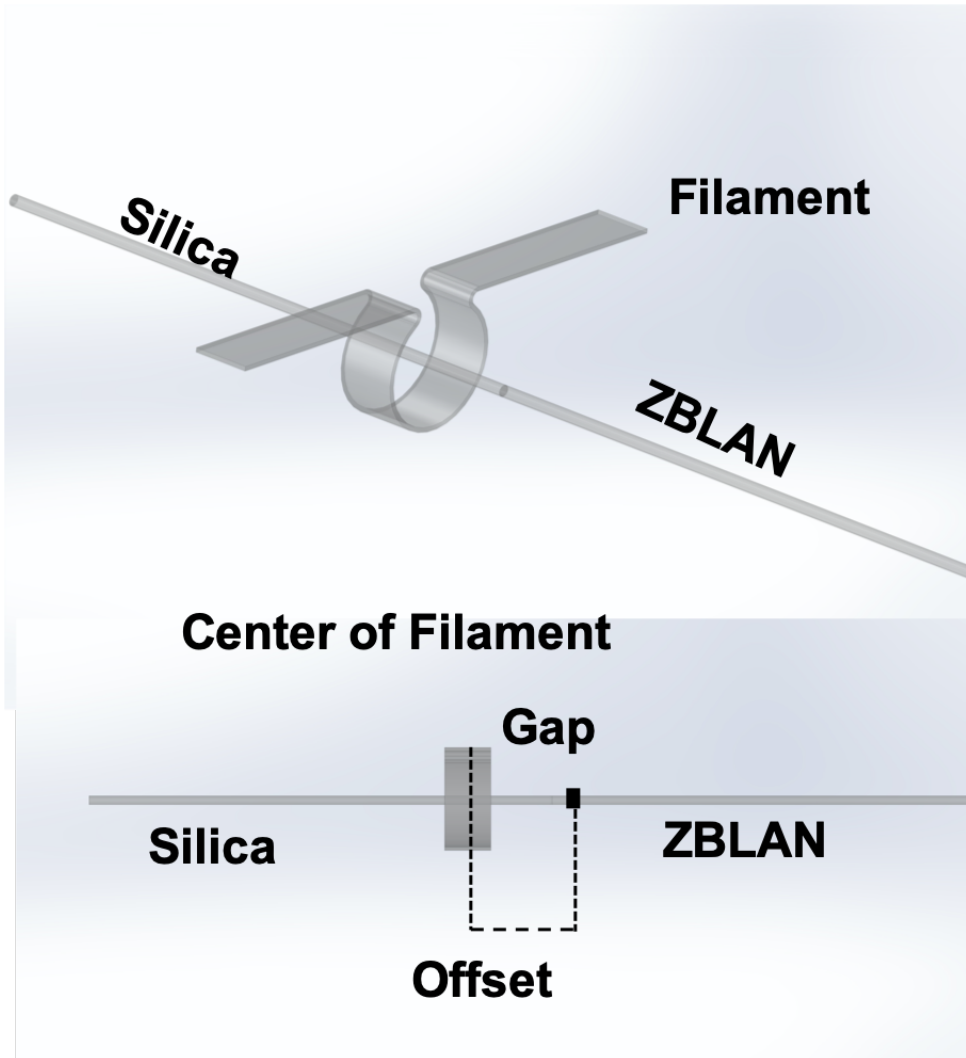


Figure 2.5: Schematic of a 3D arc shaped filament splicer and the axial view depicting the gap offset between silica and ZBLAN fibers before splicing.

2.1.5 Optical splice loss

When two fibers are spliced together, there exist losses induced by local heating, bad cleave quality, impurities at the interfaces as well as core misalignment, normally called joint losses [68]. A typical example of the effect of core misalignment is shown

in Figure 2.6. A slight offset in the core as shown in (a) lead to a loss of 9.491 dB whereas in (b), an almost aligned core leads to a loss of about 0.134 dB. During fusion splicing, all the fundamental mechanisms involved in heat transfer namely (conduction, convection, and radiation) do play a part in the splicing process. It is required that the fibers are heated well enough so that they can bond together. This temperature which is called the glass transition temperature occurs around around $1700^{\circ}C$ in silica whereas for fluoride fibers it around $450^{\circ}C$. The discrepancy in temperature is due to the low phonon energies in fluoride fibers and makes fusion splicing of silica and fluoride fibers extremely difficult as surface tension and viscosity tend to deform the fibers above their transition and softening temperatures [69]. For similar silica fibers, commercial fusion splicers can achieve losses as low as 0.01 - 0.02 dB. Such low loss splices can be realized by carefully optimizing splice parameters like pre-gap between the fibers, pre-push, hot-push, push velocity, hot-push delay, splice offset, on duration time and the power. The appropriate choice of a heat source incorporated into a fusion splicer such as an electrode arc, a resistively heated metal filament, a laser light source would determine the most important power that will be required to heat the fibers. In special cases where dissimilar fibers are spliced, offset of heating between the two fibers to have uniform heat distribution among the fibers. Similarly, the push velocities and pre-gap must be carefully optimized to suit the fibers [68–70]. Connection losses for single-mode fibers with a mode field diameter mismatch between them can be calculated from the equation

$$L_c = -20 \log \left(\frac{2w_1 w_2}{w_1^2 + w_2^2} \right) \quad (2.21)$$

where w_1 and w_2 are the fiber mode field radii defined as the spatial distribution of the fundamental mode where the intensity has dropped to $1/e^2$ so long as the beam profile has a close to Gaussian distribution. For similar mode field distribution within the fibers, the splice loss can be calculated by using equation 2.20.

2.1.6 Rare-earth doped fibers and mechanism of Amplification

Shortly after the demonstration of the first laser, the first fiber laser was realized in the year 1961 by Snitzer and co-workers [71, 72]. The word laser is the acronym for *light amplification by stimulated emission of radiation*. From the classical picture, light mostly is generated by the acceleration of electrons but the approach in lasers involves stimulated emission of ions. Whilst electronic amplification involves minute variations in injected electric current and voltage changing the flow rate and charge density of carriers, lasers require bound states called energy levels [73]. Lasers have an active medium and oscillators with which several passes of light lead to amplification. The oscillators may consist of two highly reflective surfaces and provide optical feedback leading to lasing. In some instances, there is no oscillator but rather a gain medium which leads to amplification of the signal [73].

The gain medium used in fiber lasers is based on the rare-earth ions. Their uniquely distinguishable characteristics from other optical ions make them ideal for

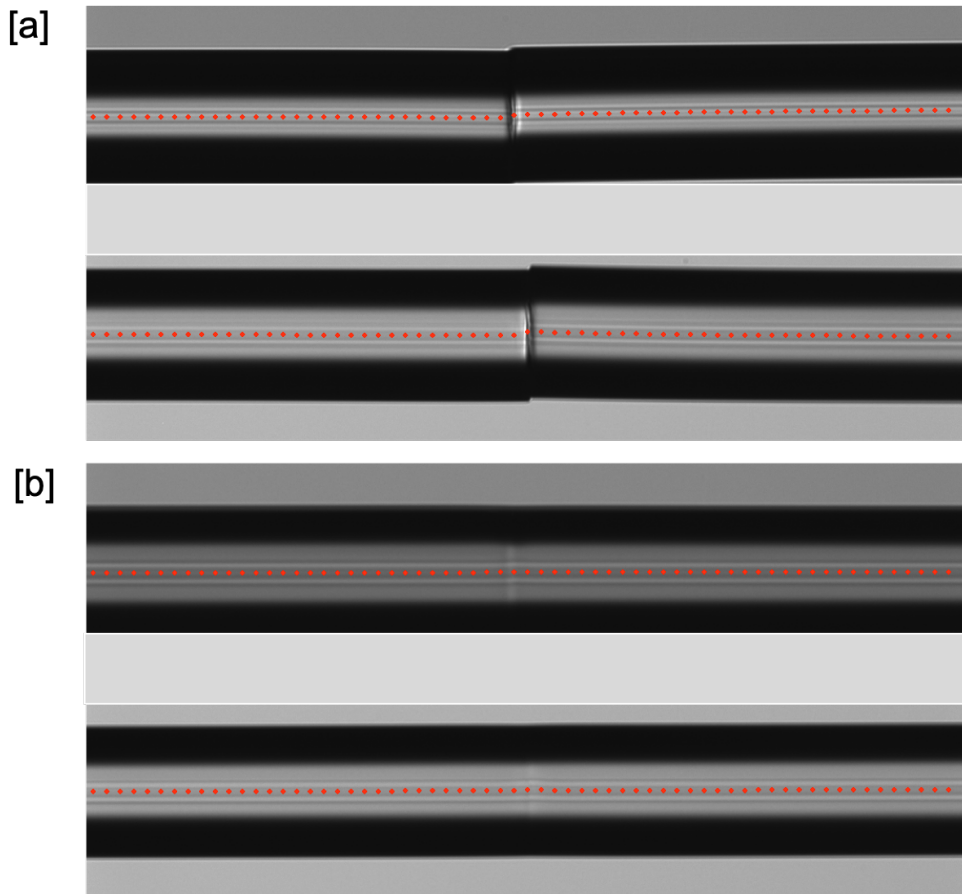


Figure 2.6: The effect of core misalignment during splicing of two ZBLAN fibers.
 (a) Core slightly misaligned leading to a splice loss of about 9.491 dB
 (b) Core almost perfectly aligned leading to a splice loss of 0.134 dB.

integrating them into fiber lasers. Such characteristics include absorption and emission over a narrow wavelength range and these absorption and emission transitions are independent of the host material, long meta-stable states, and high quantum efficiencies. The high performance of the rare-earth ions in optical lasers is due to the nature of states and the few characteristics listed above.

The rare-earth ions which are not rare naturally and occur in abundance have two groups each with 14 elements. These groups are the lanthanides and actinides. The lanthanides have the filling of the 4f shell whereas the actinides have the filling of the

5f shell. For the lanthanides, the 6s shell is filled which leads to the 4f-shell transition ions being screened from the host. In effect, as the atomic increases along with the periodic table, the 4f ions become more tightly bound to the nucleus (effective nuclear charge) a feature called the lanthanide contraction [74]. In this thesis, we will consider the lanthanides as they are more important in fiber lasers and amplifiers and more specifically Erbium and Thulium ions.

Most fiber lasers and amplifiers are based on the Er^{3+} ion due to strong emission in the Telecommunication wavelength range. Besides, the availability of commercial cheap pump diodes and their high efficiency makes Er^{3+} ideal for optical fiber lasers and amplifiers [73, 75]. Depending on the transmittance of the host and application of the laser, one can excite many transitions in a single host. As there are many pumping schemes, like the 800 nm and 1480 nm, we only consider the 980 nm pumping regime and silica host in our configuration. In Figure 3.10, we show the various transitions associated with this pumping regime.

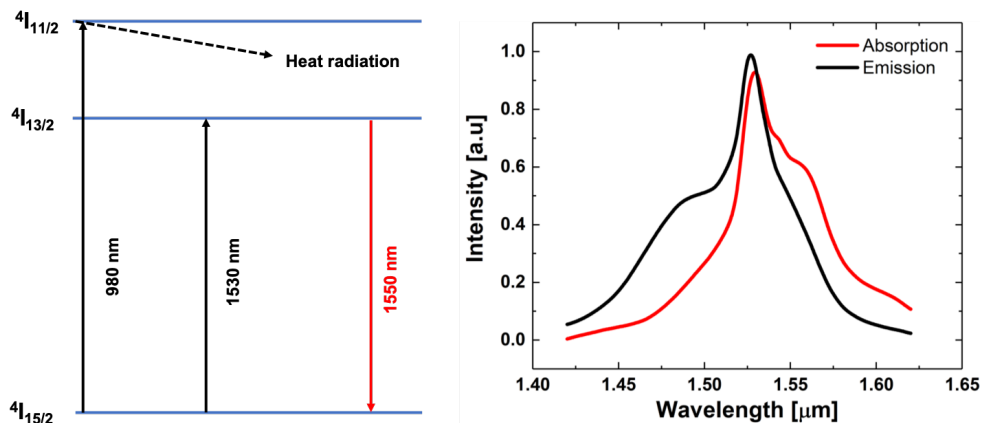


Figure 2.7: (a) Energy level diagram showing the various transitions in Er^{3+} ions pumped at 980 nm leading to 1530 absorption through cross-relaxation processes and non-radiative heat transfer. (b) Absorption - Emission cross-section of Er^{3+} ions with peak absorption and emission at 1530 and 1540 nm respectively.

The $4I_{15/2}$ and $4I_{15/2}$ energy levels are responsible for emission at the 1500 nm region with a peak absorption from 970 and 980 nm. The high quantum-limited noise figures typically of the order of 3 dB and gain efficiency make amplifiers based on this pumping scheme one of the best performing amplifiers [73, 74]. This is due to the large absorption cross-section for this band and also the absence of excited-state absorption (ESA) at the $4I_{13/2}$ level. For about 540 mW of injected power, 250 mW was realized

as an output for a 50 nm wavelength range [76]. The relatively short lifetimes at of the $^4I_{11/2}$ in oxide glasses leads to an almost negligible stimulated emission at the pump. The cross-sections of Er^{3+} spectra are influenced by the absorption and emission spectra. We show the the as absorption and emission dynamics and their cross-sections in Figure 3.10.

The first laser based on Tm^{3+} ions operated in the wavelength region of 1900 nm and was demonstrated by Gandy et al with Li-Mg-Al silicate glass as host [77]. Tm^{3+} has transitions in silica host as well as fluoride host. Tm^{3+} exhibits transitions where Er^{3+} and Nd^{3+} don't have transitions, in the wavelength range of 1400 - 2700 nm. The availability of meta-stable states and effective phonon frequency are requirements

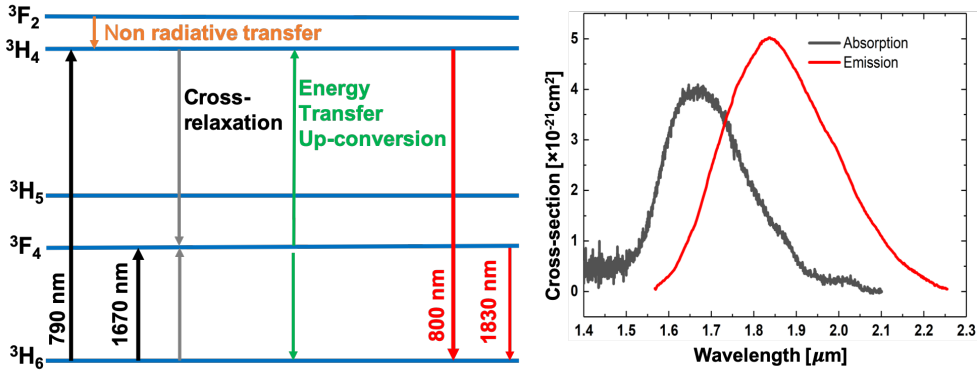


Figure 2.8: (a) Energy level diagram showing the various transitions in Tm^{3+} ions pumped at 790 nm leading to 1670 absorption through cross-relaxation processes and non-radiative heat transfer. (b) Absorption - Emission cross-section of Tm^{3+} ions with peak absorption and emission at 1650 and 1850 nm respectively.

for achieving lasing in a gain medium. Such states in Tm^{3+} is rare and only the high lying 1G_4 and 1D_2 are meta-stable in most host glasses [78, 79]. That notwithstanding, 3F_4 and 3H_4 states have small energy gaps that make their quantum efficiency much dependent on their host. The lifetimes of energy levels below 3H_5 , 3F_3 and 3F_2 are very small making it extremely difficult to achieve population inversion no matter the host material [78]. Due to the non-availability of pump diodes in the short wavelengths to excite transitions, mostly, up-conversion pumping in the long-wavelength regime is implemented which is not an efficient technique to obtain luminescence [79]. As can be seen from Figure 2.8, the 3F_4 and 3H_6 transition provides a broad emission spectrum that peaks around 1850 nm, and such broad-spectrum provides wide tunability in fiber lasers [79]. Similarly, the 3H_6 and 3F_4 is broad as a result of the high number of

Stark components and significantly larger splittings that reside in the Tm^{3+} manifold [80].

Thulium ions are efficiently pumped at 790 nm and achieve a high quantum efficiency through cross-relaxation processes. In this case, two neighboring Tm^{3+} ions at the 3H_4 manifold exchange energy with both transiting to the 3F_4 energy level and mostly achieved with high thulium doping concentrations. In a more complicated situation undertaken in this study, we excite these Tm^{3+} transitions by seeding it with a broadband supercontinuum source (operating in the wavelength region 1300-2400 nm) which will be discussed in Chapters 3 and 4 of this thesis.

2.1.7 Fundamental Electromagnetism

The foundation with which the propagation of electromagnetic waves through an optical medium can be well understood is by applying the Maxwell's equations. In our consideration of optical fibers where there is no electric charge ($\rho = 0$) and free current density ($\mathbf{J} = 0$), the Maxwell's equations takes the form,

$$\nabla \times \mathbf{E}(\mathbf{r}, t) = \frac{\partial \mathbf{B}}{\partial t}(\mathbf{r}, t) \quad (2.22)$$

$$\nabla \times \mathbf{H}(\mathbf{r}, t) = \mathbf{J}(\mathbf{r}, t) + \frac{\partial \mathbf{D}}{\partial t}(\mathbf{r}, t) = \frac{\partial \mathbf{D}}{\partial t}(\mathbf{r}, t) \quad (2.23)$$

$$\nabla \cdot \mathbf{D}(\mathbf{r}, t) = \rho(\mathbf{r}, t) = 0 \quad (2.24)$$

$$\nabla \cdot \mathbf{B}(\mathbf{r}, t) = 0 \quad (2.25)$$

where \mathbf{E} and \mathbf{H} represents the electric and magnetic field vectors respectively and \mathbf{D} and \mathbf{B} are the corresponding electric and magnetic flux densities. When a field is applied to a medium, the constitutive relation of the electric and magnetic flux densities to above defined equations can be written as

$$\mathbf{D}(\mathbf{r}, t) = \epsilon_0 \mathbf{E}(\mathbf{r}, t) + \mathbf{P}(\mathbf{r}, t) \quad (2.26)$$

$$\mathbf{B}(\mathbf{r}, t) = \mu_0 \mathbf{H}(\mathbf{r}, t) + \mathbf{M}(\mathbf{r}, t) \quad (2.27)$$

where $\epsilon_0 = 8.854 \times 10^{-12} \text{ Fm}^{-1}$ is the vacuum permittivity and $\mu_0 = 4\pi \times 10^{-7} \text{ Hm}^{-1}$ is the vacuum permeability. \mathbf{P} and \mathbf{M} are the induced electric and magnetic polarization, the later being zero for non-magnetic medium. By taking the curl of equations (2.22), (2.23) and using equations (2.26) and (2.27), the wave equation for an electric field can be derived as

$$\nabla \times \nabla \times \mathbf{E}(\mathbf{r}, t) - \frac{1}{c^2} \frac{\partial^2 \mathbf{E}}{\partial t^2}(\mathbf{r}, t) - \mu_0 \frac{\partial^2 \mathbf{P}}{\partial t^2}(\mathbf{r}, t) = 0 \quad (2.28)$$

where c is the speed of light and can be defined as $c = 1/\sqrt{\epsilon_0 \mu_0} = 2.998 \times 10^{-12} \text{ ms}^{-1}$. Generally, this equation is complicated and needs to be treated from a quantum

mechanical angle where optical frequencies nearing medium resonances are considered [59, 81].

The induced polarization term $\mathbf{P}(\mathbf{r}, t)$ in Equation 2.28 has two terms

$$\mathbf{P}(\mathbf{r}, t) = \mathbf{P}_L(\mathbf{r}, t) + \mathbf{P}_{NL}(\mathbf{r}, t) \quad (2.29)$$

where $\mathbf{P}_L(\mathbf{r}, t)$ and $\mathbf{P}_{NL}(\mathbf{r}, t)$ are the linear and nonlinear terms. It is important to write Equation 2.28 in the frequency domain by applying the convolution theorem and by using the Fourier transform and its inverse given by

$$\mathbf{E}(\tilde{\mathbf{r}}, w) = \epsilon_0 \int_{-\infty}^{\infty} \mathbf{E}(\mathbf{r}, t) \exp(iwt) dt, \quad (2.30)$$

and

$$\mathbf{E}(\mathbf{r}, w) = \frac{1}{2\pi} \int_{-\infty}^{\infty} \tilde{\mathbf{E}}(\mathbf{r}, t) \exp(-iwt) dt, \quad (2.31)$$

to obtain

$$\nabla \times \nabla \times \tilde{\mathbf{E}}(\mathbf{r}, w) - \frac{w^2}{c^2} \mathbf{E}(\tilde{\mathbf{r}}, w) - \mu_0 w^2 \mathbf{P}(\tilde{\mathbf{r}}, w) = 0 \quad (2.32)$$

In the linear regime (where the intensities of the propagating electromagnetic radiation are treated as small perturbations to the propagating medium) the induced linear polarization term is related to the electric field by.

$$\mathbf{P}_L(\mathbf{r}, t) = \epsilon_0 \int_{-\infty}^t \chi^{(1)}(t-t') \cdot \mathbf{E}(\mathbf{r}, t') dt' \quad (2.33)$$

and by using the convolution theorem of Fourier theory, this equation can be changed to the frequency domain expressed as

$$\mathbf{P}(\tilde{\mathbf{r}}, w) = \mathbf{P}_L(\tilde{\mathbf{r}}, w) = \epsilon_0 \chi^{(1)}(w) \mathbf{E}(\tilde{\mathbf{r}}, w) \quad (2.34)$$

By direct substitution of Equation 2.34 into 2.32 making use of the identity $\nabla \times \nabla \times \tilde{\mathbf{E}}(\mathbf{r}, w) = -\nabla^2 \tilde{\mathbf{E}} + \nabla(\nabla \cdot \tilde{\mathbf{E}})$ we arrive at the wave equation in the frequency domain for the linear regime given by

$$\nabla^2 \tilde{\mathbf{E}}(\mathbf{r}, w) + \tilde{\epsilon}(w) \frac{w^2}{c^2} \mathbf{E}(\tilde{\mathbf{r}}, w) = 0 \quad (2.35)$$

where $\epsilon(w)$ is the frequency dielectric constant. The first order susceptibility term $\chi^{(1)}$ describes the linear effects and relates $\epsilon(w)$ by .

$$\epsilon(w) = 1 + \tilde{\chi}^{(1)}(w), \quad (2.36)$$

where $\tilde{\chi}^{(1)}(w)$ is the Fourier transform of $\chi^{(1)}(t)$ and is complex. The real and imaginary components of $\epsilon(w)$ relate the refractive index $n(w)$ and absorption coefficient $\alpha(w)$ given in the expression.

$$\epsilon = (n + i\alpha c/2w)^2 \quad (2.37)$$

2.2 Nonlinear Effects of Pulse Propagation in Optical Fibers

Having discussed the regime where linear effects are dominant, we consider the situation where nonlinear effects sets in and this involves short pulses typically ranging from 10 ns to 10 fs. For such pulses traversing a fiber, both dispersion and nonlinear effects change the pulse shape and spectra [59]. For an applied electric field, the nonlinear contribution of the induced polarization can be modified in the wave equation as can be seen from Equation 2.29 as

$$\nabla \times \nabla \times \mathbf{E}(\mathbf{r}, t) - \frac{1}{c^2} \frac{\partial^2 \mathbf{E}}{\partial t^2}(\mathbf{r}, t) - \mu_0 \frac{\partial^2 \mathbf{P}_L}{\partial t^2}(\mathbf{r}, t) - \mu_0 \frac{\partial^2 \mathbf{P}_{NL}}{\partial t^2}(\mathbf{r}, t) = 0 \quad (2.38)$$

The induced nonlinear polarization can be treated with a power series expansion in its scalar form as

$$\tilde{\mathbf{P}} = \epsilon_0(\chi^{(1)}\tilde{\mathbf{E}} + \chi^{(2)}\tilde{\mathbf{E}}^2 + \chi^{(3)}\tilde{\mathbf{E}}^3 + \dots + \chi^{(n)}\tilde{\mathbf{E}}^n) \quad (2.39)$$

The quantities $\chi^{(1)}$, $\chi^{(2)}$, $\chi^{(3)}$ are the first, second and third order susceptibility. $\chi^{(1)}$ describe the linear response of the medium, $\chi^{(2)}$ is mostly evident in isotropic materials that does not have symmetry with respect to their center of inversion and $\chi^{(3)}$ relates to materials that are centro-symmetric eg. silica glasses. Thus, the most contributing nonlinear polarization term for silica glasses is $\chi^{(3)}$. The consideration of silica glasses and materials that are centro-symmetric in this thesis limits us to the third order induced polarization term which by incorporating it into Equation 2.1 can be expressed as

$$\mathbf{P}_{NL}(\mathbf{r}, t) = \epsilon_0 \int \int \int_{-\infty}^t \chi^{(3)}(\mathbf{r}, t - t_1, t - t_2, t - t_3) \cdot \mathbf{E}(\mathbf{r}, t_1)\mathbf{E}(\mathbf{r}, t_2)\mathbf{E}(\mathbf{r}, t_3) dt_1 dt_2 dt_3 \quad (2.40)$$

The $\chi^{(2)}$ can occur both in centro-symmetric and non-centro-symmetric material. To arrive at an equation that describes the propagation of optical pulses in an optical fiber, we consider the nonlinear polarization equation term in Equation 2.28 relating to the induced polarization and the electric field. To simplify Equation 2.28 we assume a small perturbation of the nonlinear term \mathbf{P}_{NL} and that the response of the medium is local[59]. This assumption fits well with silica where the nonlinear parameter is weak. Considering an instantaneous nonlinear response of a centro-symmetric medium, Eqn. 2.40 can be assumed to be a product of three delta functions and as such neglect all molecular contributions which then reduces it to

$$\mathbf{P}_{NL}(\mathbf{r}, t) = \epsilon_0 \chi^3 : E(\mathbf{r}, t)E(\mathbf{r}, t)E(\mathbf{r}, t) \quad (2.41)$$

2.2.1 Self-Phase and Cross-Phase Modulation

Self-phase modulation (SPM) is the spectral broadening of an optical pulse propagating a nonlinear media due to the intensity dependence of the refractive index [82–

84]. SPM induces an intensity-dependent phase shift but preserves the shape of the propagating pulse after a length scale defined by the nonlinear length given by,

$$L_{NL} = \frac{1}{\gamma P_0} \quad (2.42)$$

where L_{NL} is the nonlinear length, P_0 is the peak power, γ is the nonlinear coefficient which relates the nonlinear Kerr coefficient n_2 , by the relation,

$$\gamma = \frac{n_2 \omega_0}{c A_{eff}} \quad (2.43)$$

where A_{eff} is the effective mode area of the fiber, ω_0 is the center frequency of the pulse. The phase shift induced by SPM is dependent on the length of the fiber and the maximum phase shift occurs at center of the pulse [83, 84] as can be seen in equation 2.45.

$$A(z, T) = A(0, T) \exp[i\phi_{NL}(z, T)], \quad \phi_{NL}(z, T) = |A(z, T)|^2 (L_{eff}/L_{NL}) \quad (2.44)$$

The instantaneous frequency chirp begins at the center frequency which then increases and reaches a maximum at the trailing edge of the pulse. This has been shown in Figs. 2.9 and 2.10 by varying pulse parameters like the input peak power, pulse duration and also the chirp over varying nonlinear lengths. SPM initiated frequency chirp is present at different times which leads to the interference structure as can be seen in the power structure which has been plotted in the frequency domain. This is evident in the Figs. 2.9 and 2.10.

It is clear from the Figs. 2.9 and 2.10 that SPM is dependent on factors like the input peak power, the pulse duration, the non-linearity of the fiber, and the nonlinear length. The pulse used in the simulation has a Gaussian profile in time domain.

$$\phi_{max} = L_{eff}/L_{NL} = \gamma P_0 L_{eff} \quad (2.45)$$

where $A(0, T)$ is the pulse field amplitude at $z=0$. For a lossless fiber, the effective length of the fiber L_{eff} can be approximated as the real length L of the fiber. The spectral changes induced by SPM can be seen in the temporally changing phase due to varying optical frequencies from the center of the pulse ω_0 and the rate of change of the nonlinear phase shift with respect to the instantaneous frequency can be seen as a nonlinear frequency chirp in Eqn. 2.46

$$\delta\omega(T) = -\frac{\delta\phi_{NL}}{\delta T} \quad (2.46)$$

The frequency chirp is negative at the leading edge of the pulse and positive at the trailing edge of the pulse corresponding to blue and red-shifting of the pulse respectively.

On the other hand, if several pulses interact in time, coupling between these optical fields through the Kerr non-linearity without inducing transfer of energy between the

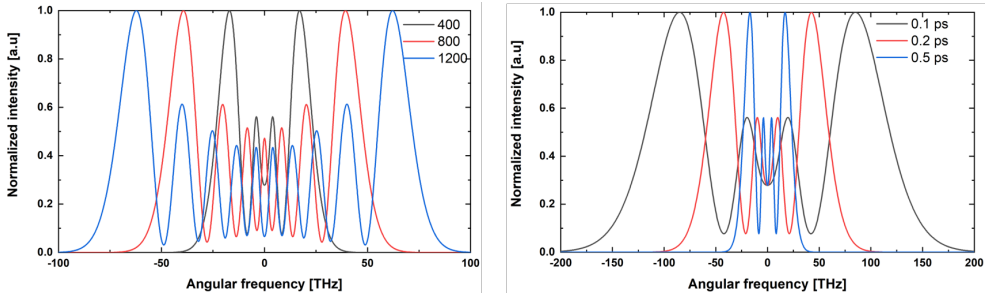


Figure 2.9: Self-phase modulation induced broadening with respect to (a) varying peak power of 400, 800, 1200 W with a constant pulse duration of 0.1 ps (b) varying pulse duration of 0.1, 0.2, 0.5 ps with a constant peak power of 400 W. The initial input pulse parameters are $\gamma = 1(Wm)^{-1}$ and $\beta_2 = 0$ were used in the simulation.

fields is called cross-phase modulation (XPM) [85]. Considering that these two fields have monochromatic angular frequencies ω_1 and ω_2 , and that their electric fields are slowly varying, the total electric field can be expressed as

$$\mathbf{E}(\mathbf{r}, t) = \frac{1}{2} \hat{x} [E_1 \exp(-i\omega_1 t) + E_2 \exp(-i\omega_2 t)] + c.c. \quad (2.47)$$

Substituting the total electric field into Eqn. 2.47 and considering waveguides which exhibit symmetry yields

$$\mathbf{P}^{(3)} = \epsilon_0 \chi^{(3)} \left(\frac{1}{2} [E_1 \exp(-i\omega_1 t) + E_2 \exp(-i\omega_2 t) + c.c.] \right)^3 \quad (2.48)$$

The polarization density functions of ω_1 and ω_2 after expansion of Eqn. 2.48 yields six terms but will consider only two terms in this section and further elaborate the rest of the terms in subsequent sections.

$$\begin{aligned} P_{NL}(\omega_1) &= \chi_{eff}^{(3)} (|\tilde{E}_1|^2 + 2|\tilde{E}_2|^2) \tilde{E}_1 \\ P_{NL}(\omega_2) &= \chi_{eff}^{(3)} (|\tilde{E}_2|^2 + 2|\tilde{E}_1|^2) \tilde{E}_2 \end{aligned} \quad (2.49)$$

where $\chi_{eff}^3 = (3\epsilon_0 \chi^{(3)})/4$ and $|\tilde{E}|^2 = \tilde{E} \tilde{E}^*$ is the electric field and its complex conjugate. The third parameter in Eqn. 2.49 contributes mainly to XPM and provides nonlinear refractive index change to the propagating medium. This means the refractive index change of one of the propagating frequencies induces an index change controlled by its intensity as well as the co-propagating frequency. The contribution of XPM is twice as much as the occurrence of SPM which is explicit in Eqn. 2.49.

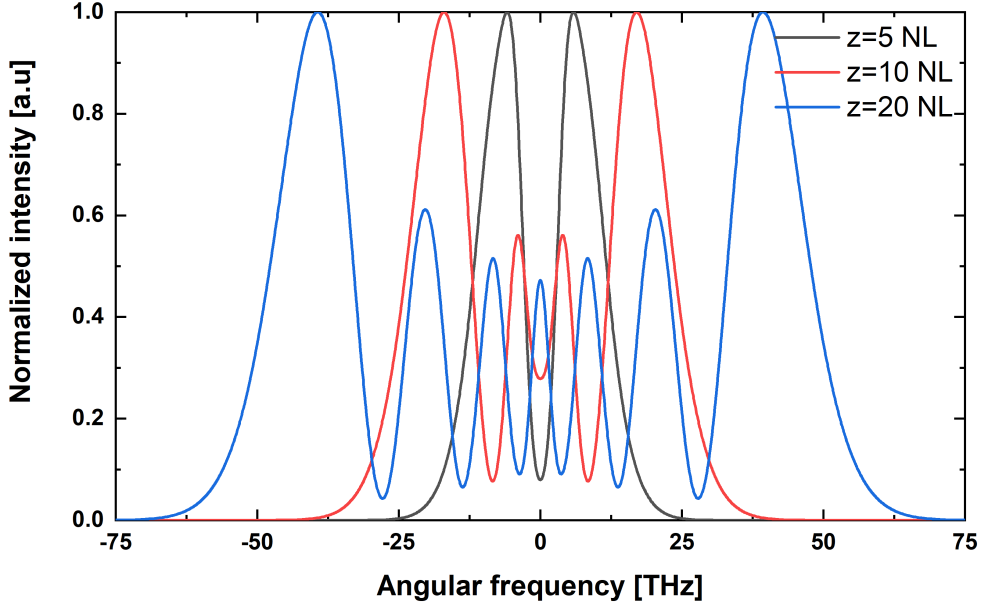


Figure 2.10: Self-phase modulation induced broadening with respect to (a) varying nonlinear length of 5, 10, 20 with a constant pulse duration of 0.1 ps and input peak power of 400 W. The initial input pulse parameters are $\gamma = 1(Wm)^{-1}$ and $\beta_2 = 0$ were used in the simulation.

The induced phase change as a result of XPM is shown in the Eqn. below;

$$\begin{aligned}\phi_{NL,\omega_1} &= n_2 k_0 z (|\tilde{E}_1|^2 + 2|\tilde{E}_2|^2) \\ \phi_{NL,\omega_2} &= n_2 k_0 z (|\tilde{E}_2|^2 + 2|\tilde{E}_1|^2)\end{aligned}\quad (2.50)$$

2.2.2 Four-Wave Mixing

Four-wave mixing (FWM) is a second or third-order parametric process which is due to the nonlinear response of bound electrons to an intense electromagnetic field. FWM is the nonlinear interaction of four optical waves whereby two photons with frequencies ω_1, ω_2 are annihilated creating photons with different frequencies say ω_3 and ω_4 while conserving energy ($\omega_1 + \omega_2 = \omega_3 + \omega_4$) and momentum. Conserving energy and momentum require phase matching condition ($\Delta\beta = \beta(\omega_4) + \beta(\omega_3) - \beta(\omega_1) - \beta(\omega_2) = 0$) for all frequencies as well as the wave vectors [86–88]. The other four terms due to the expansion of Eqn. 2.48 that was neglected earlier are combinations of ω_1 and ω_2 and even third harmonic terms mainly contribute to FWM. There are two types of FWM, 1. the case where a single photon is created through energy transfer between

three different photons ($\omega_1 = \omega_2 + \omega_3 + \omega_4$) and mostly responsible for processes like a third-harmonic generation [59]. 2. two photons of frequencies ω_3 and ω_4 are created due to the annihilation of photons ω_1 and ω_2 which is after satisfying the phase matching condition described above [89]. In many cases, with the description above, there have to be two different fields with different frequencies, but a more interesting degenerate FWM occurs when a single intense beam can be used to achieve the same purpose and most predominant in optical fibers. The strong pulse creates symmetric sidebands which are shifted from the pump frequency known as the Stoke and anti-Stoke frequencies to be discussed in the next section.

2.2.3 Modulation Instability

The interplay between dispersive effects and non-linear effects can lead to the generation of sidebands that are symmetric around the input pulse in the frequency domain [90, 91]. This effect has been shown in Fig. 2.11. In principle, MI can be likened to degenerate four-wave mixing phased matched to SPM but it is initiated from quantum noise. This noise is a result of the local dips and peaks that characterize a rather assumed ideal smooth intensity profile of the pulse.

In mid-infrared supercontinuum generation, MI can mostly be observed when we pump in the anomalous regime which leads to a breakup of a relatively long pulse into ultra-short pulses called solitons [92–95]. To study the effect of modulation instability, the steady state solution to the NLSE is slightly perturbed to realize the relation

$$A = (\sqrt{P_0} + a)\exp(i\phi_{NL}) \quad (2.51)$$

where P_0 is the input power and $\phi_{NL} = \gamma P_0 z$ which is SPM induced nonlinear phase shift. It is an indication that a pulse will propagate within a fiber and can only modify its shape by acquiring a phase shift that is power-dependent. The changes in the perturbation can be studied by analyzing the stability linearly and the coupled frequency components which gives a solution of the form

$$a(z, T) = a_1 \exp[i(Kz - \Omega T)] + a_2 \exp[-i(Kz - \Omega T)] \quad (2.52)$$

where K is the wavenumber and Ω is the frequency of perturbation respectively. K and Ω satisfy the general dispersion relation

$$K = \pm \frac{1}{2} |\beta_2 \Omega| \sqrt{\Omega^2 + \text{sgn}(\beta_2) \Omega_c^2} \quad (2.53)$$

Depending on the sign of β_2 $\text{sgn}(\beta_2) = \pm 1$ and

$$\Omega_c = \sqrt{\frac{4\gamma P_0}{|\beta_2|}} = \frac{4}{|\beta_2| L_{NL}} \quad (2.54)$$

For $\beta < 0$ (anomalous regime) the wavenumber term in 2.53 becomes imaginary leading to sharp growth of the perturbed wave. On the other hand, when $\beta > 0$

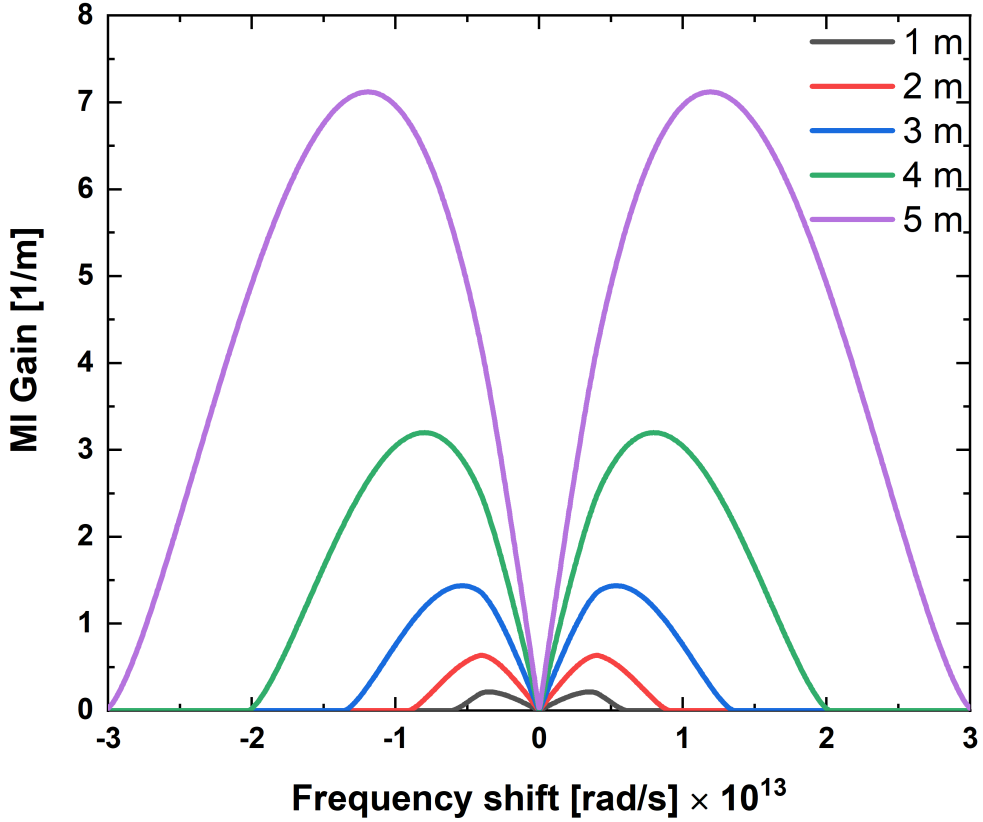


Figure 2.11: MI sideband of a Gaussian pulse with an input peak power of 45 mW injected into and 6 m long erbium doped fiber with a gain of 0.6 / m, $\gamma = 0.0018 / (\text{Wm})$. The gain along the fiber was considered as adiabatic and the MI sideband has been plotted for propagation lengths 1,2,3,4, and 5 m.

(normal regime) the wavenumber term is always a real number, thus stable against all sort of perturbation and thus the probability of scalar MI occurring is almost negligible unless with the inclusion of higher order dispersion terms. The maximum MI gain bands that can be generated and their respective peak positions as shown in Fig. 2.11 is given by the equation

$$\Omega_{MI} = \pm \sqrt{\frac{2\gamma P_0}{|\beta_2|}} \quad (2.55)$$

with a peak value

$$g_{max} = 2\gamma P_0 \quad (2.56)$$

The gain spectrum is seen as symmetric around the center frequency $\Omega = 0$ and the peak gain directly relates peak power and is not affected by dispersion.

We illustrate this effect in Fig. 2.11 by propagating a Gaussian pulse through a 6 m long erbium-doped fiber. The input peak power was about 45 mW and the linear gain of the fiber was about 0.56 / m and $\gamma = 0.0018$ / (Wm). We considered an adiabatic gain along the fiber length and assumed an exponential growth of the input peak power. We then computed the MI gain at 1, 2, 3, 4, 5 m along the fiber as shown in 2.11. The gain in the fiber increases as the peak power of the pulse along the fiber length and hence MI sidebands increase in gain and shift outwardly as expected. It is worth noting that for fibers whose Raman gain falls with the MI band, the Raman gain can significantly enhance the MI gain until the MI band falls outside the Raman gain which will lead to a reduction once again [10].

2.2.4 Raman Scattering

Raman scattering is the inelastic scattering of photons after interacting with the vibrations of the molecules of the medium leading to a downshift or an up-shift of the frequency of the optical field, the extent of this shift determined by the vibrational modes [96, 97]. It is generally a weak process and only a small fraction (10^{-6}) of one optical field is transferred to the other. This light-matter interaction is a χ^3 process which has a time scale that is determined by the response of the molecular vibrations to the interacting photons. We show in Fig. 2.12 the energy level diagram of the possible Raman scattering (Stokes and anti-Stokes) processes. In the Stokes process, the pump excites vibrations in the phonons which leads to loss of photon energy leading to a shift in the frequency called Stokes frequency. On the other hand, the anti-Stokes shift leads to the transfer of energy from the already excited vibrational state to the optical field leading to an up-shift of the frequency [59, 86]. The Stokes phenomena are easy to observe experimentally as most materials in equilibria have their ground states fully field. For rare cases, which exhibit zero photons at the Stokes frequency, this process is known as spontaneous Raman scattering. There can be stimulation of the Raman scattering process by stimulating the Stokes frequency through processes like Raman scattering, a strong pump inducing nonlinear processes like SPM and FWM. This can lead to significant amplification around the Stokes frequency, in the case of silica this is maximum and located at $\Omega = 2\pi \cdot 13.2 THz$. A CW pump traversing an optical fiber with a probe beam, the probe beam will be amplified so long as the difference in frequency between the probe and pump lies well within the Raman gain spectrum. This phenomenon is referred to as stimulated Raman scattering.

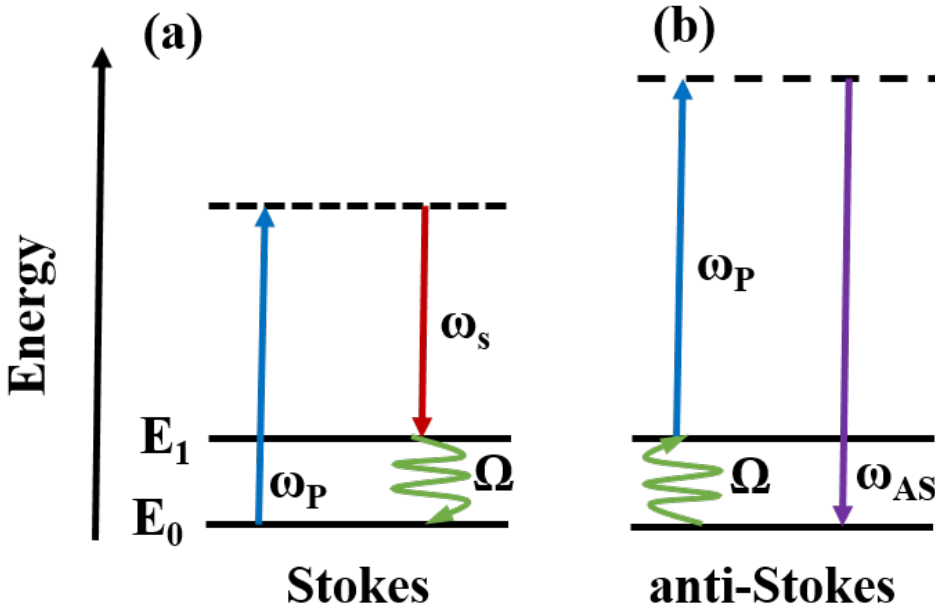


Figure 2.12: Energy level diagram depicting the Stokes and anti-Stokes frequency shifts as a result of the Raman scattering effect.

2.2.5 Solitons and Dispersive Waves

When a pulse traverses an optical fiber pumped in the anomalous regime, the shorter wavelength components tend to move relatively faster than the longer wavelength components. A pulse will temporally broaden and the effect of SPM will be at play where the front part of the pulse will red-shift while the trailing edge will blue-shift. The chirp that arises from the linear GVD and nonlinear SPM can cancel each other given the right β_2 and peak power values such that the dispersion length L_D equals the nonlinear length L_N [59]. This explicitly shown in the equation

$$N^2 = \frac{L_D}{L_{NL}} = \frac{\gamma P_0 T_0^2}{|\beta_2|} \quad (2.57)$$

where N is the soliton order number and $N = 1$ for a fundamental soliton. When the contribution from Raman and fiber losses are ignored a soliton will propagate indefinitely without losing its temporal shape thus, it is stable against perturbations. For $N < 1$ the contribution of the nonlinear factor γP_0 is weak which will lead to many contributions from dispersion induced broadening and will not lead to the generation

of solitons. For a soliton with order $2 > N > 1$ and a pulse propagating in the anomalous regime, the soliton will evolve periodically in a hyperbolic secant shape [14, 98]. This does not depend on the nature of the input pulse. Finally, higher-order solitons with $N > 2$ can be generated. These higher-order solitons do not maintain their shape upon propagation but rather evolve periodically over a propagation length that is given by

$$z_0 = \frac{\pi L_D}{2} \quad (2.58)$$

In contrast to fundamental solitons that are stable to small perturbations, higher-order solitons are not and will continue to shed energy upon propagation. This will lead to it breaking down into fundamental solitons while it tries to adapt and sheds energy that leaves the temporal confinement remaining in the soliton wavelength (non-solitonic radiation) or being dissipated as dispersive waves [14, 29, 59].

The pulse duration and peak power of the input pulse relates to the pulse duration and peak power of the fundamental soliton by the inverse scattering relation which is given by

$$T_k = \frac{T_0}{2N + 1 - 2k} \quad (2.59)$$

$$P_k = \frac{(2N + 1 - 2k)^2}{N^2} P_0 \quad (2.60)$$

where k is an integer from 1 to N . From the relations above it is clear that the first soliton that is generated has the shortest pulse duration and highest peak power which follows the order of k from 1 to N . However, in the presence of perturbations like third-order dispersion, intrapulse Raman scattering, self steepening, this bound state degeneracy is lost. A soliton with N number is a superposition of N fundamental solitons and that the presence of the perturbations aforementioned will initiate soliton fission into N fundamental solitons since a higher-order soliton is already unstable [14, 98, 99]. The relative magnitudes of these effects on the soliton fission process can be studied using the nonlinear Schrodinger equation. These parameters have an inverse relation with pulse duration. The soliton fission process develops over a length known as the fission length given by

$$L_{fiss} = \frac{L_D}{N} \quad (2.61)$$

Intrapulse Raman scattering normally will shift the spectrum of superimposed N solitons by different speeds which will lead to an unstable soliton therefore breaking into fundamental solitons. Relatively short pulse duration and referring to Eqns. 2.59 and 2.60 shorter pulse duration temporarily are generated which are broader spectrally. This leads to amplification of the low-frequency components by the high-frequency components through stimulated Raman scattering. This leads to a continuous transfer of energy to the red edge causing a high degree of red-shifting. This process is known as soliton self-frequency shifting [14, 59]. The frequency of this shift per fiber length has an inverse relation with the temporal width of the soliton and can be

expressed as

$$\frac{dv}{dz} = \frac{8 |\beta_2| T_R}{2\pi 15 T_{sol}^4} \quad (2.62)$$

where T_{sol} is the temporal width of the soliton and T_R relates the slope of the Raman gain spectrum. This is the effect that is responsible for the continuous spectral broadening in MIR SC sources. The soliton with the highest peak power and pulse duration will experience the highest Raman scattering effect and will SSFS more following the order of ejected solitons. This forms a broad continuum of solitons that are spectrally separated. While a soliton would want to compensate for losses posed by the fiber, the soliton width increases while the amplitude decreases. The rate of red-shift decreases and eventually ceases when the width of the spectrum no longer overlaps with the Raman gain.

When the wavelength of a soliton is closer to ZDW, this causes them to overlap with wavelengths in the normal regime by transferring part of their energy [14, 59]. This is facilitated by third-order dispersion and the resonance frequency of the soliton. The dispersive wave position can be calculated from the phase-matching condition that involves the soliton linear and nonlinear phases. The amplitude of a dispersive wave remains negligible not until the phase-matching condition is satisfied. This phase velocity always matches that of a soliton and the frequency shift between them depicts a temporal analog of their angle. The dispersive wave can be generated at a frequencies given by the relation

$$\beta(w_s) - \frac{w_s}{v_{g,s}} + (1 - f_R)\gamma P_s = \beta(w_{DW}) - w_{DW}/v_{g,s} \quad (2.63)$$

where P_s is the peak power of the soliton with a frequency w_s , and a group velocity $v_{g,s}$ which generates a dispersive wave at w_{DW} . Neglecting the effect of fourth-order dispersion the frequency shift between the soliton and the dispersive wave can be approximated as

$$\Omega = -\frac{3\beta_2}{\beta_3} + \frac{\gamma P_s \beta_3}{3\beta_2^2} \quad (2.64)$$

For solitons propagating in the anomalous regime ($\beta_3 > 0$), there is a positive frequency shift as can be seen from Eqn. 2.64 which implies that the dispersive waves that will be generated will be in the normal regime of the dispersion of the fiber. Contrary, when solitons propagate in the normal region dispersive waves will be generated at the red-edge of the spectrum [59]. There is an overlap between the solitons and the dispersive waves through the nonlinear processes XPM and FWM which leads to the generation of new spectral components. The trapped wave exists in the normal dispersion region and therefore slows down the trapped dispersive wave which also slows down the rate of SSFS. The trapping of short wavelength by solitons is a process that occurs readily in relatively long pulse pumping in the anomalous regime leading to mid-infrared SCG.

2.3 Noise measurement with a fast detector and oscilloscope

With a fast detector and oscilloscope and spectrally filtering the broad spectrum, one can measure the pulse-to-pulse fluctuations in the SC. This directly measures the fluctuations in energy from a train of pulses [100, 101]. The SC is filtered with a bandpass filter (a monochromator fitted with gratings was used in this work) which is directed to a fast photodetector and an oscilloscope. The RIN is used to quantify the intensity fluctuations and can be defined as

$$RIN(\omega) = \frac{\sigma}{\mu} = \frac{\langle (|A_i\tilde{\omega}|^2 - \mu(\omega)^2) \rangle^{1/2}}{\langle |A_i\tilde{\omega}|^2 \rangle} \quad (2.65)$$

where σ and μ are the standard deviation and mean of the variations in the train of pulses, $A\tilde{\omega}$ is the field envelope in frequency and $\langle \dots \rangle$ is the average over i pulses. The photodetector voltage response $V(t)$ when light is incident on it is a convolution of the photodetector response function and intensity of the incident light. This can be written mathematically by taking the photodetector response function as $P(t)$

$$V(t) \propto \int_{-T_{rep}/2}^{T_{rep}/2} P(t - \tau) |A(t)|^2 d\tau \quad (2.66)$$

where $T_{rep}/2$ is the inverse of the repetition rate of the light source. The incident light should have a response that is much shorter than the rise of the photodetector from the Eqn. above. In so doing all the totality of the pulse goes through the photodetector before it responds. Thus the input can be approximated as the amplitude of a delta function which is the integrated energy of the train of pulses and can be expressed as

$$|A(t)|^2 \propto E_0 \delta(t) \quad (2.67)$$

where $\int |A(t)|^2 dt = E_0$ is the recorded pulse energy and that we can relate the voltage out of the photodetector to the pulse shape recorded on the oscilloscope and the peak of this response is proportional to the total energy in the pulse given in the expression

$$V(t) \propto E_0 \cdot (Impulse) \quad (2.68)$$

It is worth noting the accuracy of these measurements depends on the operation of the photodetector in the linearity regime to keep a constant voltage on the oscilloscope.

CHAPTER 3

Relative Intensity Noise Mitigation in Supercontinuum Sources through cascading scheme

This chapter is based on the publication [10].

3.0.1 Introduction

Laser sources that are spatially coherent such as frequency combs [1, 102–108], optical parametric oscillators (OPO's) [109] that transmit into the mid-infrared region have received widespread attention due to the various molecular resonances (fundamental and recurring overtones) that exist within this region. These resonances offer unique absorption features which can be used to determine the constituents and concentration of a molecule [103, 110]. The technology for achieving a broadband light source in the mid-infrared to probe these absorption features include but not limited to integrated optical waveguides [102, 109, 111], bulk media [108] and most importantly optical fibers [1, 106, 107, 112]. Fiber-based SC sources are robust and have the advantage of scaling the power spectral density over the entire bandwidth of the SC spectrum.

An all-fiber, compact, high power SC source can be realized by using standard telecommunication pump sources and concatenating various fibers with different dopants, non-linearities as well as thermal properties through a scheme known as cascading [13, 25, 112]. Due to the limitation of silica's transmission window edge in the IR-region to about 2400 nm, the cascading scheme employ cascaded spectral broadening in sev-

eral nonlinear fibers with higher transmittance. Several factors have to be considered in the cascading scheme and such factors include matching the mode field diameter (MFD) and also, since the soft glass fibers have a much lower damage threshold, there should be an appropriate peak power which is introduced into such fibers [24, 113]. The red edge of the SC pump should be dominated with solitons to progressively undergo soliton self-frequency shifting (SSFS) in subsequent fibers in the cascade and the zero-dispersion wavelength should be shorter than the generated solitons [13, 24, 112]. One limiting factor of broadband SC's pumped in the anomalous by relatively long pulses (picosecond to nanosecond) is that the dynamics leading to the generation is seeded by noise through modulation instability generated solitons. The entirety of the SC which is dominated by a sea of solitons suffers from RIN [35, 39, 114]. In some instances, people have tried to mitigate the noise through under tapering of the fiber [36] and in others through seeding of the MI either with limited low power or a phase coherent seed [3, 37, 115, 116]. In real-time applications like spectroscopy and optical coherence tomography (OCT), increasing the repetition rate and averaging of several pulses have enhanced the signal to noise ratio (SNR) [117, 118]. The generation of mid-IR SC involves nonlinear processes and absorption/emission processes. Thus, the appropriate choice of fibers in the cascade and seed parameters influence the RIN [19]. This coupled nonlinear and amplification dynamics to its effect on the bandwidth and RIN has remained an open question which has eluded the mid-IR SC community.

Noise studies on mid-IR SC sources may rely on different configurations and methods to study the fluctuations across the entire bandwidth of the spectra. One of such methods that have been widely used is the Fourier transform technique where there is a transformation of the spectral profile of the SC which is normally detected with a very fast photodiode and oscilloscope from time to wavelength [39, 40, 119]. The spectrum is sent through a highly dispersive medium whose dispersion profile is already known and as such the spectral profile can be correlated from time to wavelength [40, 119]. This method is however limited by using a long length of the nonlinear fiber to stretch the pulses in time and also in the longer wavelength region, there is the limitation of a suitable low loss highly dispersive fibers. On the other hand, other studies have relied on the use of filters and photodiodes to wavelength resolve and capture individual pulses to perform pulse to pulse statistics on the train of pulses captured [39, 114]. One can implement this technique by either using an electrical spectrum analyzer (ESA) [33, 114, 120] or by using fast oscilloscopes [11, 64, 100, 121]. This technique is mostly confined to the silica transmission window or the near-IR region mainly limited by appropriate narrowband filters and fast photodiodes as one moves into the longer wavelength region. Other techniques also rely on the polarization properties of the SC generated [122] whereas others have studied the averaging of several pulses and how they enhance the SNR of the SC generated [38].

In this chapter, we present the pulse-to-pulse spectrally resolved pulse energy changes with respect to wavelength across the entire bandwidth of the generated SC at each stage of the cascade. These experimental investigations are backed by numerical simulations starting from the erbium-ytterbium co-doped amplifier (EYDFA)

here referred to as in-amplifier SC, the second stage which is the thulium-doped fiber (TDF) which is responsible for power redistribution from shorter to longer wavelengths, and the ZBLAN stage which is responsible for red-shifting of the solitons. We emphasize two fundamental effects which are (a) the overlap of the EYDFA gain band to the MI gain bands leading to MI induced soliton pulse break up leading to soliton spectral alignment and its effect on noise which will be elaborated later, (b) the TDF power redistribution stage, how it affects the solitons that are already aligned in the absorption region of the TDF and its effect on the PSD of the entire spectrum. We present the results for two different repetition rates and employ the GNLS to simulate the pulse propagation in the gain fibers and the absorption emission processes.

3.0.2 Experimental set-up and Characterization of RIN

To get a deeper understanding of the RIN dynamics, we set up an experimental setup shown in Fig. 3.1 to measure the pulse energy variation at each wavelength. The output of the supercontinuum source was collimated to a 4mm beam diameter using an off-axis parabolic mirror (OAPM) (RC04FC-P01- Thorlabs) which is silver coated and a CaF_2 lens L1 and then mounted on a 3-D laboratory stage. The beam is directed onto two silver-coated mirrors (M1 and M2) to give degrees of freedom in adjusting the height and position on the monochromator. Using a gold-coated OAPM with a 10 cm focal length, the beam was then focused on the input slit of the monochromator (SpectraPro2300i, Princeton Instruments). The divergence of the beam on the parabolic mirror PM2 and the precision of the beam collimation onto the grating is determined by how well the beam is focused at the input slit (S1).

The monochromator has a Czerny-Turner 2f configuration fitted with 3 different gratings G1, G2 and G3 mounted on a motorized stage which is controlled by an accompanying software. Gratings G1, G2, and G3 have groove densities of 150, 600, and 150 grooves/mm (g/mm). The groove density affects the optimum wavelength region with which a grating can operate (mechanical scanning range), the resolution of the grating, and the dispersion properties of the grating. The higher the groove density the higher the dispersion properties which in turn gives a higher resolution. This can be seen in the inset in Fig. 3.1 where the grating G1 offers the best resolution of approximately 5 nm with an almost same input and output slit width whereas the gratings G2 and G3 have a resolution range of approximately 17-31 nm. The gratings are angle-blazed at wavelengths 800, 1600, and, 4000 nm respectively leading to an optimum operation region of 475-1300, 1000-2400, and 2000-6000 nm. After resolving the input beam to the desired wavelength, the spectrally filtered beam is then focused onto the output slit (S2) by an OAPM (PM3). The precision of the output beam focus is determined by the input focus bearing in mind the 2f configuration. The output beam is then collimated using a CaF_2 lens L2 onto a mirror M3 and subsequently onto a flip mirror FM1. The filtered beam can either be directed onto a photodiode and an oscilloscope to measure the pulse energy variation or to a diffuser attached to ZBLAN

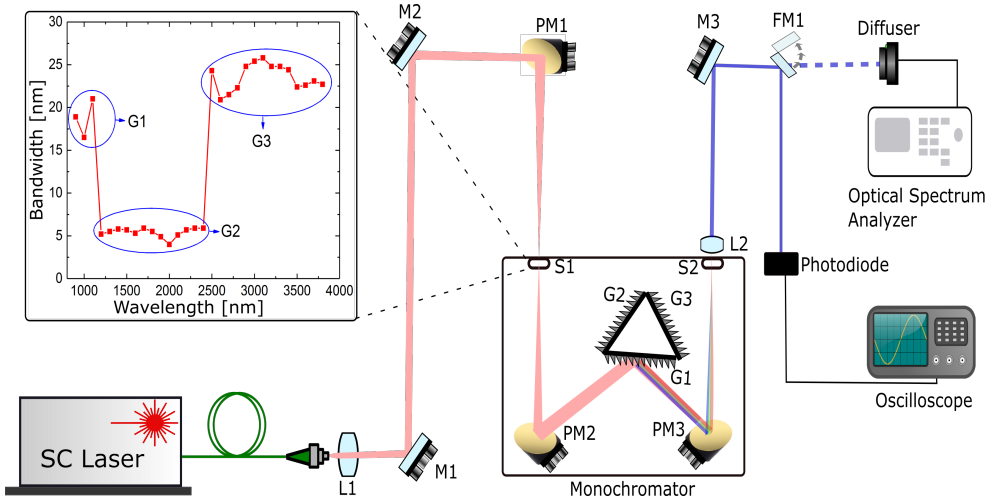


Figure 3.1: (a) Experimental setup to investigate the RIN of the SC source at various stages of the cascade. A monochromator fitted with three appropriate gratings offering different efficiencies in different wavelength regions, a fast photodiode whose bandwidth is more than twice the repetition of the laser source and operates in the required wavelength regions, a fast oscilloscope, and an optical spectrum analyzer(OSA). Inset is the spectral filtering measured at the output of the ZBLAN fiber using the OSA and showing different bandwidths of filtered spectra for the different gratings used.

patch cable to measure the spectral resolution on an optical scanning spectrometer. The spectral resolution was computed by considering the full width half maximum (FWHM) of the normalized intensity plot as can be seen from Fig. 3.2. This has been measured using grating G3 which has an efficiency that spans above 2000 nm but with a rather lower groove intensity which invariably leads to a poor spectral resolution. A resolution of approximately 26-31 nm was computed for the selected wavelengths. For the entire spectrally resolved bandwidth measurements the filtered FWHM span 5-31 nm in the range of 900 -3800 nm. This achieved spectral bandwidth is comparable to experimental studies previously carried out using a similar configuration [62]. In their setup, series of narrow bandpass filters (10 - 30 nm FWHM) were used in the 450-2310 nm wavelength region. It should be noted that the spectral bandwidth of the beam the exits the monochromator depend on the sine angle of the incident light as well as the output monochromator slit width. Thus, there is a trade-off between how wide the output slit width should be and how much power we can have on the photodiode such that we operate it above the noise floor. To avoid higher-order

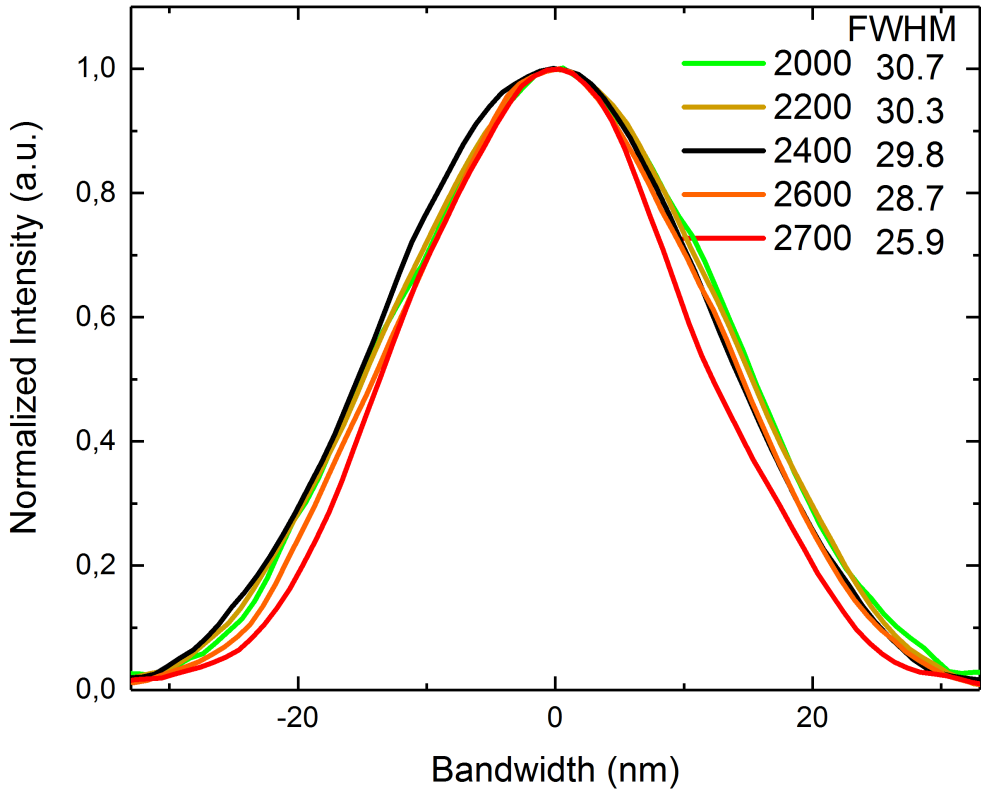


Figure 3.2: Estimate of the FWHM from the normalized intensity plot for selected wavelengths (2000, 2200, 2400, 2600, 2700 nm) measured out of ZBLAN fiber using the OSA. This has been measured with grating G3 with a much lower groove density and such a poor spectral resolution.

diffraction contributions which will appear as ghost signals for certain wavelengths, either a long pass or short pass filter were used to cut off this interference.

The entire SC bandwidth was covered by two photodiodes with responsivities in the desired wavelengths region. One of the two photodiodes used is (PDA10PT-EC InAsSb amplified detector, from Thorlabs) which a thermoelectrically cooled photoconductive indium arsenide antimonide (InAsSb). It has a variable bandwidth from 12.5 to 1600 kHz and operates in the wavelength region of 1000-5800 nm with a peak responsivity around 4900 nm. The other detector is an InGaAs photodiode and has a bandwidth of 125 MHz (Model 1811, New Focus) and operates in the wavelength region 900-1700 nm with its peak responsivity around 1600 nm. Both have an active detector area of approximately 1 mm. The signal from the photodiode is recorded

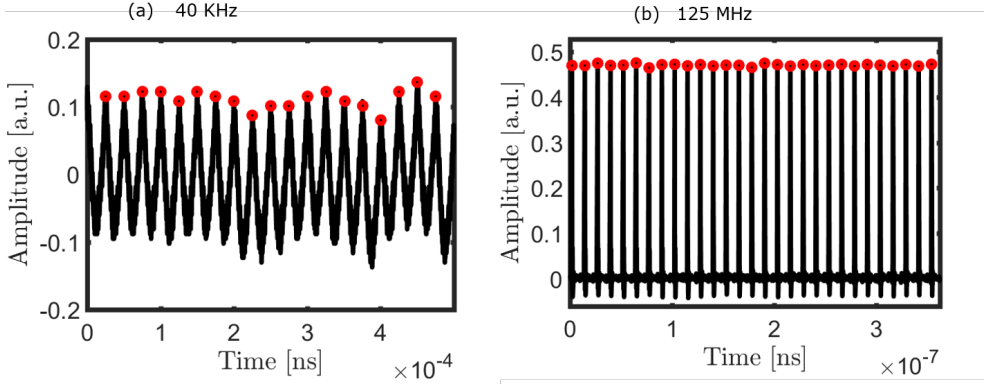


Figure 3.3: Plot showing the effect of satisfying the Nyquist criteria and defining the noise floor. (a) Is a 40 kHz bandwidth photodetector measuring pulses at a repetition rate of 100 kHz and (b) is a 125 MHz photodetector measuring pulses at a repetition rate of 100 kHz.

using a fast oscilloscope (HDO9404 4 GHz, Teledyne Lecroy, maximum sampling rate 40 GS/s and a variable bandwidth from 1 to 4 GHz and up to 10 bits of resolution) and these traces were acquired with a sampling rate of 1GS/s, a bandwidth of 1 GHz, and resolution of 9 bits. In this work, a total of 10000 pulses were acquired for each wavelength that was probed.

The effect of choosing a photodetector with bandwidth more or less than the repetition rate of the laser source is shown in Fig. 3.3. In the first Fig., a 40 kHz bandwidth photodiode is used to measure a train of pulses at a repetition rate of 100 kHz. The pulses are not separated in time and form an oscillating train which makes the noise floor difficult to be defined in such an instance more or less having pulses overlapping in time. The recurring peaks of the pulses must thus, satisfy the condition $T_{FWHM} \ll T_{PD} \ll T_{REP}$ where the T_{FWHM} is the FWHM of the input pulse, T_{PD} is the photodiode response and T_{REP} is the repetition rate of the laser source. For a much higher bandwidth photodetector, as can be seen in Fig 3.3b, the pulses are separated leading to a much well-defined noise floor which has been implemented in this studies. Since the FWHM of the pulse also satisfied the condition above, we could conclude that we satisfied all the conditions for acquiring the pulses. The arrival at 10000 as the standard and statistically viable for analysis can be shown in Fig. 3.4 where there is a plot of the percentage variation of the RIN to changes in the number of pulses. One can see that after 10000 pulses the percentage variation is almost insignificant about 0.01 % of the total acquired pulses. A much higher variation is seen from pulses less than 10000. A choice of 5000 pulses will also reduce measurement time but also give a small variation in RIN. To satisfy

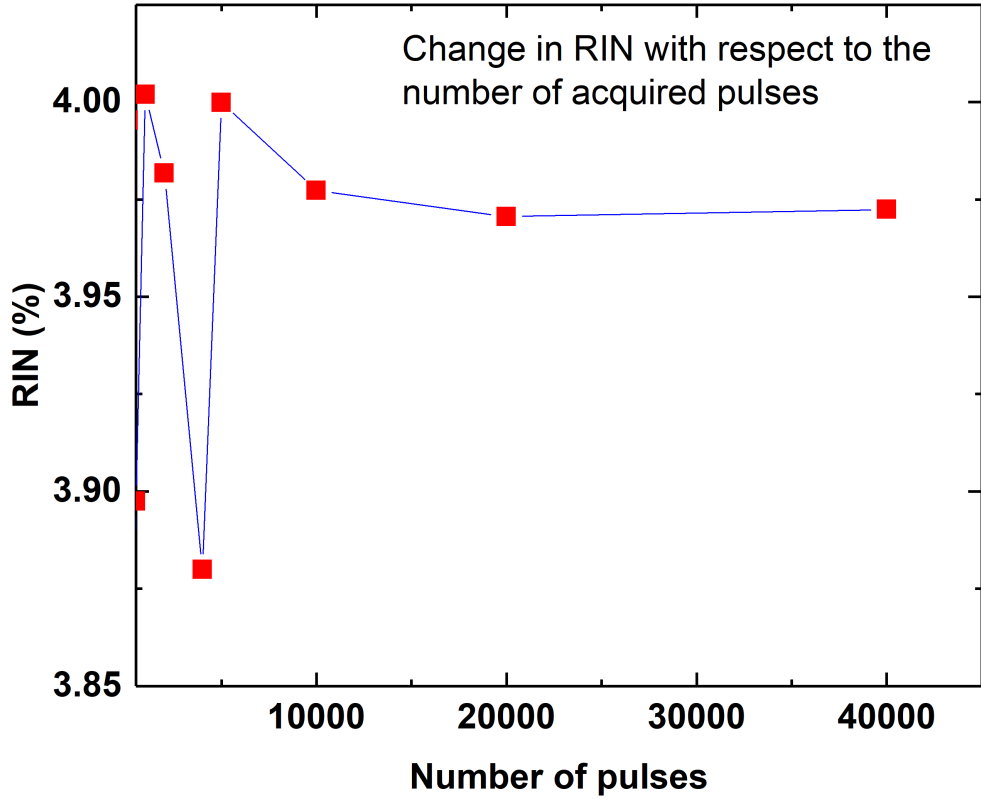


Figure 3.4: Plot of measured RIN variation with changing number of pulses.

the Nyquist criteria determined by the pulse shape, we assume that the bandwidth of the photodiode is more than twice as fast as the repetition rate of the laser source and that the pulse duration is shorter than the rise of the photodiode. Moreover, if the response or voltage trace on the oscilloscope lies in a linear range then these traces directly reflect the filtered SC variation. The common minima which is the noise floor for the trace pulses are deducted from the fluctuating maxima. The RIN can therefore be computed from the series of measured maxima as

$$RIN = \frac{\delta U}{\langle U \rangle} \quad (3.1)$$

where δU is the standard deviation and $\langle U \rangle$ is the mean value of U .

3.0.3 Configuration for supercontinuum source

Fig. 3.5 shows the configuration of the MOPA used in the experiment. The seed of the MOPA is based on a distributed feedback laser (DFB) operating at 1550 nm. Using the inbuilt electronic system the seed is modulated by intermittently changing the current fed to the laser. This yields a seed pulse duration of approximately 1 ns and a variable pulse train from 10 kHz to 35 MHz. The average power is approximately 700-1000 μW depending on the repetition rate as an increase in repetition rate generally yields a high average power. The seed is then amplified in two stages using a double-clad polarization-maintaining (PM) erbium-doped (Er) fiber which is pumped at 980 nm by splitting the pump into 30/70 % configuration to avoid gain saturation and amplified spontaneous emission (ASE). In the first amplification stage, an average power of 20 to 30 mW is achieved and upon further amplification, we achieve about 100 to 120 mW of average power. This becomes the seed for the third stage amplification.

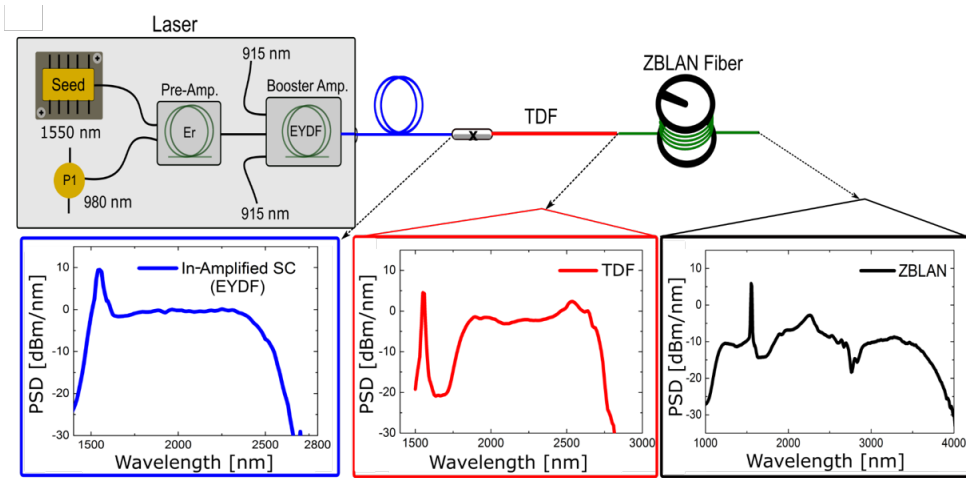


Figure 3.5: (a) Schematic diagram showing the concatenated fibers based on the MOPA configuration. The seed is based on a direct current modulated DFB seed operating at the telecommunication wavelength of 1550 nm. The pulse duration is fixed to approximately 1 ns and a variable repetition rate of 10 kHz to 35 MHz. The seed is amplified in two stages to achieve an average power between 100 to 120 mW depending on the repetition rate. At the third stage of amplification we achieve a spectrum spanning 1400 to 2400 nm which is then shifted by TDF to 2800 nm and shifted further by ZBLAN to 4000 nm.

The second stage is fed to an erbium-ytterbium codoped fiber (EYDFA) (PM-

EYDF-12/130-HE, Coherent Nufern) pumped at 915 nm to excite the ytterbium ions which then transfer its energy to the erbium ions for emission at 1550 nm. The core of the fiber is approximately 12 μm and a cladding 130 μm . The exponential amplification relative to the small core diameter leads to nonlinear effects setting in leading to the generation of a broad spectrum from 1400 nm to 2400 nm referred to us as in-amplified supercontinuum generation. The EYDFA is then spliced to about 30 cm piece of a single-mode double-clad TDF (DCF-TM-10/120, Core active) with core and cladding diameters of 10 μm and 120 μm respectively. The TDF has a core and clad numerical aperture (NA) of 0.22 and 0.45 respectively and has a clad absorption of 4.0 dB/m at 790 nm. The function of the TDF fiber is to absorb the light around the pump and redistribute it to longer wavelengths, a mechanism that will be looked at in detail in the subsequent sections. Here, we further extend the spectrum to approximately 2800 nm. The TDF is spliced to about a 15 cm long passive mode matching fiber to enhance coupling efficiency to the subsequent fiber. The output is butt-coupled to a 7.5 m passive ZBLAN fiber (ZSF - 7.0/125, Fiberlabs) which further shifts the spectrum to 4000 nm. Two repetition rates (100 and 200 kHz) were used and the measured average power from the EYDFA are 1.4 and 1.8 W, TDF 0.9 and 1.2 W and that of ZBLAN was 0.4 and 0.7 W respectively.

3.0.4 Numerical computation of the dispersion of the fibers

The dispersion of the fibers plays a vital role in the SSFS as there should be as many of the solitons above the ZDW of the fiber as possible. We show in Fig. 3.6 the computed dispersion profiles using the full vectorial finite element method based on the COMSOL Multiphysics software of all the fibers used in the cascade. The fibers were modeled using the Electromagnetic Waves-frequency Domain interface. We only considered the fundamental EM model of the propagating light. With this, we could compute the effective refractive index at different excitation wavelengths and also the profile of the refractive index. The 2-D cross-section of each fiber was built in COMSOL also taking into consideration the ion dopant concentration which modifies the refractive index profile earlier reported in [123]. We calculated the material dispersion of each of the fibers using the Sellemier's equation 2.10 considering all three fibers are step-index fibers (SIF's). The NA of the fibers were calculated from the relation

$$NA^2(\lambda) = n_1^2(\lambda) - n_2^2(\lambda) \quad (3.2)$$

where n_1 and n_2 are the refractive indices of the core and cladding respectively [124]. From the computed dispersion profile it is evident that the EYDF exhibits ZDW at 1250 nm and that pumping at 1550 nm is well above the ZDW of the fiber. In a similar manner TDF exhibit a slightly lower ZDW than EYDF which is also good to have many solitons that will be amplified through absorption/emission processes and continuously red-shift in the subsequent fibers. The ZBLAN fiber has a higher ZDW around 1600 nm which in principle has already been mitigated by the introduction of TDF to amplify and redistribute most of these solitons above its ZDW.

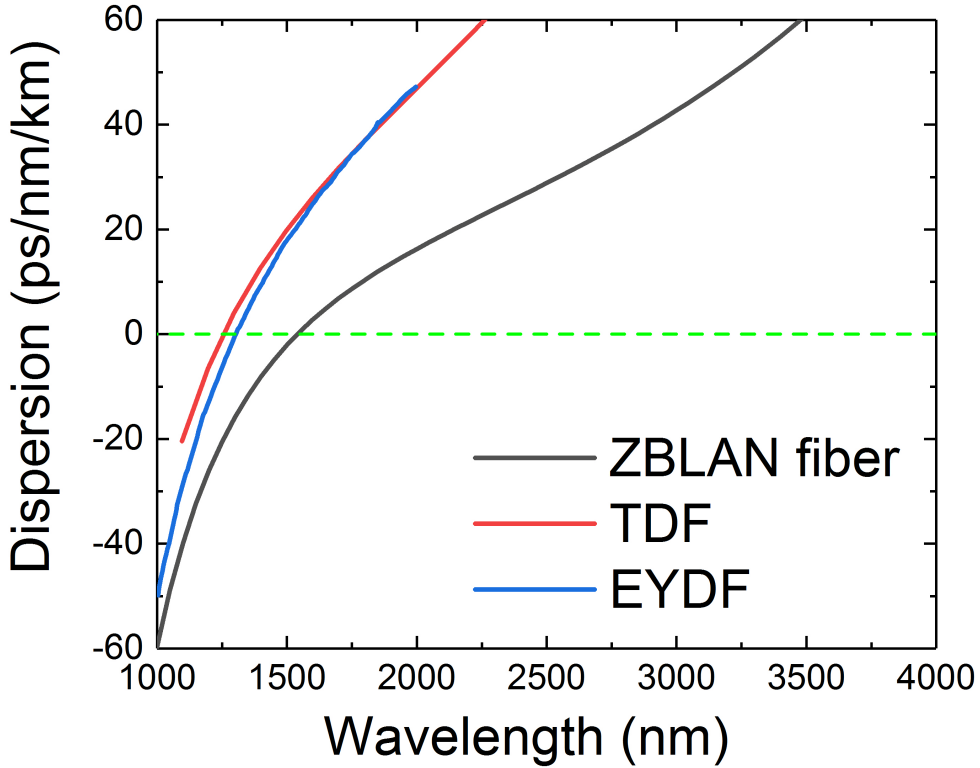


Figure 3.6: Computed dispersion profiles of the fibers used in the cascade.

3.0.5 General explanation of mid-IR SC generation

The mechanism underlying supercontinuum generation using the cascading scheme is pictorially shown in Fig. 3.7 using relatively long pump pulses (picosecond to nanosecond regime). The requirement for mid-IR SC is to pump above the ZDW of the fibers in the cascade. For standard silica, the ZDW is approximately 1300 nm so pumping with a 1550 nm pump is a good choice. The SC generation is initiated by noise-induced modulation instability caused by small perturbations originating from pump noise or inhomogeneities in the fiber. This leads to pulses breaking up into a sea of solitons of several orders which continue to red-shift [59, 112]. The dispersion profile of the fiber should be such that it exhibits both normal and anomalous regimes. The solitons will continually red-shift in the anomalous region mostly due to the stimulated Raman scattering effect [59]. Since the solitons formed have different amplitudes and duration mostly related to properties of the starting pulse, they will traverse in the fiber with different velocities (long wavelengths have a slow group

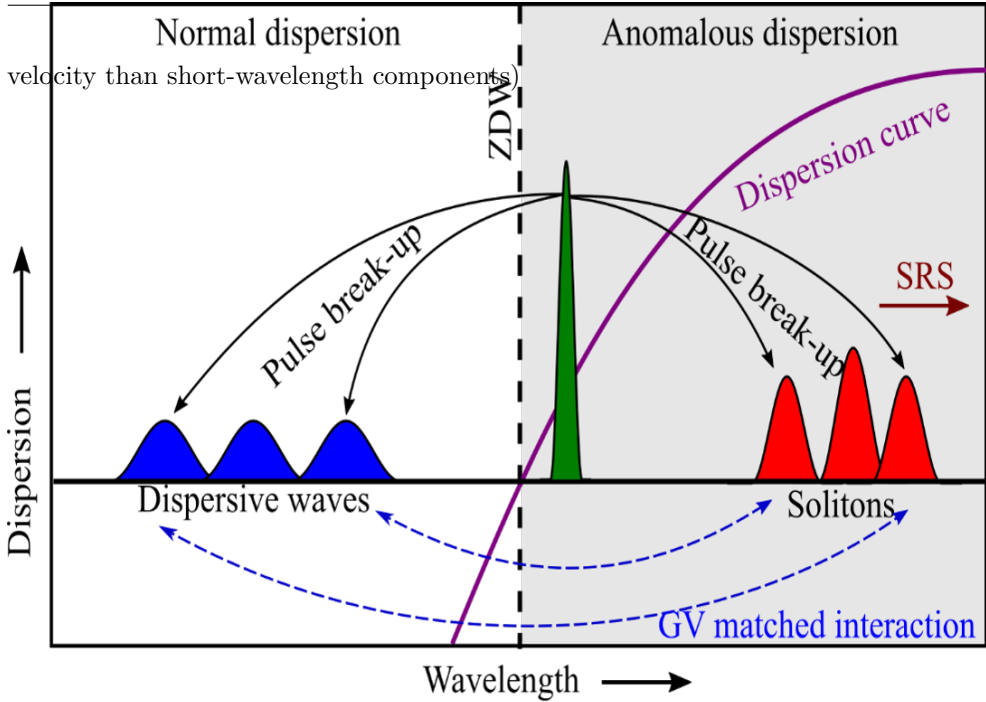


Figure 3.7: The general description of mid-IR supercontinuum generation pumped by relative longer pulses (picosecond to nanosecond regime) in the anomalous regime.

The collision among solitons leads to an energy transfer from much weaker solitons to much stronger solitons. The red-shifting solitons are group velocity matched to dispersive waves in the shorter wavelength region where the solitons shed part of their energy to the dispersive waves. This extends the mid-IR SC into blue region and mostly dominated by dispersive waves. In most cases, these dispersive waves are trapped by cross-phase modulation (XPM) from the red-shifting and decelerating solitons and thus, blue-shift [14]. The combination of the red-shifting solitons and blue-shifting dispersive waves form the entirety of the bandwidth of the mid-IR SC generated.

It is imperative to add that the contribution of the dispersive waves in cascaded mid-IR SC generation is almost insignificant [112]. To continually increase the bandwidth of the SC generated, we need the most energetic solitons to continuously red-shift in subsequent fibers [112]. These solitons may lose energy as described earlier through collisions and fiber imperfections and are therefore amplified along the cascade using gain fibers. This effect also increases the rate of red-shift quite significantly as the amplitude of the solitons increases leading to a shorter duration to conserve energy. It is therefore important to avoid the dispersive waves in the early part of

the cascade which is achieved by pumping a little further above the ZDW of the first fiber in the cascade.

3.0.6 Thulium doped fiber absorption emission processes

The loss of energy of the solitons calls for a mechanism to replenish the energy. This is achieved through the introduction of gain fibers which not only restore the soliton energy but also increases the bandwidth of the SC generated. In special cases, by the novel addition of dopants to the rare-earth ions, the absorption and emission profiles are altered leading to a shift in the absorption profiles to a few nanometers [125]. This is important where we significantly want to reduce the residual peak power initially used in the cascade which damages soft and fragile fibers in the subsequent cascade. In this section, we focus on the absorption emission characteristics of Tm ions taking into consideration the relevant transitions employed in the mid-IR SC generation. To characterize the transition of the TDF fiber used, a conventional cut back method was employed to measure the ground state absorption (GSA) using the NKT SuperK compact (450-2500 nm, 22 kHz repetition rate, and an average power of 80 mW) white light laser. The output spectra from 3, 1, and 0.5 m TDF was normalized with the laser output spectrum. To observe the excited absorption bands of the TDF fiber, a home built in-amplifier SC source spanning 850-2600 nm with a residual peak at 1000 nm due to ytterbium co-doping with erbium, average power of 517 mW and a repetition rate of 10 kHz was used. These transition bands are shown in Figs. 3.8 (with the GSA in green and ESA in blue). Fig 3.9 (b) shows the output spectra of the amplifier (in blue) before coupling into the TDF fiber (in red).

From Fig. 3.8, it is evident that TDF have much narrower but relatively much higher GSA transitions at the shorter wavelength region (higher frequencies), and these transition cross-sections increase towards longer wavelengths (lower frequencies) which is well explained by the McCumber's theory shown in equation [126]. This theory has been developed for phonon terminated lasers whose operations are based on metal ions. The temperature-dependent parameter ϵ which is the energy required to excite an ion from one energy level to the other scales the cross-section spectra relative to each other. The relative difference between the absorption and emission can be seen in the parameter $v = \epsilon/h$ where at a particular frequency the two spectra are the same. This theory is ideal for providing spectral information and can be used to generate one spectrum so long as the inverse spectrum is known.

$$\Sigma_{b,a}(V) = \Sigma_{a,b}(V) \exp\left(\frac{\epsilon - hv}{kT}\right) \quad (3.3)$$

At a particular wavelength, the gain and absorption for two Stark manifolds can also be described by McCumber theory given by

$$\frac{g^*(\lambda)}{\alpha(\lambda)} = \exp\left[\frac{hc}{kT} \left(\frac{1}{\lambda} - \frac{1}{\lambda_0}\right)\right] \quad (3.4)$$

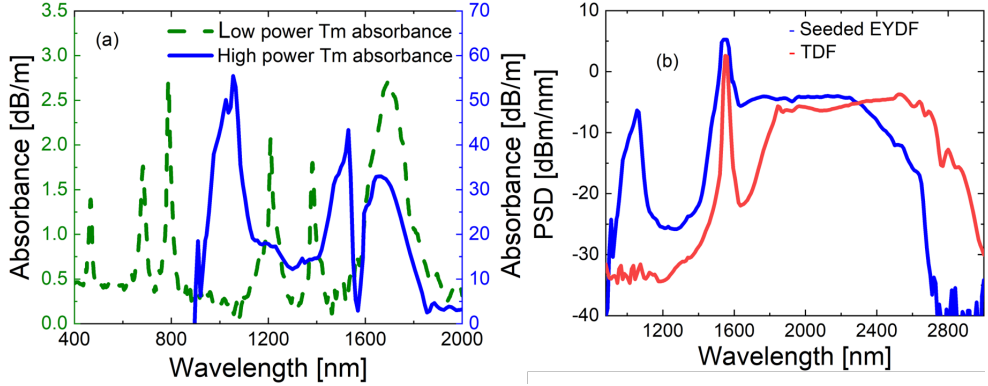


Figure 3.8: (a) TDF measured absorbance using an NKT SuperK compact SC (spectrum spanning 450-2400 nm) source with an average power of 80 mW and a repetition rate of 10 kHz (green dashed line) and a high power SC source (solid blue line) with about 517 mW of average power operating at 10 kHz (spectrum spanning 850-2600 nm) using the conventional cut-back method. (b) Measured PSD out of the EYDFA stage (in-amplifier SC)(blue) and TDF (red) respectively.

where h is the Planck's constant, k is the Boltzmann's constant, c is the speed of light, T is the temperature in Kelvin, λ_o is the crossover wavelength where the gain at the excited state equals the loss at the ground state. This equation holds and can be used to describe all transitions in rare-earth-doped metals including EDFAs and TDF used in this work. The TDF fiber exhibits ground state absorptions at 460, 650, 790, 1200 and a very broadband absorption at 1600 nm. This broadband absorption is as a result of the many Stark components that are parked in a single manifold within the transition [73]. The existence of a non-characteristic transition of TDF at 1300 nm can be attributed to aluminum ions which are added to enhance the Tm-ion dispersion during fabrication to avoid clustering effects.

The high power ESA characterization has a band at 1450 nm region which agrees with previous absorption measurements of the TDF [127] whereas an important ESA band exist around 1000 nm which coincides with the ytterbium emission band. Whiles the Figs. above give a general description of all the possible absorption/emission bands of TDF, we have summarized the possible absorption/emission transitions that give rise to the soliton amplification and possible extension of bandwidth in the supercontinuum generation in Fig 3.9. From the Fig., a GSA of thulium ions around 1600 nm from the 3H_6 manifold to the 3F_4 manifold can lead to a possible emission at 1800-2100 nm band and accounts for the first broad emission band of the SC generated. A populous 3F_4 manifold with thulium ions can lead to a non-radiative exchange of energy between the ions through energy transfer up-conversion (ETU) to the 3H_4 and

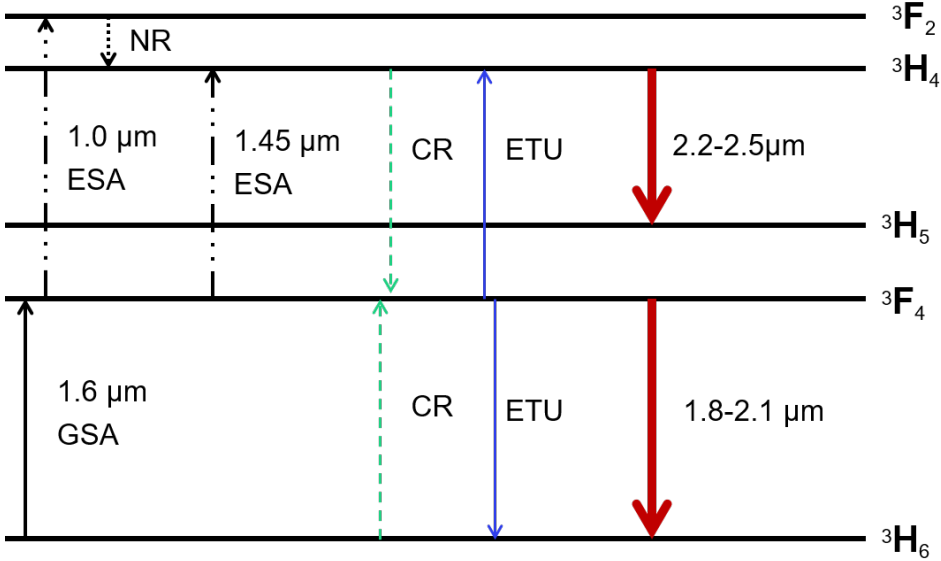


Figure 3.9: (a) Energy level diagram showing the various possible transitions in Tm^{3+} ions excited simultaneously by a broadband source. Depicted in the Fig. are GSA (Ground state absorption, ESA (Excited state absorption) mechanisms like ETU (Energy transfer up-conversion), CR (cross-relaxation) and NR (non-radiative energy transfer).

3H_6 states as clearly depicted in Fig.3.9. This can lead to a possible transition from the 3H_4 to 3H_5 manifold leading to a broad second emission window at 2200-2500 nm. A contribution to this emission window is ESA of 1450 nm from the 3F_4 energy level to the 3H_4 and cross-relaxing to the 3H_5 energy level. In the same way, there can be ESA of the 1000 nm ions to the 3F_2 energy level and non-radiatively relaxing to the 3H_4 energy level and finally emitting to the 3H_5 energy level. These processes can contribute to both the first and second emission windows.

3.0.7 Pulse Amplification Relative to Bandwidth of SC

We show an overlay plot of the measured PSD and the noise profile out of the EYDFA and TDF at 100 kHz and 200 kHz repetition rates.

The RIN curve in both instances shows a relatively low RIN for almost the entire bandwidth of the SC generated from the output of both fibers. To get a deeper insight into the origin of the low noise, we investigate both the RIN and PSD profiles along the cascade beginning from the EYDFA and TDF focusing much on the spectral

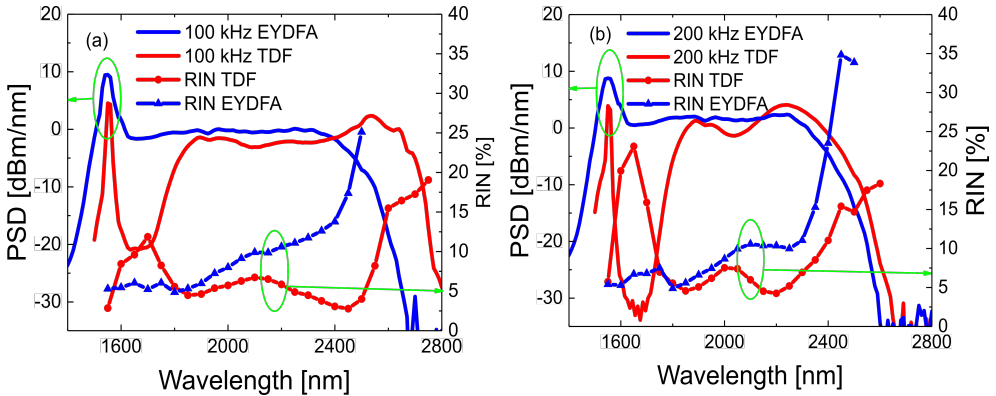


Figure 3.10: Overlay plot of experimentally measured PSD (solid line) and RIN (symbol run through by lines) from the output of EYDFA (blue/triangle) and TDF (red/circle) with a laser repetition frequency of (a) 100 kHz and (b) 200 kHz respectively.

region above 1500 nm. These results are shown in Fig 3.10 at two repetition rates of 100 and 200 kHz with an average power of 1.4 and 1.8 W respectively. A direct comparison of the average power gives a ratio of 1.56 which is an indication that the total continuum energy at 100 kHz is a factor of 1.56 higher than at 200 kHz. Moreover, a direct computation of the soliton number shows a factor of 1.25 larger at 100 kHz to 200 kHz when we assume that the fraction of residual pump and non-solitonic radiation is almost the same in both repetition rates. A much closer look at 3.10 shows that the bandwidth of the PSD in the 100 kHz case is few nanometers larger than that of the 200 kHz case. This is well explained that the bandwidth of MI-based SC is much more dependent on the number of solitons for a given fiber length [59]. This is observed in both EYDFA and even much more pronounced in TDF. The even pronounced bandwidth in TDF can also be complemented with the underlying absorption/emission dynamics explained earlier.

The average power increases much more significantly for a doubled rep. rate under the same continuous wave (CW) pumping. We can therefore conclude that we operate the laser in the unsaturated regime and at this point, each pulse does not fully deplete the already achieved population inversion. Upon reduction of the rep rate, it takes much time for the amplifier to recover its population inversion which leads to a higher per pulse gain of the train of pulses but also an increase in ASE as well as parasitic gain [128]. The dynamics are somewhat different in TDF as population inversion is not achieved with the CW pumps. The gain is thus, induced by the arrival of the first pulse and reaching a steady-state by the continuous arrival of several pulses which in most cases referred to us as the concept of tandem pumping [129]. Besides the

number of solitons that are directly related to MI-based SC, low rep. rate pulse does carry much pulse energy and thus provides stronger amplification for incoming pulses leading to increased broadening in the TDF fiber.

From the RIN curve in Fig.3.10, and considering the EYDFA stage, the RIN at the pump is at a relatively low % of about 5 % and increases to about 30 % along the edges of the SC considering a - 20 dBm/nm from the pump edge around 2500 nm. This trend is not different from standard SC sources whose generation is initiated by MI leading to the formation of solitons and dispersive waves [114]. The high RIN at the edges is a result of the non-deterministic occurrence of rare events such as rogue waves and low signal to noise ratio (SNR) which is an established phenomenon in the mid-IR SC community [34, 114]. The less variation in the soliton self-frequency shifting within the region 1500-2300 nm part of the spectrum leads a low RIN remaining around 5-10 % though narrow bandpass filtering of approximately 5 nm was achieved within this region (see Fig. 3.1). This dominant effect of SSFS variation is also complemented by spectrally overlapping solitons which reduces the noise through soliton averaging.

A much closer look at PSD and RIN of the TDF reveals spectral dip within the absorption region of 1600-1800 nm region which has already been shown in Fig. 3.8. This strong absorption by TDF reduces the SNR very significantly within this window to about 20-30 dB and thus, a higher RIN in this region. But more interesting is the fact that the introduction of TDF in the cascade strongly reduces the RIN above 1800 nm region in both rep. rates after the TDF absorption. This is as a result of amplification of solitons which conserves energy by increasing their amplitude and narrowing the temporal width. This leads to a much faster rate of red-shifting of the solitons in the region of 1800-2100 nm. The second emission band in the region of 2200-2500 nm will further amplify the solitons that are already within this region and having red-shifted from the first amplification window leading to a more pronounced SSFS. This pushes the solitons towards the loss edge which in effect increases the bandwidth of the SC generated.

The existence of the two gain bands is of importance as it is the cause of the low RIN above 1800 nm. As can be seen, the absorption window leaves an absorption band within that region, one would have assumed that there should have been a similar dip in the second absorption window around (2200-2500 nm). Whiles this fits for the 100 kHz case, this is entirely not the case for the 200 kHz case but rather the dip starts quite early above 2000 nm.

There is a correspondence between the presence of the ER gain band and the generally low RIN posed by the EYDFA. This can be seen from Fig. 3.11 that a commercial SuperK EVO SC source from NKT Photonics which is based on a ytterbium 1064 pump and amplifier pumping a PCF has significantly higher RIN compared to our source. The commercial NKT SuperK EVO industrial white light laser has an on-time average power of 3.4 W, operating at a pulse rep. rate of 20 MHz and the RIN curve marked in blue in Fig. 3.11b. The RIN curve in both instances have been measured using the same system and employing almost the same parameters used for our laser RIN measurement and we can therefore say it is fair to compare the two laser sources. The commercial laser source exhibits a RIN above 5.5

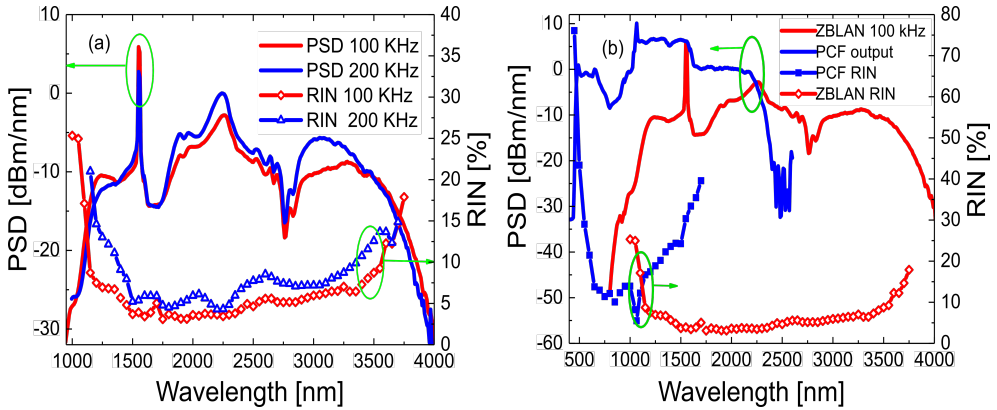


Figure 3.11: (a) Overlay plot of the experimental measured PSD (solid lines) and RIN (symbols with lines) out of ZBLAN fiber at the rep. rates of 100 kHz (red) and 200 kHz (blue). (b) Overlay plot of experimental measured PSD of 100 kHz setup (red) for ZBLAN fiber output and the corresponding values for a 20 MHz SuperK EVO laser source. The source is based on a ytterbium-doped fiber amplifier pumping a silica PCF.

% at all wavelengths and the minimum RIN was achieved at the pump wavelength. This is a little bit on the high side compared to our laser source make our source much useful for applications like spectroscopy and microscopy. Whiles, it is important to acknowledge the low noise, it is also important to consider the influence of the filter bandwidths used in the experiment. It seems feasible that a much broader filter bandwidth will reduce the RIN but there is only an isolated case of the RIN change at 2500 nm for the 100 kHz case due to a filter bandwidth jump from 5 to 25 nm. This anomaly is not seen in the 200 kHz case and generally the noise increases around 2500 nm. This seems to debunk the earlier suggestion of a larger bandwidth leading to a smaller RIN and that there are nonlinear factors which tend to also dominate in the RIN dynamics and that for a bandwidth of 5-31 nm we are in the regime where we can neglect the influence of filter bandwidth on RIN.

3.0.8 Theoretical Modelling of noise

The contribution of the soliton dynamics in the generation of the SC is important, hence, a deeper understanding of these issues was complemented with numerical modeling to the experimental results. For simplicity, we tune the parameters to suit the 200 kHz rep. rate which has a relatively low per pulse gain. This is a reasonable approximation because the gain can be assumed to be uniformly distributed along

the length of the EYDFA and TDF. Modeling of the spectral evolution along the length of the fiber in the first two stages of the cascade was performed by solving the generalized nonlinear Schrodinger equation (GNLSE) employing the fourth-order Runge-Kutta integration scheme in the interaction picture and an adaptive step size [36, 130]. A temporal resolution $dt = 0.92$ fs with a 2^{19} time sampling points were used in all simulations. The conventional random phase noise and standard one-photon-per-mode were added to the initial conditions in the Fourier domain whereas a laser amplitude noise of about 1 % was also added to the amplitude of the input pulse [131]. Because the seed of our in-house built mid-IR SC source laser being a directly modulated laser diode, noise was only added to the amplitude. This would have been different for a mode-locked laser in which case, the anti-correlation of noise in the pulse length should also have been added [131]. The PSD spectra shown here are an ensemble an average of 72 simulations employing random noise seeds. To emulate the experimental PSD recorded using the optical scanning spectrometer used in the experiment, the PSD's are plotted with a 10 nm running average. A Gaussian-shaped 5 nm and 24 nm broad filters for wavelengths < 2500 nm and > 2500 nm respectively also to mimic the filters used in the experiments as discussed in the previous section were also used.

A Gaussian pulse envelope with peak power of approximately $P_0 = 470$ mW which was specifically chosen to match the experimental peak power of the 1 ns experimental pulse duration seed was part of the initial pulse characteristics used for modeling the SC generated in the first cascade (EYDFA). The simulated pulse duration used was reduced to 20, 40, and 80 ps which was necessarily chosen to maintain a high spectral resolution as well as a much reasonable computation time. Though the pulse duration was reduced, we still were in the region where the SC generated was initiated by MI with the corresponding maximum MI gain being

$$g_{MI} = \gamma P_0 \quad (3.5)$$

where $\gamma = 1.8$ (Wkm) $^{-1}$ is the EYDFA non-linearity at the pump wavelength. We, therefore, matched the peak power of the simulated and experimental parameters instead of matching the pulse energy or the soliton number while using 3 progressive pulse duration to study the general trend when moving to longer pulses and getting closer to the nanosecond regime. For both the EYDF and TDF step-index fibers, their dispersion could be computed from the refractive index of pure silica and its NA by employing the step-index eigenvalue equation [124].

Earlier suggestions by Thirstrup et al. [123] showed the effects of rare earth dopants and other ion dispersing dopants on increasing the refractive index of the fiber. Such passive effects (outside the absorption/emission regions) that modify the dispersion of the fibers was neglected in our simulations. The emission and absorption transitions with certain bands were included as gain and loss respectively and were assumed that the gain and loss were adiabatic along the length of the fiber. Using the Kramer-Kronig relations, we included the effect of the 1550 nm gain. All other absorption and emission gain bands were neglected. The CW 915 nm backward pumping of

the EYDFA was not included in the modeling. An erbium gain peak of 6.7 dB/m was empirically determined by comparing the simulated output spectrum to the experimentally measured spectrum having already taken the Er gain profile from [73]. Shown in Fig. 3.12 (a) are the EYDFA gain profile and its relative effect on the dispersion. It is worth noting that the Raman Stokes peak located at $\Gamma_{RAMAN} = 1663$ nm lies outside of the Er gain band. Moreover, the MI Stokes peak of the input can be located at

$$\Lambda_{MI} = \frac{2\pi c}{w_0 - \Omega_m} = 1560nm \quad (3.6)$$

where

$$\Omega_m = \left(\frac{2\gamma P_0}{|\beta_2|} \right)^{1/2} \quad (3.7)$$

In our configuration, the TDF has no dedicated amplifier with external CW pumps,

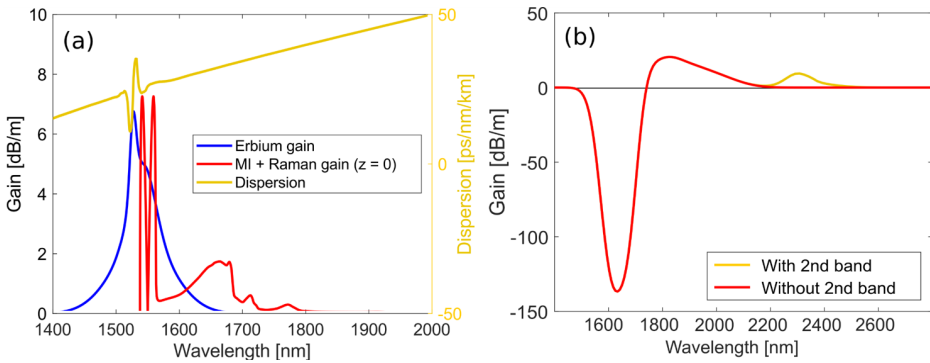


Figure 3.12: (a) Experimental and simulated results of the EYDF and TDF (a) Erbium gain band, MI + Raman gain and dipersion of the fiber TDF gain with and without the second absorption band.

so here the output of the EYDFA acts as a seed for excitation of the Tm ions which is mostly done by the 1550 nm pump. De-excitation of the Tm ions is mostly by stimulated emission. From the manufacturer's data of the TDF, it is 7 % doped by weight, thus, the peak core absorption at 1600 nm was computed to be 137 dB/m whilst the first emission band peaking at 1900 nm was modeled with a gain of 20 dB/m [132]. The second emission band at 2300 nm was modeled with a gain of 9 dB/m or 0 dB/m to investigate the effect of second emission window on the soliton dynamics. The plot of the gain spectrum is shown in Fig 3.12 (b).

Shown in Fig 3.13 are the results of the Sc generated from a 3.5 m EYDFA and a 25 cm piece of TDF. From Fig. 3.13 (a) we can see that the experimental and simulated results of the PSD and RIN from the EYDFA approach each other quite

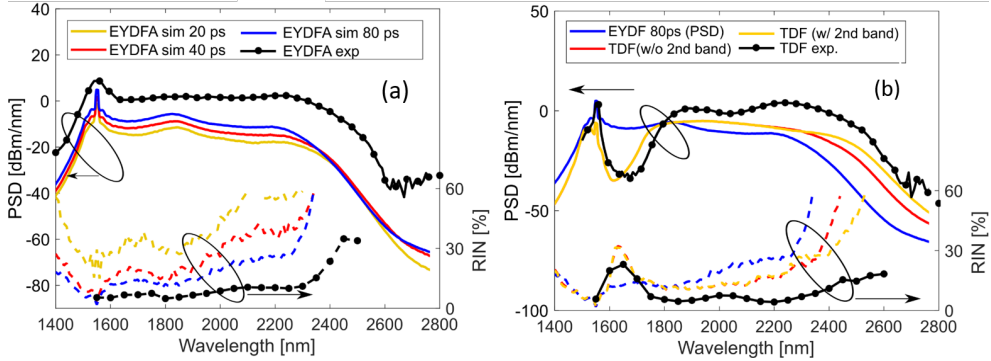


Figure 3.13: (a) Experimental and simulated result of the EYDF and TDF PSD and RIN (a) EYDF output with varying pulse duration compared with the experimental results (b) TDF output at 80 ps with and without the second absorption band compared with experimental TDF output.

well (given by black curves) as the pulse duration is increased from 20 to 80 ps. There is an agreement of both simulations and experiments at the red edge of the curve where the difference between the 80 ps and 1 ns pulses of identical amplitude is approximately 11 dB of the PSD. we can therefore say that the 80 ps simulation gives a well qualitative description of the dynamics that leads to the generation of the SC at 1 ns pump.

From Fig. 3.13 (b) which describes the TDF scenario, we can also see the good agreement of both the simulated and experimental results. Striking of such similarities is the absorption around 1600-1800 nm which has created a dip in PSD and a subsequent increase in the RIN. Moreover, there has been a red-shift in the red spectral edge and we can also see that the RIN out of the TDF is relatively lower than the RIN at EYDFA at wavelengths above 1800 nm where the Tm emission bands start. The inclusion of a second gain band in our simulations seems to increase the red edge bandwidth to about 50 nm and subsequently lowers the RIN above 2300 nm which further collaborates the simulated and experimental results. We can therefore agree on our previous assertion that absorption/emission dynamics coupled with the amplification of the solitons lead to SSFS induced red-shift and more importantly leading to the lowering of the RIN. This is well explained that, a fundamental soliton will reduce its pulse duration adiabatically and also increase the amplitude to keep its soliton number fixed to 1 which leads to an increase in the rate of red-shift.

Having been able to ascertain the correlation of both experimental and simulated results, we now look deeper into the Physics of the SC generation by looking at the RIN and PSD evolution along the fiber length in both the EYDFA and TDF in Figs 3.14 (a-d) and Figs 3.15 (a,b). It is shown in Figs. 3.14 (a-d) the spectrograms of

the output fiber PSD with 3 dB/nm emission and gain bands shown in green and red respectively. This has been determined as the width of the absolute level. Owing to

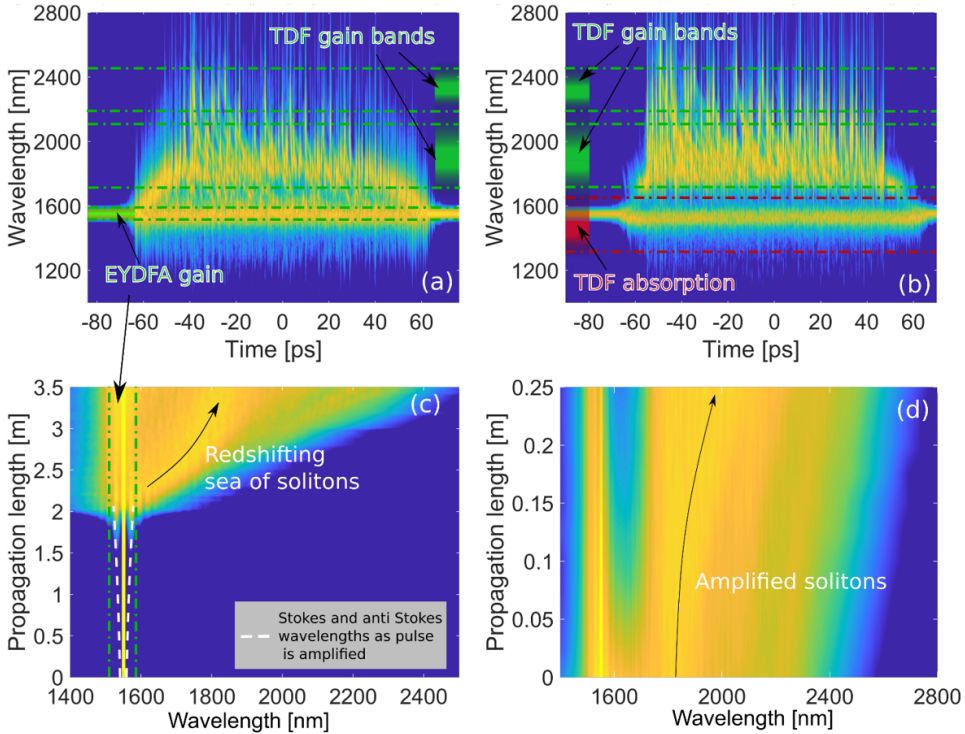


Figure 3.14: (a) Experimental and simulation results of EYDFA and TDF showing, (a) the spectrogram of EYDFA (b) the spectrogram of TDF (c) PSD evolution along EYDFA.

the gain (approximately 5 dB/nm at the pump) the pump power increases gradually leading to a shift of the MI Stokes wavelength as has been shown in the white dashed line in Fig. 3.14 (c). Within a short length of about 2 m of the fiber, the pump peak power has increased exponentially to $P_0 = 4.7$ kW. This thus, shifts the MI Stokes band to approximately 1580 nm but still well within the Er gain band. Since the MI bands lie within the Er gain band, it will amplify and speed up the MI process as well as all solitons that are generated within this band and subsequently increasing the SSFS induced redshift. Within 2 m of the fiber length, where the pulse is almost about to break up, with a peak power of $P_0 = 4.7$ kW and a pulse duration of 80 ps, the calculated pump soliton number $N = 225$. In passive fibers for standard SC sources where MI initiates the generation of a packet of solitons, these solitons will stay closer to each other for a long distance. There is thus, energy transfer among these solitons

through multiple collisions and therefore create larger solitons and enhances the SSFS. What we see in our case is in sharp contrast to what is generated in these passive fibers. Since the solitons are generated within the gain region, they will experience gain and will be forced to rapidly red-shift away from the pump. These red-shifting packet of solitons are marked by an arrow in 3.14 (c). This rapid redshift leaves a void at a wavelength above the gain band. From the spectrogram in Fig. 3.14 (a) we can see that dispersion and fiber length greatly affects the spectral width of solitons. Within the region where the packets of solitons are aligned would have a high SNR which invariably leads to a lower RIN which is shown in Figs 3.13 (a) and 3.15 (a), mostly in the region around 1800 nm in both the numerical and experimental results. This local dip is not as a result of high SNR but also due to the alignment of the solitons due to the Er gain. This effect has already been demonstrated in fibers that are under-tapered and leads to the alignment of the solitons imposed by the second ZDW of the taper moving into the SC [36]. This alignment of the solitons within a particular region has clearly been shown in Fig 3.14 (a)

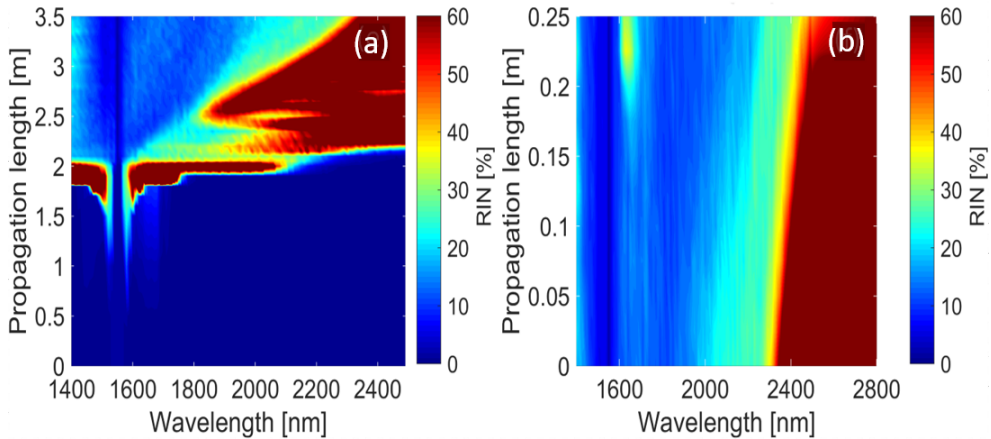


Figure 3.15: (a) Experimental and simulation results of EYDFA and TDF showing, (a) evolution of RIN along EYDFA (b) the evolution of RIN along with TDF.

Similarly, the absorption band of the TDF within the region 1600 - 1800 nm will further deplete the spectrum while the two gain bands from 1800 - 2500 nm will increase the rate of redshift and impose much more spectral alignment which in effect will lower the noise above 1800 nm. We have shown this spectral dip and the continuous red-shifting solitons in Fig. 3.14 (d) and the spectral alignment can be seen in 3.14 (b). This we can convince ourselves leads to a lowered RIN which is finally transferred to a passive ZBLAN fiber for the red-shifting process to continue. This technique has provided a platform for generating broadband, low noise SC source

which can have several useful applications.

3.1 Summary

The enormous potential of making broadband, low noise SC source cannot be overlooked. Whereas there exist few platforms for generating mid-IR light sources, they are either spatially incoherent and lower in brightness like the global or may be limited to a few tunable bandwidths like in the case of the quantum cascade laser (QCL). The SC investigated in this chapter addresses these aforementioned problems.

The cascading technique where dissimilar fibers with progressively longer transmittance are concatenated have provided a platform for realizing an all-fiber, compact, mid-IR source. This may sound so easy to generate but the mechanism underlying the generation of the SC are complicated. This is due to the coupled effect of both nonlinear processes and underlying absorption/emission processes.

In this work, we experimentally and theoretically investigated the generation of a mid-IR SC based on this technique. Since the generation of such a broad SC is inhibited by noise, we have provided mitigation to noise. This we have described in this work as soliton spectral alignment which is as a result of MI happening just within the gain band of the first fiber in the cascade. This reduces the noise quite significantly and we compare this reduced noise to a commercial SC from NKT photonics. We show that our in-house mid-IR SC source though so broad in terms of bandwidth still outperforms a relatively narrow SC from a commercial NKT SuperK EVO in terms of noise.

CHAPTER 4

Power Spectral Density and Bandwidth Scaling of Supercontinuum sources

This chapter is based on the publication [19].

4.1 Introduction

The enormous potential of mid-IR broadband SC sources owing to the existence of molecular resonances within this region has led to considerable attention by researchers in this field [1, 13]. Today mid-IR SC sources are being used in applications like optical coherence tomography [133, 134], spectroscopy [110], stand-off detection [135], photoacoustic microscopy [136, 137], and hyperspectral microscopy [2]. All these applications have been made possible because of the high average power and larger bandwidth achievable in these SC sources. SCG generation into the mid-IR is quite challenging to realize. A practical way of SCG is by launching an intense laser light into long fiber to exploit the nonlinear dynamics posed by the long interaction length between the pulse and the fiber. Multi-photon absorption, however, limits the transmittance of traditional robust silica fibers into the mid-IR region. To further enhance transmittance into the mid-IR, heavier element glasses with relatively lower phonon energies are used which include heavy metal fluoride and chalcogenide glasses.

The cascading scheme offers the platform for realizing a robust, all-fiber, high power, spatially coherent mid-IR SC that covers the near to mid-IR region [1, 13, 24, 25, 112, 138]. This technique relies on concatenating the fibers in order of increasing

transmittance and subsequently continued broadening of the spectrum into the mid-IR region. Through noise seeded modulation instability, the generated solitons in the first stage of the cascade contribute to efficient broadening in the other fibers in the cascade [24, 112]. Cascading is much cheaper to realize because the scheme is based on the use of readily available telecommunication components and pump sources such as MOPA. In the MOPA configuration, the seed diode which is mostly directly modulated can have pulse durations that range from the nanosecond regime [13, 25] to the pico-second regime [139] and repetition rates that range from a few kilohertz (kHz) [13, 25] to several megahertz (MHz) [114]. The seed has a few micro-watts of average power, which is further amplified in several amplification stages to the watt level. Amplification leads to an exponential growth of the laser pulse intensity and with a small core fiber diameter, can initiate nonlinear dynamics leading to the generation of in-amplifier SC [10]. The coupled effect of gain dynamics and nonlinear dynamics makes the whole generation process complicated to decouple the effects and know which processes contribute at each stage of the process.

The technique of cascading was first demonstrated by Xia et al. [25] by concatenating silica and ZBLAN fibers but the influence of the input pulse parameters on the coupled nonlinear dynamics, the noise properties, and amplification has remained an open question. The damage threshold of the fragile soft glass fibers is relatively low compared to the more robust silica fibers and tend to decrease further as one moves more into the IR transparency region. It is therefore imperative to tailor the peak power as one moves along the cascade. Naturally, since some of the pulse energy is lost to the continuum, the peak power decreases but sometimes are still higher for the soft glass fibers to handle.

In this chapter, we provide experimental investigations into generating a mid-IR SC by employing the cascading scheme where the first in-amplifier SC from the EYDFA MOPA acts as seed. We vary pulse parameters like the pulse duration and repetition rates to see how the bandwidth, noise, and PSD of the EYDFA affects the SC in the subsequent fibers in the cascade. Most importantly by coupling the in-amplifier SC into a small piece of thulium-germanium (Tm/Ge) codoped fiber to amplify the solitons through the so-called inter-pulse self-pumping [129]. In so doing we study the noise levels of all parts of the cascade by relating it to the input pulse parameters and predicting which pulse combination regime offers the best noise performance.

4.1.1 Master Oscillator power amplifier configuration

The SCG is based on the MOPA configuration as shown in Fig. 4.1. In the configuration two directly modulated laser diodes operating at a wavelength of 1550 nm, each having a spectral width of 0.1 nm FWHM were used to vary the pulse duration and repetition rates. The first seed diode has a fixed pulse duration of 35 ps and a repetition rate that varies from 10 kHz to 50 MHz and a seed RIN of $1.0589 \pm 0.003\%$. The other seed has a variable pulse duration and repetition rate of 1 -50 ns and 10

kHz to 3 MHz respectively and a RIN $1.1103 \pm 0.004\%$. Both diodes are amplified using the same amplification setup. First, they are amplified in two stages using ER doped PM fibers of about 3.5 m long which are pumped by a single CW pump with a total average power of 600 mW power split into 30 and 70 %. The first amplification stage is pumped with the 30 % pump where we achieve an average power of 15 - 30 mW depending on the pulse parameter combination. The second split stage of 70 %

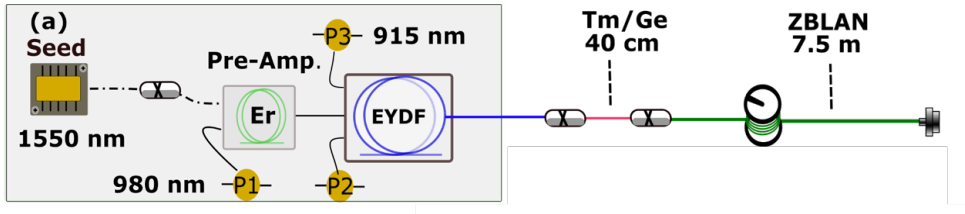


Figure 4.1: Schematic of the MOPA configuration using two seed diodes with the first seed operating at a wavelength of 1550 nm and spectral width of 0.1 nm FWHM and fixed pulse duration of 35 ps and a variable repetition rate of 10 kHz to 50 MHz. The second seed also operates at 1550 nm and has a spectral width of 0.1 nm and variable pulse duration from 1 to 50 ns and a repetition rate that varies from 10 kHz to 3 MHz. The seed is amplified in 3 stages using a series of ER and EYDF fibers and finally into a 40 cm piece of Tm/Ge fiber and a ZBLAN passive fiber.

is also used to pump the same length of the Er fiber and we achieve an average power of about 70-125 mW also much dependent on the pulse parameter combination. After the first and second amplification stages, the pulses are amplified further in about 6.3 m of an EYDF which is pumped by two 20 W CW pumps operating at a wavelength of 915 nm. Co-doping erbium with ytterbium enhances the pump to signal conversion efficiency to about 40-70 % [140], due to reduced erbium ion clustering. Thus, a much efficient way to realize the high power operation of erbium amplifiers is to co-dope with ytterbium.

The EYDF output is then spliced to a 40 cm long of Tm/Ge co-doped fiber. The Tm/Ge fiber is an in-house fiber which is fabricated from Nanyang Technological University, Singapore. It is designed to have a high absorption around the pump wavelength of 1550 nm and redistribute the absorbed photons to longer wavelengths. The residual pump in the initial cascade tends to damage the soft glass fibers in the subsequent cascade and therefore, we use the high absorption of the fiber around the pump to mitigate this damage threshold. The fiber was fabricated using the optimized modified chemical vapor deposition method (MCVD). The fiber has core and cladding diameters of $12\mu\text{m}$ and $125\mu\text{m}$ respectively. Shown in Fig. 4.2 are the refractive index profile and absorption spectrum of the fiber. A noticeable index dip from the Fig. can be attributed to the evaporation of the germanium ions during preform collapse.

It has a maximum refractive index change of approximately $\Delta n = 0.027$. The fiber has 20 wt % and 0.15 wt % concentrations of Ge and Tm respectively.

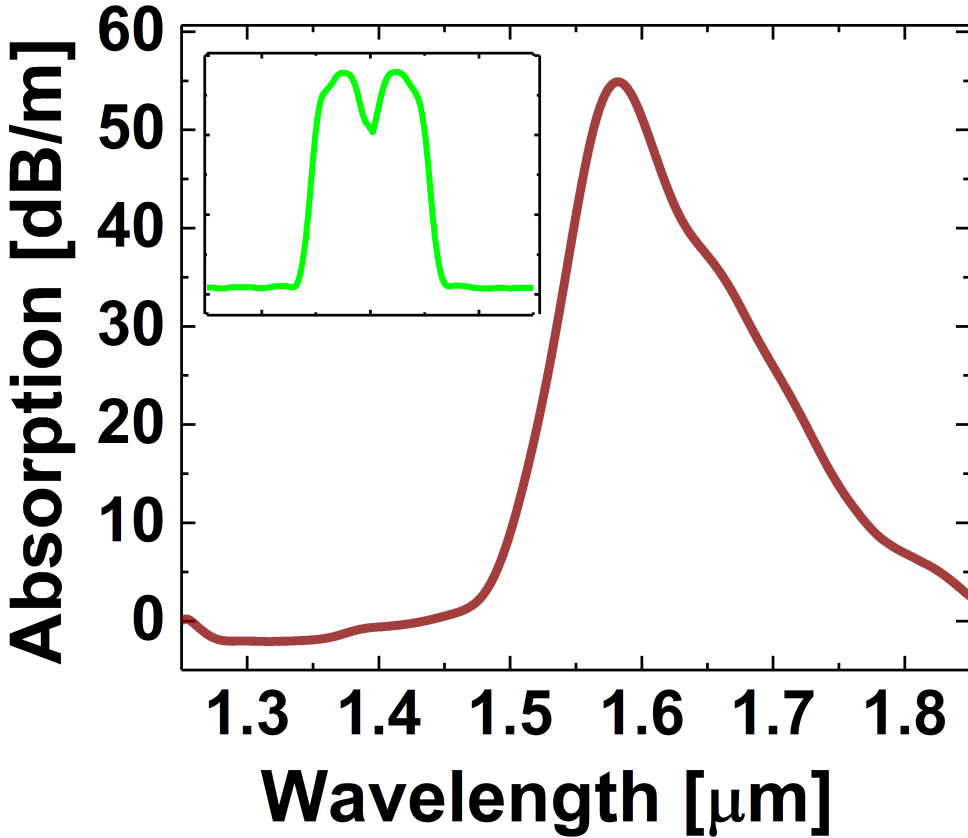


Figure 4.2: Measured GSA spectrum of the in-house Tm/Ge co-doped fiber with a peak absorption of about 55 dB/m. Inset: measured refractive index profile of the core of the fiber with a core diameter of $12\mu m$ and a maximum refractive index change $\Delta n = 0.027$.

The fiber has a peak absorption of about 55 dB/nm around 1580 nm which decreases to about 40 dB/nm around 1550 nm. Comparing the absorption of this fiber to the one used in [10] which is a commercial fiber, that has an absorption of about 10 dB/nm at 1550 nm from the manufacturer data on their website, our in-house fiber is much higher in absorption around the pump. The absorption profile of the Tm/Ge co-doped fiber is shifted a few nanometers of about 80 nm towards the 1550 nm region compared to the commercial Tm doped fiber. This is made possible by the

inclusion of Ge ions with Tm. The underlying effects of this shift though observed experimentally is yet to be investigated numerically. This strong absorption of the fiber around 1550 nm helps in reducing the residual peak power which helps achieve a flatter spectrum, increased PSD at longer wavelengths, and lastly improved power handling by the soft glass fibers in the cascade. The fiber is finally mechanically spliced to about 7.5 m ZBLAN with a core diameter of $7\mu\text{m}$ which further extends the spectrum to the loss edge of ZBLAN through SSFS.

4.1.2 Influence of pulse duration and repetition rate on bandwidth, average power, and noise.

We study the effects of the pulse duration and repetition rate changes to the average power, bandwidth of the SC generated, and noise in this section. In Fig. 4.3, at the EYDFA stage (dashed lines in both (a) and (b)) it is generally expected that increasing the repetition rate will also increase the average output power because of enhanced amplifier efficiency which will subsequently lead to a decrease in the -30 dBm/nm (0.001 mW/nm limit) bandwidth owing to a reduction in peak power of the incoming pulses. This is in principle the case for 1 ns seed but an anomaly is observed for the 3 ns seed which more or less exhibits a flattening of the curve from 500 kHz to 1 MHz repetition rates. This can be attributed to the onset of amplifier saturation. The 35 ps seed on the other hand has a relatively increased bandwidth as well as constant average power as the repetition rate increases which is an indication that there is a limitation imposed by an early occurrence of spectral broadening in the EYDF. We can also see from Fig. 4.3 that at the output of the Tm/Ge stage (dotted lines), the 3 ns seed follows the trend of the EYDF stage where bandwidth decreases but the average power shows an opposite trend when compared to the EYDF. This is as a result of the weak broadening in the EYDF stage as the repetition rate increases which leads to a reduced overlap with absorption bands of the Tm/Ge fiber. This is also corroborated by the 1 ns and 35 ps case dynamics. The bandwidth trend for the 1 ns seed and 35 ps seed cases are almost identical, there is a monotonic increase in average power for the 35 ps but there is a significant increase for the 1 ns from 100 kHz to 500 kHz. There is a drop of the average power from 500 kHz to 1 MHz which is an indication that the amplification as a result of stimulated emission at the Tm/Ge stage is limited by less broadening in the EYDF stage on one hand and the possibility of gain saturation on the hand. In the final ZBLAN case which only acts as a passive fiber, and that there is no amplification dynamics, the bandwidth, and average power follow the trend of the Tm/Ge fiber as expected.

From Figs. 4.3 (a,b) and 4.4 (a-f), we can see that the final stage of the cascade (ZBLAN) has the best performance in terms of bandwidth from the 1 ns and 35 ps seeds. This final performance can be linked with the initial bandwidth achieved at the EYDF stage. In other words, in-amplifier SC seems to be of importance in realizing the best bandwidth, average power and noise in the final SC stage. For relatively long pulses (nanosecond to picosecond), pumping above the ZDW of silica

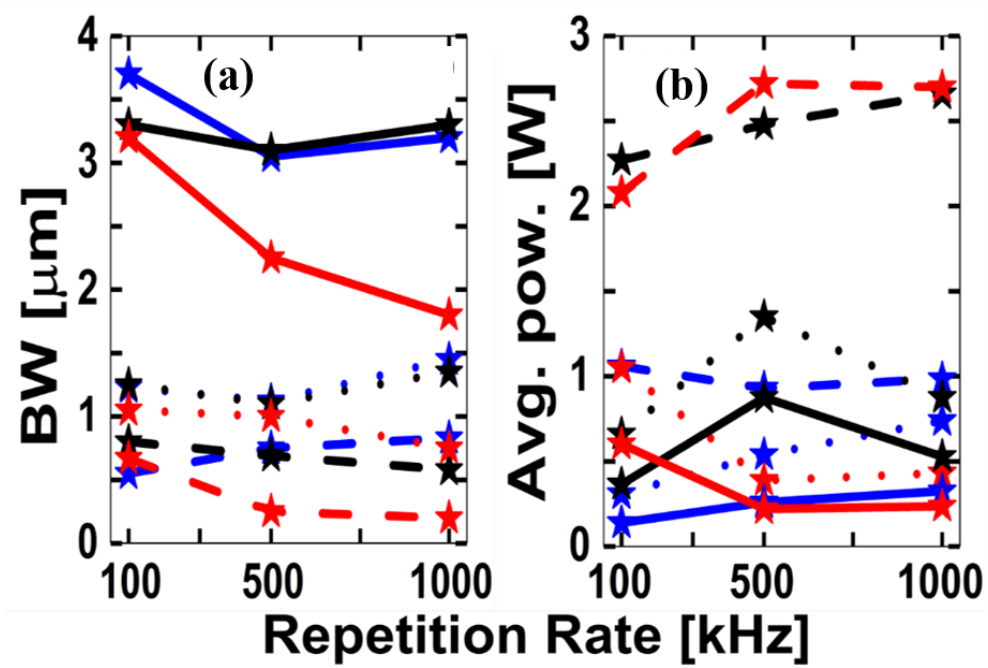


Figure 4.3: SC of -30 dB/nm = 0.001 mW/nm plot of (a) bandwidth (b) average power versus repetition rate at the output of the 3 stages of the cascade (dashed EYDF, dotted Tm/Ge, solid ZBLAN for a seed pulse duration of 35 ps (blue), 1 ns (black), and 3 ns (red)).

at approximately 1300 nm, SC is generated by noise seeded MI which eventually leads to the generation of a sea of solitons. The onset of the generation of the solitons are therefore critical in mid-IR SC generation and therefore looked into in the next section.

4.1.3 Onset of modulation instability (MI) in mid-IR Supercontinuum generation.

There is an inverse relationship between the MI gain length (L_{MI}) and the input peak power (P_{in}) given by the expression

$$L_{MI} = \frac{1}{\gamma P_{in}} \quad (4.1)$$

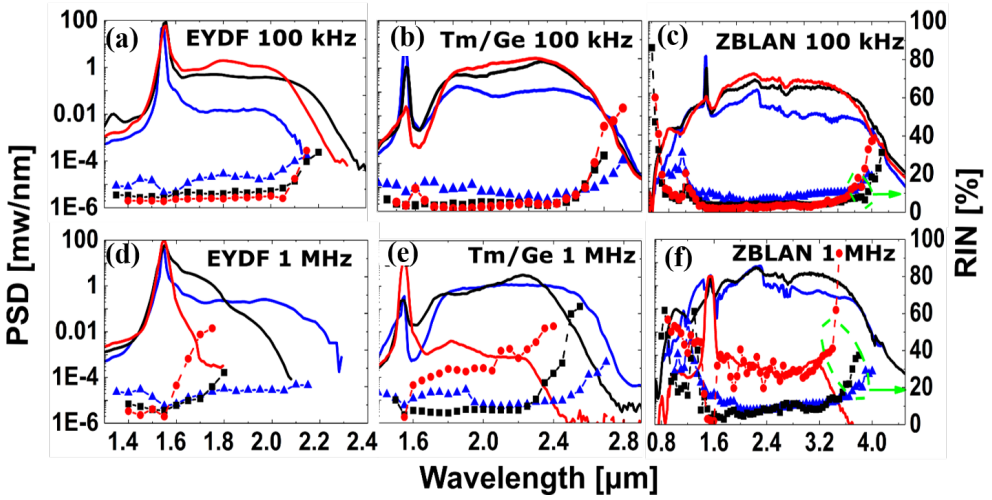


Figure 4.4: Plot of measured PSD (solid line) and RIN profiles (dashed line) of the EYDF stage (a,d), Tm/Ge stage (b,e), and ZBLAN stage (c,f) for repetition rates 100 kHz (top row), and 1 MHz (bottom row).

where γ is nonlinear coefficient of the fiber and for silica = $0.0018(Wm)^{-1}$. When L_{MI} is much more shorter than the length of the fiber in our case 6.3 m of the EYDF then one is assured that MI will initiate SCG. To investigate the effect of the initial pulse parameters on the role of MI and subsequent SCG we plot in 4.5 the computed input peak power to the EYDF. The input peak power was found through the measured average power P_{av} by the relation

$$P_{in} = \frac{P_{av}}{2T_0RR} \quad (4.2)$$

where RR is the repetition rate and the pulse and is assumed to be sec-shaped with a pulse duration that can be computed by the expression

$$T_{FWHM} = 1.763T_0 \quad (4.3)$$

We show in Tab. 4.1, the computed peak power from the measured average power taking into consideration a sech-shaped pulse using eqns. 4.2 and 4.3.

We define two thresholds to investigate the effect of peak power on initiating MI. These thresholds are if $P_{in} < P_1$ then we are sure that MI will not initiate SCG, on the other hand if $P_{in} > P_2$ then MI and subsequent SCG will take place. We also define a theoretical upper limit such that $P_{in} = P_2$ defined as the input peak power P_{in} is so high that even without going through the amplification stage, it is able to

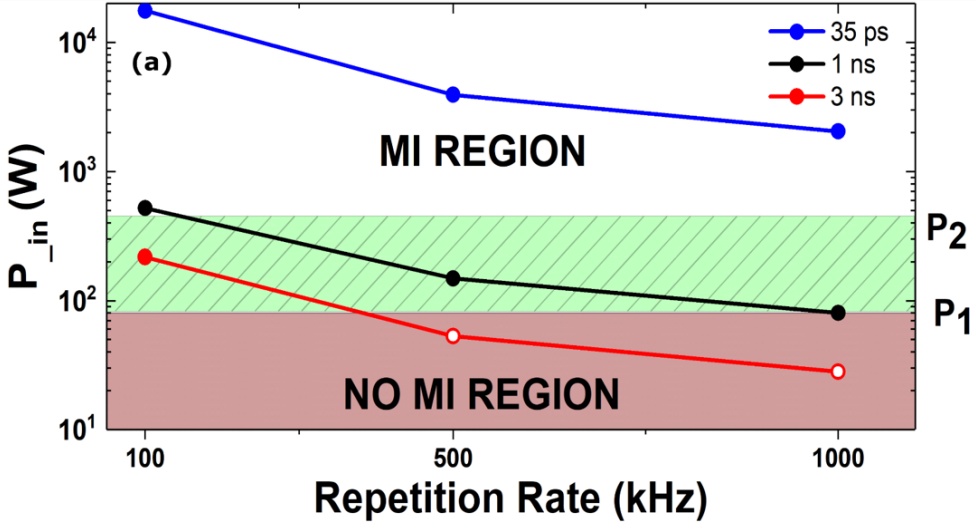


Figure 4.5: Plot of measured input peak power P_{in} to the in-amplifier SC with respect to the repetition rate for a seed with pulse lengths 35 ps (blue), 1 ns (black), 3 ns (red), which has been divided into theoretically assumed regions which predict whether MI will occur ($P_{in} > P_2$, white) and cannot occur ($P_{in} < P_1$, brown) and region of uncertainty (green, see text for $P_{1,2}$). Filled/empty dots mean the measured EYDF output spectrum was broad/narrow.

Table 4.1: Peak power of the pre-amplified seed pulses, calculated from the measured average power.

Rep. Rate (kHz)	35 ps	1 ns	3 ns
100	17630	520	217
500	3929	148	53
1000	2040	80	28

initiate MI on its own. This Mi length can therefore be defined as

$$\frac{1}{\gamma P_2} \text{ is } \frac{L}{5} \quad (4.4)$$

which corresponds to

$$P_2 = \frac{5}{\gamma L} = 441 \text{ W}. \quad (4.5)$$

We define the maximum power out of the EYDF by considering a uniform gain

along the length of the fiber by the expression

$$P_{max} = P_{in}exp(gL). \quad (4.6)$$

where g is the gain of the fiber. We find $g = 0.5m^{-1}$ experimentally by using a long pulse duration of about 20 ns and a fast repetition rate of 3 MHz. With such pulse combination the pulse shape is preserved such that we are not in the region of MI. The lower boundary $P_{in} = P_1$ we define as the maximum power available at the input of the EYDF which will initiate MI given by the relation

$$\frac{1}{\gamma P_1 exp(gL)} \text{ is above } \frac{L}{20} \quad (4.7)$$

which corresponds to

$$P_1 = \frac{20}{\gamma L} \times exp(-gL) = 76W. \quad (4.8)$$

From Fig 4.5, it is clear that MI will occur for all the possible combinations of the 35 ps seed as well as the 1 ns seed with repetition rate 100 kHz as they are above the computed theoretical limit P_2 . Between P_1 and P_2 is the region of uncertainty where we have combinations like 1 ns (500, 1000 kHz), and 3 ns (100 kHz) lying within this region. It can though be found from the experimental plots that there was a strong broadening for these cases that lie within the uncertainty region as depicted in Fig. 4.4. We can also see from Fig. 4.5 that the seed combination 3 ns (500, 1000 kHz) lie well below the theoretical computed lower limit P_1 which is also in agreement with limited spectral broadening depicted in Fig. 4.4 (d-f). We see a low degree of broadening in the EYDF for cases where there is no MI breakup and as such there is no in-amplifier SC. In the event of the occurrence of MI, the longer seed pulses tend to have a lower degree of RIN compared to shorter pulses as can be seen from Fig. 4.4 (a-f).

We measured the RIN at all stages of the cascade employing the same technique described in the previous chapter and also employed in the work done in my Ph.D. studies [10]. A monochromator was used to spectrally filter the broad spectrum at each stage to about 5-25 nm bandwidth FWHM depending on the wavelength and the grating used. Two photodiodes for 1000-5800 nm wavelength region (PDAV10 HgCdTe Amplified detector, Thorlabs, Bandwidth = 100 MHz) and 800-1700 nm wavelength region (Model 1811, New Focus, Bandwidth = 125 MHz) were used to measure the filtered signals. The bandwidth of the photodetectors were each more than twice the repetition rate of the laser source measured to satisfy the Nyquist criteria. Using a fast oscilloscope (HDO9404, 4 GHz, Teledyne Lecroy) with a 40 GS/s sampling rate, the electrical signals from the photodiode were measured. The noise floor of the photodiode on the oscilloscope defined the minimum U_{min} of the signal while the maximum U_{max} was recorded. About 5000 pulses were recorded and the RIN was computed from the pulses by the relation

$$RIN = \frac{\delta U}{\langle U \rangle} \quad (4.9)$$

where δU is the standard deviation of the maximum of the train of pulses and $\langle U \rangle$ is the mean value of

$$U = U_{max} - U_{min} \quad (4.10)$$

The RIN were recorded at every 50 nm step size. We have shown an overlay plot of the PSD and RIN curves in Figs. 4.4 (a-f) and the subsequent plots in this chapter.

4.1.4 In-amplifier Supercontinuum generation in silica fibers

To have a deeper understanding of the SCG dynamics with changing pulse parameters, we now focus on the 500 kHz which exhibit all scenarios as to whether MI will occur or not. We show in Fig. 4.6 the overlay plot of the PSD and RIN at the EYDF output of

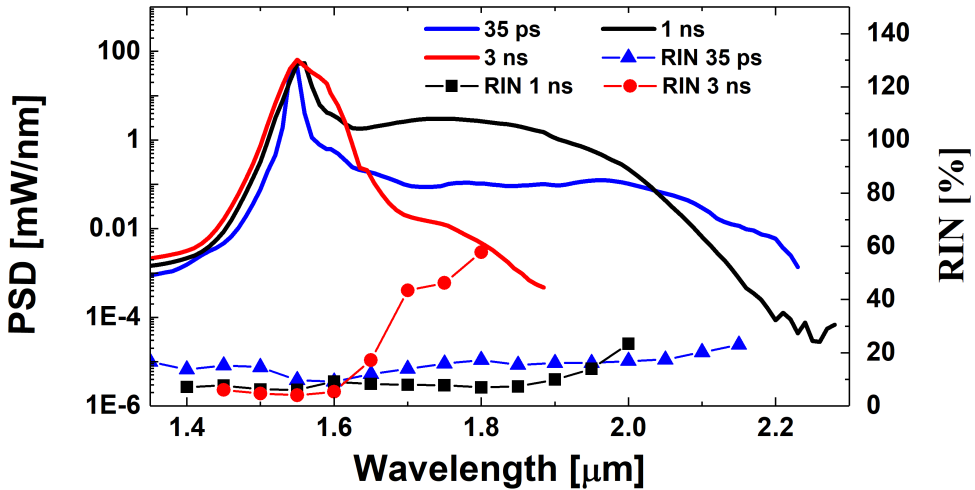


Figure 4.6: Overlay plot of PSD and RIN out of EYDF stage at a repetition rate of 500 kHz and pulse duration 35 ps (blue), 1 ns (black), and 3 ns (red). All RIN were measured at a 50 nm step size, filtering the spectrum to about 5 -25 nm using band-pass filters (grating).

the 3 pulse duration, 35 ps, 1 ns, and 3 ns. As already predicted in the previous section experimentally, the 35 ps and 1 ns cases do show significant broadening whereas that of 3 ns is limited because its peak power is not sufficient to satisfy the condition of MI defined earlier. At 500 kHz most of the power thus remains closer to the pump wavelength. It is imperative to note that the final bandwidth and average power achievable is much dependent on the PSD that falls within the Tm/Ge gain (absorption/emission) window here defined to be 1500 - 2000 nm. It should also be noted that while there are sufficient photons that fall within the Tm/Ge absorption region, there should be well enough photons to stimulate the emission. There should

also be sufficient solitons which overlap with the emission window so that they can be amplified. Though the 35 ps case has the broadest bandwidth as can be seen from Fig. 4.6, the 1 ns case provides both a broad bandwidth and higher PSD that can be absorbed to provide amplification within the Tm/Ge absorption/emission window.

4.1.5 Supercontinuum generation in Thulium doped and Thulium/Germanium co-doped fibers

From Fig. 4.7, we show the overlay plot of the PSD and RIN from a 40 cm long of the Tm/Ge co-doped fiber. Though we only use a short piece of this fiber, we observe that in the case of the 1 ns seed the fiber is almost able to absorb all the residual 1550 nm pump but there remains a strong residual pump for the 35 ps and 3 ns seed. The strong residual pump in the 35 ps case can be attributed to the high peak power achieved with the seed combination. The 3 ns case on the other hand is a result of most of the pulse energy remaining closer to the pump w and that there is not enough stimulated emission. By comparing the RIN curves in Figs. 4.6 and 4.7, it is evident that the Tm/Ge fiber does not only extend the bandwidth of the spectrum but also extend the low noise region. Long pumped SCG has soliton dynamics as the dominant factor, therefore the interaction of the numerous solitons and the number of solitons generated is really important in defining the noise properties. It is well established that the sharp increase in the noise at the red edge of the spectrum can be attributed to the occurrence of rogue events [34, 114] which is observed in all RIN data for all possible pulse combinations used in the experiment [114].

The 3 ns case has the lowest RIN near the pump out of the EYDF stage but increases sharply to about 50 % about 100 nm away from the pump. Similarly, the 1 ns and 35 ps scenario also exhibit low noise levels less than 10 % and 20 % for most of their spectrum about 500 nm and 600 nm bandwidths respectively. At the second stage of the cascade (Tm/Ge stage) the RIN is further reduced and to a larger bandwidth of 1200 nm for the 35 ps and 800 nm for the 1 ns scenario. In the case of the 3 ns seed, it has a RIN of more than 20 % for wavelengths above 1800 nm which can be attributed to the limited PSD within the Tm/Ge gain window. When we make a general comparison of the noise levels not considering the spectral edges which we already know are non-deterministic because of the occurrence of rogue events, we can see that longer pulses tend to have lower RIN so long as they satisfy the condition for MI break-up.

To explain this we further look into the MI theory. From the MI theory 3.7, the frequency of the maximum MI gain gives a rough estimate of the pulse length of the generated solitons given by the expression

$$\frac{\pi}{\Omega_m} \quad (4.11)$$

whereas the input peak power determines the length within the fiber where the solitons are generated.

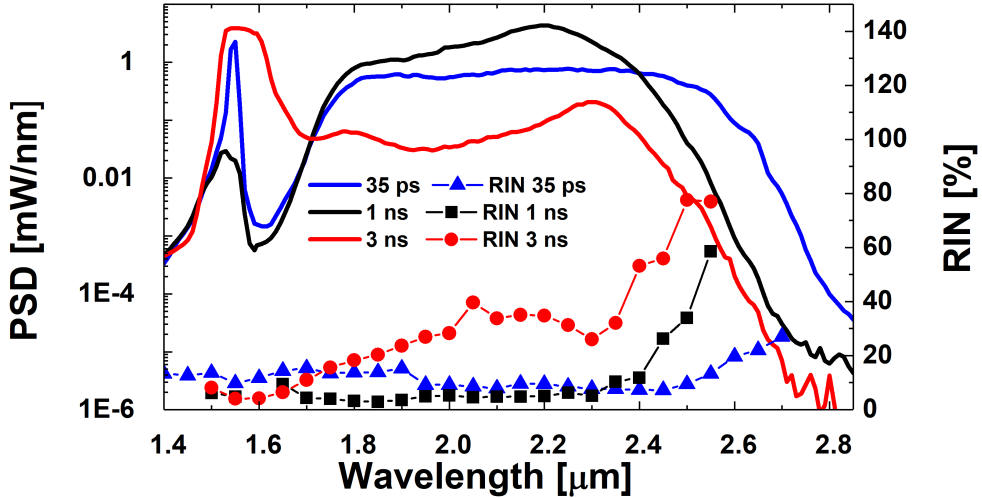


Figure 4.7: Overlay plot of PSD and RIN out of Tm/Ge stage at a repetition rate of 500 kHz and pulse duration 35 ps (blue), 1 ns (black) and 3 ns (red). All RIN were measured at a 50 nm step size filtering the spectrum to about 5 -25 nm using band-pass filters (grating).

For a plane wave, the solitons would be generated at the same point and would be identical. But for a pulse that assumes a Gaussian-like shape, will generate different solitons of different pulse lengths and will be generated at different lengths within the fiber. The high peak power component which is at the center of the pulse will generate short solitons and this happens early in the fiber while the low peak power components will generate relatively long solitons later in the fiber. For relatively shorter pulses the spectrum of the MI-generated solitons will be more distributed leading to phase-dependent and high amplitude soliton collisions. This will lead to a high noise level of the SCG. If one decides to change the pulse duration for a fixed soliton number, this feature will be observed. Thus, if the peak power is kept constant, increasing the pulse duration will increase the soliton number which will lead to a soliton spectrum that is not well distributed and has much more solitons. This will lead to the effect of soliton averaging therefore leading to the comparatively low noise achieved for longer pulses [10, 36]. Solitons that are generated undergo SSFS which are group-velocity to dispersive waves in the blue region as these solitons shed part of their energy to these dispersive waves. This makes the edges of the spectra in ZBLAN much noisy as can be seen in Fig. 4.8. ZBLAN fiber which is a passive fiber helps in the continued SSFS process. Therefore, the noise properties that are achieved in the first and second stages of the cascade are further transferred to the ZBLAN fiber as can be seen in Fig. 4.8. Both the 35 ps and 1 ns seeds have RIN < 10 % noise

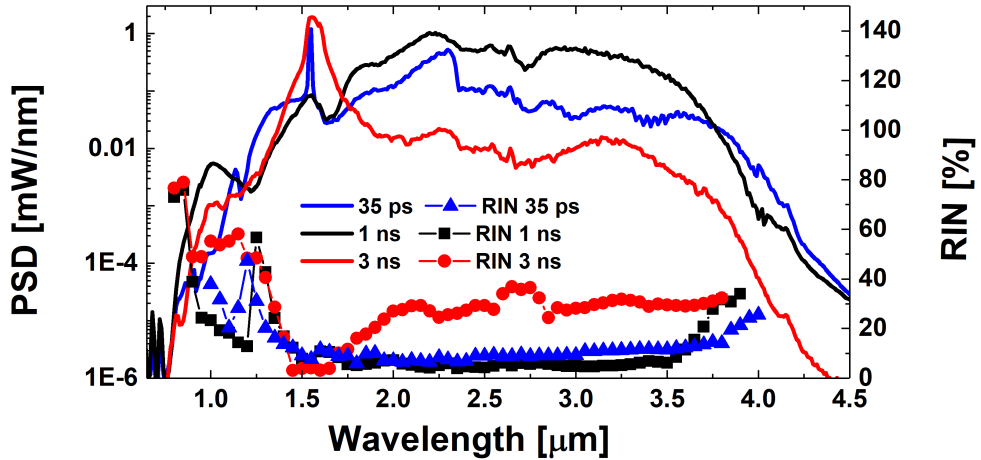


Figure 4.8: Overlay plot of PSD and RIN out of ZBLAN stage at a repetition rate of 500 kHz and pulse duration 35 ps (blue), 1 ns (black) and 3 ns (red). All RIN were measured at a 50 nm step size filtering the spectrum to about 5 -25 nm using band-pass filters (grating).

from 1800 - 3500 nm part of the spectrum. The achieved maximum power efficiencies between the Tm/Ge and ZBLAN fibers considering the output of the ZBLAN fiber are 33.1 % for the 35 ps seed at 1 MHz, 35.2 % for the 1 ns seed at 500 kHz, and 28.9 % for the 3 ns seed at 100 kHz. Relatively, the 1 ns seed outperforms the 35 ps seed in terms of RIN for wavelengths between 1700 - 3600 nm. For the 3 ns scenario, we achieve an average power of 225 mW and a bandwidth of 2250 nm, and a RIN above 20 % in almost all parts of the spectrum with exception of wavelength components closer to the pump. This is because we do not satisfy the condition for MI breakup in the first part of the cascade.

We further show that relatively long pulses will give a better RIN spectrum so long as they can satisfy the condition for MI break-up. This we have explained as the effect of soliton averaging. With these investigations, one could always aim for relatively longer pulses for mid-IR SCG and also consider critically the effect of in-amplifier SCG on the rest of the cascade.

4.2 Summary

Mid-IR SC sources are now being used for several applications and that better criterion in defining the performance of such sources should not only be limited to the bandwidth of the SC generated. Besides, a much more detailed explanation of how

the various pulse parameters combination affect the generated spectrum should also be looked at. In this chapter, we have provided detailed experimental investigations into how the input pulse parameters like the repetition rate and pulse duration affect the bandwidth, RIN, and the average power of the generated spectrum. We show how a possible combination of these parameters will efficiently generate the SC in terms of RIN, bandwidth, and average power by employing the cascading scheme. We show how the in-amplifier PSD generated in the first part of the cascade also affects the subsequent SC of the cascade. We also use an in-house Tm/Ge fiber with a relative higher absorbance compared to a commercial Tm-doped fiber to absorb the residual pump. The absorption of the in-house fiber is shifted 80 nm towards the pump due to the inclusion of germanium ion and can deplete almost all the residual pumps especially for the 1 ns 500 kHz pulse combination.

CHAPTER 5

High repetition rate, stable, Supercontinuum Spectrum up to $10 \mu\text{m}$

This chapter is based on publication that has been submitted and currently under review.

5.0.1 Introduction.

The long-wavelength region that stretches into the mid-infrared (MIR) ($2 - 20 \mu\text{m}$) has received enormous attention because it has seen applications such as real-time monitoring of pollution [141, 142], food quality control [142, 143], stand-off detection of chemicals [144], cancer diagnosis in the early stages [145], hyper-spectral imaging [2, 146] and non-destructive testing of materials that are highly scattering in nature such as coatings, paper ceramics and plastics [133] just to mention a few. Realizing a spatially coherent, high power, compact, with the brightness that is even several orders of magnitude higher than the synchrotron is normally achieved with mid-IR fibers [1, 13, 144]. MIR light source will be the ideal source for the applications aforementioned [51] because it is easy to integrate into setups because they require less optics. The full spectrum of such a source should be contained in the individual pulses that are emitted.

MIR SCG involves relatively long pulses pumping above the ZDW of the fiber to generate solitons through noise seeded MI for the solitons to undergo SSFS. Thus, the solitons should be above the ZDW of all fibers if the cascading technique is employed for continuous SSFS [13, 24, 112]. However, above 5500 nm where the loss edge of fluoride fibers is already reached, one requires chalcogenide fibers to further extend the spectrum. The main challenges here is that the ZDW of such fibers is typically

above 5000 nm [18] in one part and their inability to handle high power because of their low damage threshold on the other part [147].

Several experimental designs of pumping chalcogenide fibers have been adopted to move the solitons above the 5500 nm region. For example, a brute force approach was adopted by directly injecting femtosecond pulses (100-170 fs) with megawatt peak power operating in the MIR region above 4500 nm into a high NA chalcogenide fiber. The configuration of the mid-IR laser source may be based on Ti: Sapphire laser pumping a tunable optical parametric amplifier (OPA) based on the difference frequency nonlinear generation (DFG) concept [1, 148, 149]. With this approach the authors were able to reach wavelengths up to 16000 nm. Since the repetition rate was limited to the kHz regime (1 kHz) the total output average power from the broadband generated spectrum was in the micro-Watt level making such a source not useful for any application. Besides, the pump lasers were bulky coupled with the free space optics which makes it much more complicated and can only be used in a laboratory setup and also much more expensive. In other experiments, a high repetition rate 21 MHz OPA which was tunable from 3300 - 4700 nm with pulse duration of 330 fs giving out kW peak power has been used to generate an SC with 5 mW average power but the spectrum was limited to 10000 nm [23, 150, 151]. This system was also expensive and bulky and can only be used in the laboratory setting.

The best approach to realize a MIR source is by using a fiber laser operating in the MIR region to pump the chalcogenide fiber directly. This has already been realized where MIR laser source whose configuration is based on the rare-earth dopants $\text{Ho}^{3+}/\text{Pr}^{3+}$ co-doped with ZBLAN as host and emitting pulses with duration 230 fs at a wavelength of 2900 nm was used to directly pump a chalcogenide fiber [107]. The chalcogenide fiber was tapered and SCG was able to reach 9500 nm with about 30 mW average power [107]. The configuration has so many bulk and free space optics also losing its compactness. Besides, very small tapered chalcogenide fibers were used because of the short wavelength 2900 nm pump making it not useful for field applications.

Cascading scheme is a promising technique to realize a compact, relatively high power, cheap, MIR source. This involves using the output of a nonlinear fiber as a seed for the other fibers that follow in the cascade to further spectrally broaden. This technique is cheap because it relies on readily available telecommunication 1550 nm laser pumps and amplifiers. This technique was first demonstrated using a two-stage cascade between silica and ZBLAN by using pulses with a duration of 900 fs [152] and subsequently 2 ns [25] to reach 4500 nm which was later extended to a four-stage cascade by using two chalcogenide fibers [13, 18, 112, 153] to get past 10000 nm [13, 153].

The current state of the art is based on an 800 kHz repetition rate delivering 1 ns pulses and has an on-time average power of 139 mW and the bandwidth stretches from 1570 - 11000 nm [13]. This high average power was achieved through a dedicated thulium amplifier that was employed in between the silica and ZBLAN fibers in the laser configuration adding to the complexity and cost of the laser source. The thulium amplifier reduced the signal below 1900 nm including the residual 1550 nm pump quite

significantly and increased the signal above 1900 nm. As discussed in the previous chapter, this is important because it reduces the damage threshold of the soft and fragile chalcogenide fibers in the cascade and most importantly enhanced spectral broadening in the longer wavelengths. It is important also to note the use of Arsenic trisulfide (As_2S_3) chalcogenide fiber which has a better higher damage threshold but lower transmittance compared to the more fragile Arsenic triselenide (As_2Se_3) with a transmittance above 10000 nm was a clever way to manage the damage threshold.

The use of readily available telecommunication components make the cascading technique cheaper to realize compared to other configurations. That notwithstanding, the price is still above what can be integrated into commercial setups as a light source as can be likened to the globalar in spectroscopy. Besides, complexity and robustness are still major issues that need to be addressed. A way of reducing the price was employed in the work by Venck et. al by using only an Erbium amplifier as pump and with this configuration, they could achieve a spectra that reached 10000 nm but the average power was only limited to 16 mW and operated at a low repetition rate of 100 kHz [153].

In this work, we show that one can use a thulium fiber passively without building a dedicated amplifier. The passive thulium fiber redistributes the shorter wavelength light components to longer wavelengths above 2000 nm. This is non-trivial and requires carefully optimizing the fiber length, doping concentration, the pulse duration of the seed, the lengths of other fibers in the cascade, and the NA which inevitably affects the coupling efficiencies between the fibers. With this, we were able generate an SC that span 1500 - 10460 nm with about 86.6 mW average power operating at a repetition rate of 3 MHz without using a dedicated thulium amplifier. Owing to the noise-driven mechanism leading to the generation of the MIR SC, the high repetition rate makes it possible to average several pulses. This makes it ideal for applications like OCT and spectroscopy to enhance the signal to noise ratio. We further show that the source has long term stability in terms of the average power and bandwidth.

5.0.2 Laser Configuration.

At the booster stage, nonlinear effects coupled with amplification dynamics lead to the generation of in-amplifier SC which extends the spectrum out of the amplifier to 2300 nm as can be seen from Fig. 5.2 The laser configuration is shown in Fig. 5.1 The seed is a directly modulated laser diode operating at a wavelength of 1560 nm. the seed has a variable pulse duration of 0.5 - 50 ns and a variable repetition rate of 10 kHz - 3 MHz respectively. The seed is pre-amplified in two amplification stages using a series of Er fibers pumped by 980 nm CW diode. This is followed by EYDFA fiber pumped by two 20 W 915 nm CW diodes referred to as the booster stage. The Er amplifier was operated at a short pulse length of 0.5 ns and the highest repetition rate of 3 MHz. At these seed combination, the seed exhibit a power conversion efficiency of 33 %.

To absorb wavelengths below 2000 nm and redistribute them longer wavelengths

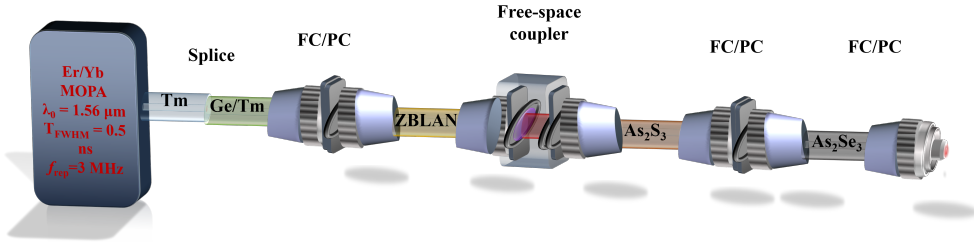


Figure 5.1: Configuration for the MIR SC based on the cascading scheme. The SC is based on a directly modulated laser diode with a pulse duration of 0.5 ns and a repetition rate of 3 MHz. The seed is amplified using the MOPA configuration using a series of Er and ERYDF fibers. The output of the EYDF is spliced to Tm fiber and also spliced to a Tm/Ge codoped fiber. An FC/PC and mating sleeve connector are used between the Tm/Ge output and ZBLAN and ZBLAN - As_2S_3 . There is a fiber collimation/coupling system between ZBLAN - As_2S_3 to remove light below 2000 nm. The fiber is connectorized at the output to make it user friendly.

to extend broadening, a 30 cm long TDF (DCF-TM-10/128, Coreactive) was spliced to the output of the MOPA. The fiber has a core and cladding diameter of $10\mu\text{m}$ and $128\mu\text{m}$ respectively. This fiber is subsequently able to extend the red-edge of the spectrum to about 2670 nm as is evident in Fig 5.2.

To further absorb the residual pump power around 1560 nm and redistribute to longer wavelengths, the output of the TDF is spliced to a Tm/Ge co-doped fiber. The fiber was designed and fabricated from the Nanyang Technological University (NTU). The fiber has similar properties to the one used in the previous chapter. It has an absorption of 50 dB/m around the pump wavelength of 1560 nm. We show in Fig. 5.2 the measured ground state absorption of Tm/Ge co-doped fiber around the pump and also the output spectra of the TDF and Tm/Ge co-doped fiber. It is evident from Fig. 5.2 that the addition of the Tm/Ge co-doped fiber leads to depletion of the residual pump around (1560 nm) and further extending the spectrum to about 3000 nm.

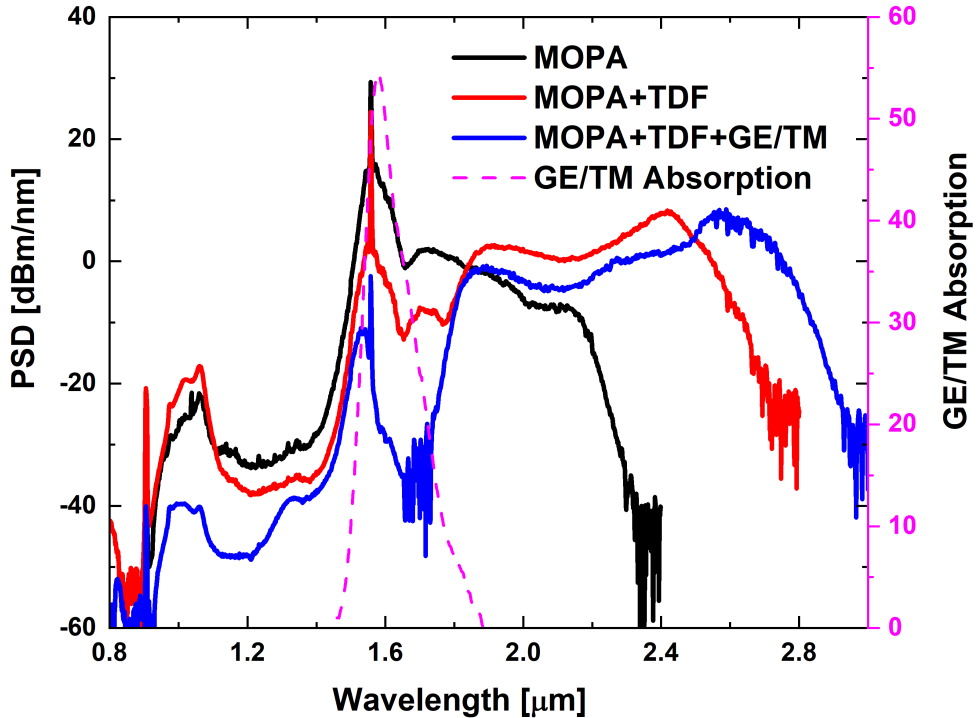


Figure 5.2: Plot of the output spectrum of in amplifier SC from the MOPA (black), 30 cm long of the TDF (red), 25 cm long Tm/Ge (blue) and ground-state absorption spectrum of TDF (pink).

5.0.3 Experimental Results.

One would have expected the TDF to have depleted the residual pump but since its absorption is relatively low, the TM/Ge co-doped fiber does this well. The high concentration of Ge (20 wt %) leads to a reduction of the multi-phonon losses at the red edge of the spectrum and thus, the extension of the spectra to 3000 nm [154]. The reduced long wavelength loss and efficient redistribution process lead to a 92 % total average power above 2000 nm. This increased power at longer wavelengths is important for cascaded SC generation. It is imperative to note that singling out the TDF fiber or Tm/Ge co-doped fiber in SCG wouldn't have yielded such enormous power above 2000 nm. This is clearly shown in Fig. 5.3. From the Fig., we compare the output spectra of 100 cm long TDF to that of 100 cm Tm/Ge co-doped fiber and a combined 30 cm TDF and 25 cm Tm/Ge which is pumped by the MOPA having the in-amplifier SC as the seed. It is evident that the 100cm Tm/Ge co-doped

fiber could completely deplete the residual pump around 1560 nm, the spectrum was limited in broadening compared to the combined TDF and Tm/Ge co-doped going up to around 2700 nm. This is as a result of the relatively larger core diameter of the Tm/Ge codoped fiber which leads to a reduction of the nonlinear effects in one part and also pumping below its ZDW in another part. Similarly, the spectrum out of the TDF alone is not as broad as TDF and Tm/Ge co-doped combined. This is due to the high multi-phonon losses above 2400 nm which is characteristic of silica fibers [149]. Besides, due to the low absorption of the fiber around the pump wavelength, it is evident from Fig. 5.3 that most of the residual pump is still preserved.

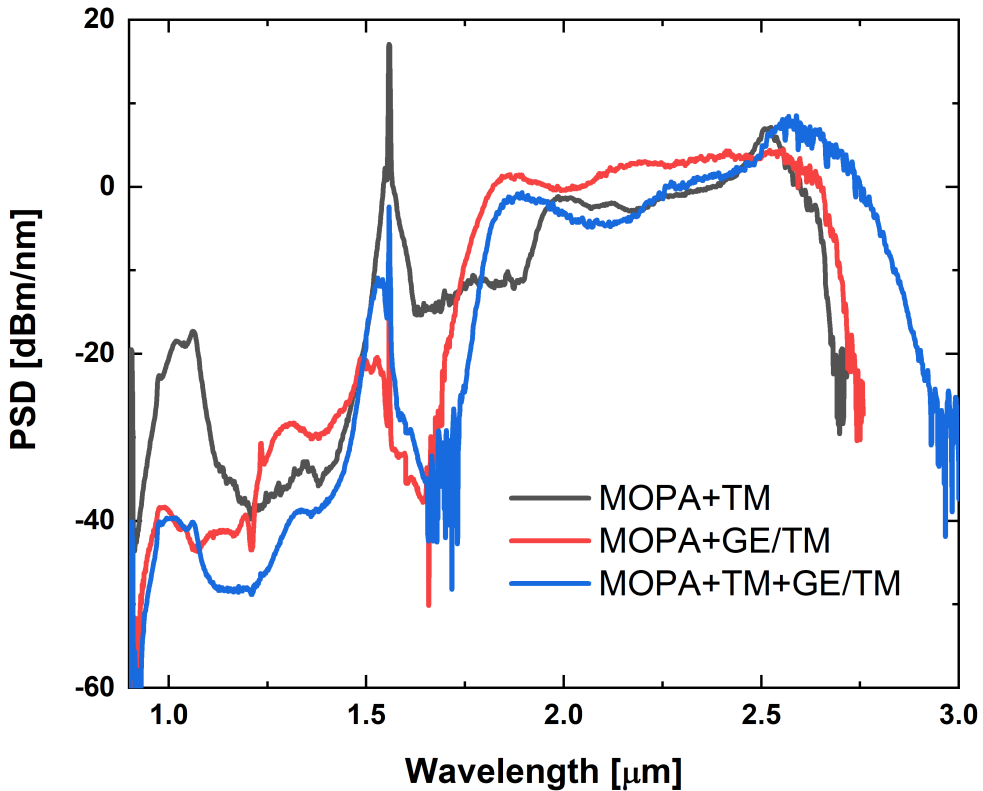


Figure 5.3: Comparison of the spectra using a 100 cm long TDF (black), 100 cm Tm/Ge co-doped fiber (red) and 30 cm of the TDF and 25 cm of the Tm/Ge combined pumped with the in-amplifier SC.

The high discrepancies in material properties of silica and nonlinear fluoride fibers make splicing of these fibers almost impossible. An attempt has been made to splice silica and ZBLAN which yielded lower splice losses, the repeatability of this has

been in doubt [30]. This is because one needs an optimized recipe for the splice parameters. Since the heating system (filament or arc heater) in the splicer does degrade with time, such recipes are not sustainable and thus, need to be changed per the changing conditions of the heating system. To efficiently couple light between the nonlinear fibers one, therefore, needs to resort to mechanical means of joining the fibers together. In our case, we connectorized the fibers with FC/PC connectors and subsequently joined together by a mating sleeve. This yielded robust, stable, and good coupling efficiencies (40-80 %) depending on the eccentricities of the fibers.

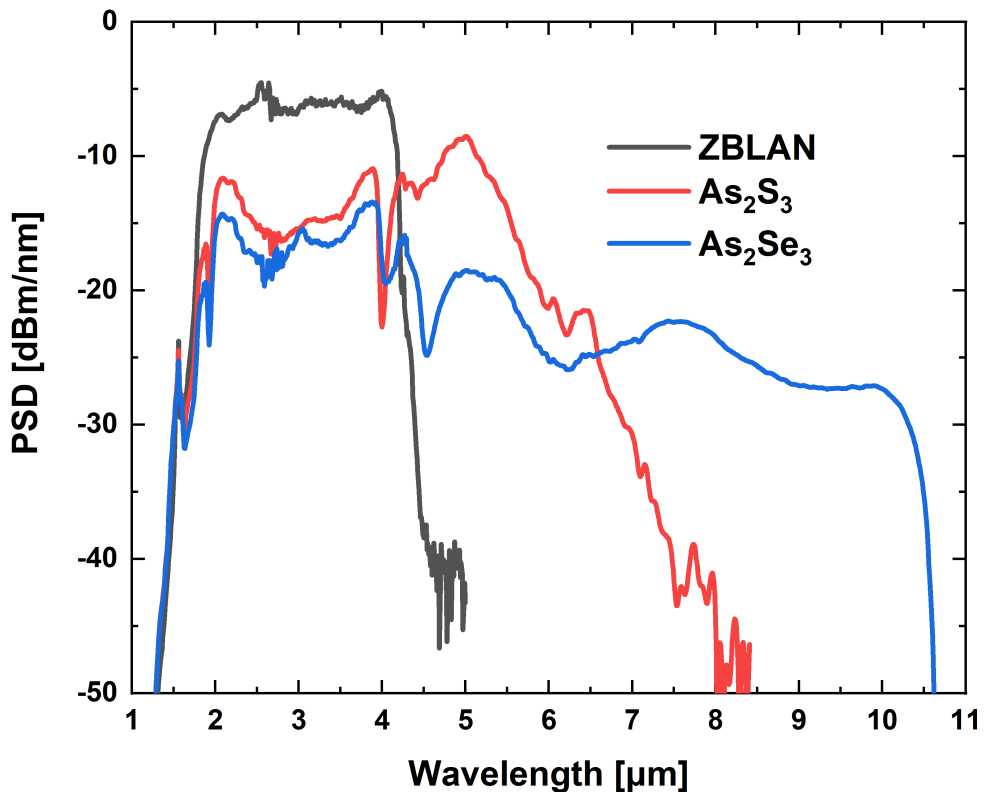


Figure 5.4: Plot of measured spectra out ZBLAN (black), As_2S_3 (red) and As_2Se_3 (blue) fibers. All measurements are normalized to the average power and step size of the instruments used.

The connectorization between the Ge/Tm and a 4.5 m long ZBLAN (Fiberlabs Inc.) fiber with $7\mu\text{m}$ core diameter shifted the red edge of the spectrum to about 4400 nm as can be seen from 5.4. The spectra from ZBLAN became the seed for the chalcogenide fibers. Connectorization was made between ZBLAN and $9\mu\text{m}$, core

diameter As_2S_3 with a 4.5 m length (RF-S-9-IRflex). This subsequently shifted the spectrum to about 7000 nm through SSFS. Besides shifting of the spectrum to longer wavelengths, As_2S_3 was used to reduce the damage threshold to finally get to the soft and fragile As_2Se_3 . Chalcogenide fibers generally have high absorption below

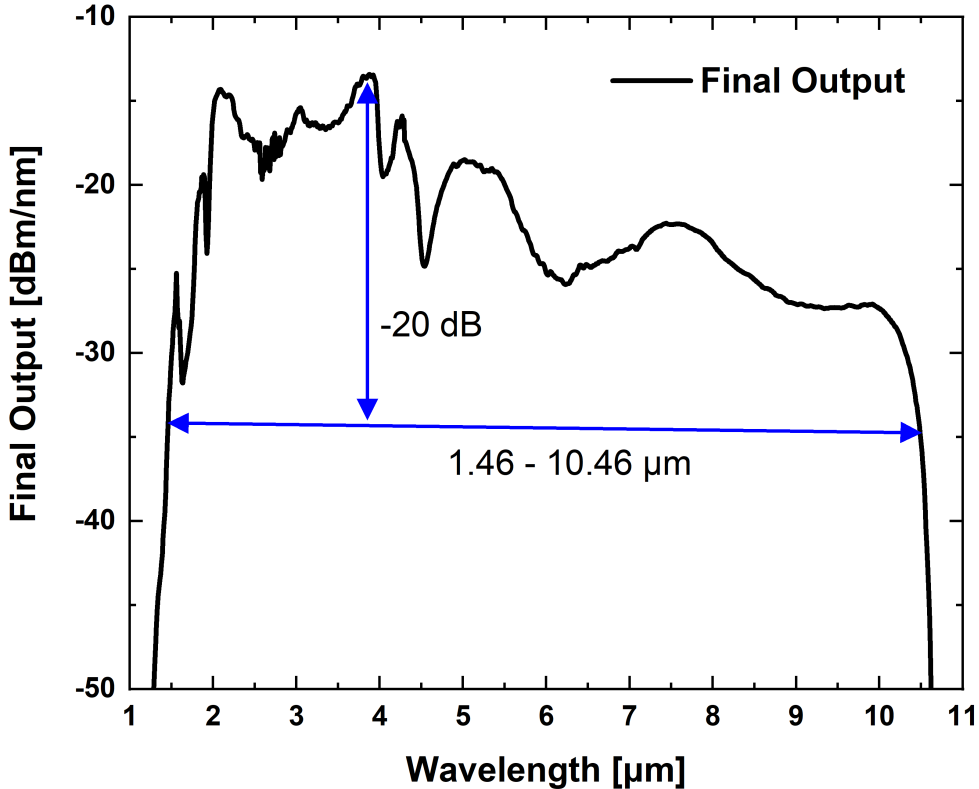


Figure 5.5: MIR SC output spectrum spanning 1460 - 10460 nm taken from the -20 dB edge.

1500 nm. It is therefore important that the As_2S_3 fiber is shielded from these short-wavelength light. A fiber collimation/coupling module (Thorlabs, PAF2-4E) with two black diamond lenses was used to filter out the short-wavelength light, acting as a long pass filter. This removed light below the 1500 nm region reducing the damage that would have been caused to the chalcogenide fibers. The As_2S_3 was then connected to a 12 μm core As_2Se_3 (IRF-SeG-12, IRflex), which is 3 m in length. This extends the spectrum past 10000 nm as can be seen from Fig. 5.4. Due to the high NA of the As_2Se_3 , the output of the fiber was terminated with an FC/PC connected to a 4 mm silver coated off-axis parabolic mirror. This made it convenient and very practical for

use in various applications.

The PSD out of ZBLAN was measured with a grating-based scanning spectrometer (Spectro 320, from Instrument Systems). The spectrometer is fitted with three gratings whose efficiencies and resolution are wavelength dependent. The scanning spectrometer could measure up to 5000 nm. Above this wavelength, a custom-made fiber-coupled Fourier transform infrared (FTIR) spectrometer (FOSS Inc.) was used to measure the PSD. Both spectrometers were already calibrated using a black-body radiation source. All PSD measured were normalized to the average power and step size of the spectrometers.

When a -20 dB is taken as reference, it is clear from 5.5 that the output spectrum span from 1460 nm to 10460 nm. At a fixed pulse duration of 0.5 ns and a repetition rate of 3 MHz and operating the booster CW pump diodes at 2A, the average power achieved in all stages of the cascade are Ge/Tm = 1554 mW, ZBLAN = 825 mW, $As_2S_3 = 172$ mW and $As_2Se_3 = 86.6$ mW. These yield coupling efficiencies of Tm/Ge - ZBLAN = 67 %, ZBLAN - $As_2S_3 = 72$ % and $As_2S_3 - As_2Se_3 = 88$ % respectively. The low coupling efficiency between Ge/Tm and ZBLAN can be attributed to the dramatic change in core diameter from 12.5 μm to 7 μm . The final average power of 86.6 mW was distributed in the spectrum as > 3600 nm = 47.48, > 4500 nm = 27.43 mW and > 7300 nm = 9.2 mW. The coupling efficiencies between all fibers have been computed taking into consideration Fresnel reflections from the interface of a 5 cm long pigtail of the same fiber. It is very impressive to achieve such a



Figure 5.6: A pack of the compact, robust MIR SC with dimensions 47.4cm \times 30.0cm \times 13.45cm.

large bandwidth and a high average power operating at a fast repetition rate without building a dedicated Tm amplifier. The MIR source has been made compact (packed in $47.4\text{cm} \times 30.0\text{cm} \times 13.45\text{cm}$ box shown in 5.6) and robust being able to be carried around. The source has been shipped to Radboud University to carry on with pollution monitoring activities which includes food and environmental degradation.

To achieve these results, the fiber length was carefully optimized to achieve the largest possible bandwidth and average power. It is a trade-off between the average power achievable and spectral broadening. For much shorter fibers within the cascade than the optimal length, the energy transferred to the red edge of the spectrum was reduced and affected subsequent spectral broadening in the subsequent fibers. Likewise, a longer fiber than the optimized length on the other hand reduced the power to the longer wavelengths. This is a result of losses and multi-phonon absorption and has a ripple effect on the total average power in the cascade.

5.0.4 Laser stability measurement.

The continuous average power stability at the output of the MIR SC was measured over 7 days using a power meter. During this period, the source was switched on

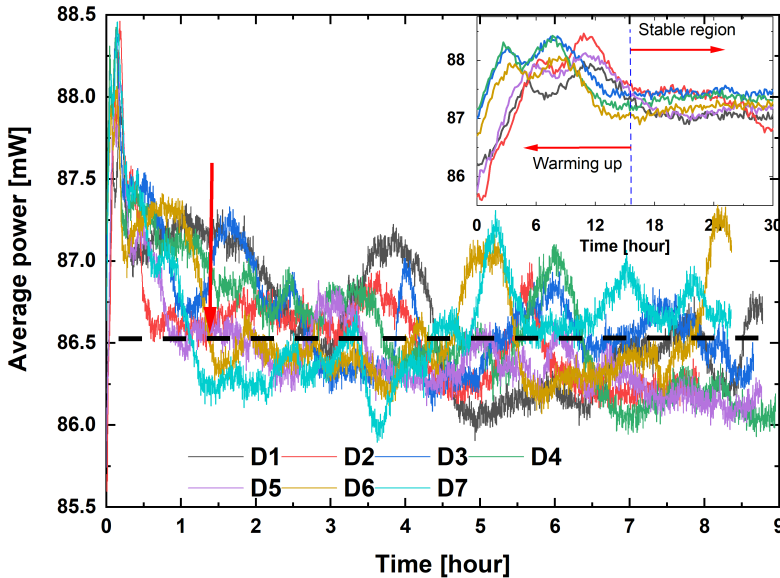


Figure 5.7: Stability measurement of the compact, all-fiber cascaded MIR SC source over 7 days with measurements being taken for 8-9 hours each day. Inset: A more enlarged figure of the first 30 minutes of each day measurement.

and operated for about 8 - 9 hours. Shown in Fig. 5.7 and 5.8 are the plot of the

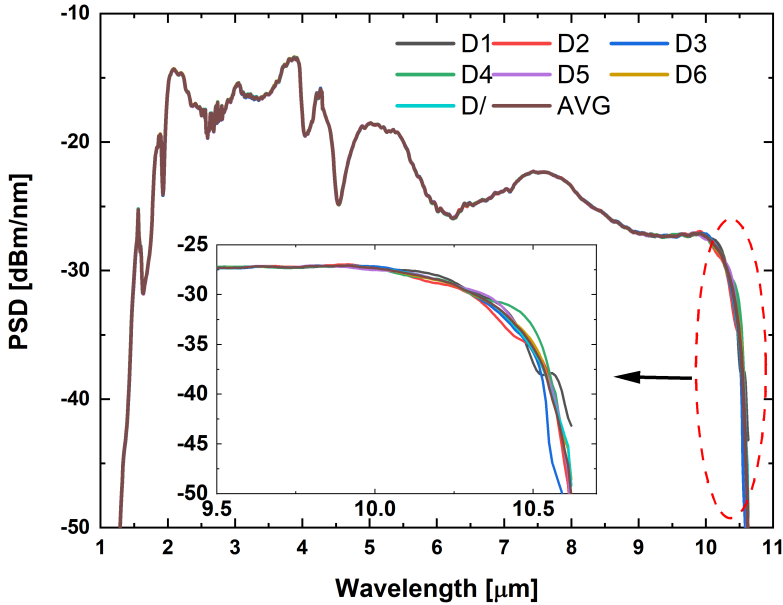


Figure 5.8: Measured 7 PSD spectra to show the spectral stability recorded for about 8-9 hours of operation. An average of these spectra is also plotted as AVG. Inset: A closer look at the spectral stability above 9500 nm.

stability measurements. It is clear from the Figs that the laser is stable in terms of power and most stable in terms of bandwidth except for wavelengths closer to the red edge. From the inset in Fig. 5.7, it is clear that for one to efficiently operate the laser, it will require a little over 15 minutes to warm up and become stable. This warm up period is generally determined by the laser seed. The fluctuations show about 0.43 % standard deviation over the 7 days for a mean value of about 1 mW. After each stability measurement, a spectrum was taken. The spectra shown in Fig. 5.8 show a high degree of overlap between all the spectra at almost all wavelengths.

The slight variation is seen above 10000 nm which is due to the established fact of the occurrence of rogue events at the edges of the spectra [115]. This is also depicted in the inset of Fig. 5.8. For the main spectral range of 1800 nm to 10000 nm, the spectral variations are within ± 0.18 dB. It should be noted that this is the first time a comprehensive power and spectral stability has been measured for a MIR source and has proven to be well within what can be used for various field and industrial applications.

5.0.5 Summary.

In conclusion, we have built a compact, all-fiber, stable, relatively high power, MIR SC operating at a fast repetition rate of 3 MHz and a pulse duration of 0.5 ns. The total achieved bandwidth of the MIR source span 1460 - 10460 nm with an on-time average power of 86.6 mW. The laser configuration is based on an EYDFA pumping a series of concatenated Tm, Tm/Ge, ZBLAN, As_2S_3 and As_2Se_3 fibers. The MIR spectra are based on solitons generated in the first part of the cascade (in-amplifier supercontinuum generated in the EYDFA) which continue to red-shift through SSFS. The Tm/Ge and Tm act as passive fibers without any dedicated amplifier with CW pumps. They only redistribute energy from shorter to longer wavelengths through absorption/emission processes. Though a record 139 mW average power has been achieved in the work by [13], the low repetition rate reduces the averaging effect that would cancel the fluctuations in the laser. Besides, since we don't use a dedicated Tm amplifier, the thermal load is reduced and also the components for building the laser and complexity reduces making our laser relatively cheaper.

CHAPTER 6

Application of Supercontinuum Sources in Spectroscopy

6.1 Introduction

NIR and MIR spectroscopy has been in existence since the 1970s and has been used in the quantitative analysis of food products like a dairy, pharmaceutical products like medicine, and the chemical industry [155]. The light source used in these spectrometers is the quartz-tungsten-halogen lamps and remains the most acceptable light source for spectroscopic applications till date [156, 157]. It has a broad coverage from the visible to the mid-infrared range. These light sources are relatively cheap to manufacture compared to emerging technologies but spatially incoherent (emits to all directions) and also have a lower PSD across all wavelengths. The SC source has thus, emerged as an alternative to mitigate the challenges of spatial coherence and low PSD. In other words, the SC can be described to have the broad spectral range of a lamp coupled with the collimated beam that characterizes a laser. This means during optical instrumentation, since the beam exits from a fiber, one can easily manipulate the beam (tightly focusing it into a sample being probed) leading to achieving high spectral brightness compared to the traditional light sources [51]. When stand-off detection probes are being made, the SC source becomes an ideal light source because it can travel far distances before losing its spatial coherence through divergence and interaction with particles [144]. Similarly, when a small portion of a bulky sample is to be analyzed, the SC has an enormous advantage over the traditional light sources.

SCG involves intricate nonlinear processes coupled with absorption/emission dynamics of an intense narrow linewidth laser traversing an optical fiber [1, 4, 25]. The optical fiber has the nonlinear properties enhanced through a reduction in the core

size or through structures like holes around the core as well as the addition of dopants for amplification or reduction in the multi-phonon absorption [14, 24, 154]. SCG in the MIR region is based on noise-seeded modulation instability leading to the generation of solitons. The solitons continue to redshift through collisions with other solitons and shedding off energy between them. This generally makes MIR sources suffer from a high RIN from pulse to pulse. A way to mitigate this is through the inherent building configuration of the source or by scaling the repetition rate to average over several pulses [10, 36].

The high discrepancy in absorption between the NIR and MIR makes it difficult to probe a sample simultaneously using a single configuration. While the NIR has low absorbance and would require longer interaction lengths (in the centimeter range) the opposite holds for the MIR range (micron range.) The higher O-H absorption around 2900 nm (3448 /cm), the fundamental absorption of water, makes it difficult to probe the overlapping C-H stretches. Most experimental setups seem to avoid this region with rich information. Direct absorption pathlength cuvettes with cm length have been used in the NIR to enhance the interaction length [157, 158]. To do same in the MIR, one would have to use cuvettes with lengths down to a few microns [159]. At this short pathlength, samples to be probed would have sizes to the order of the pathlength and cannot be contained in these cuvettes. Besides, it is difficult to fill highly viscous liquids in such a small pathlength cuvette and we may end up damaging the windows of the containing cell.

To mitigate the problems listed above for the MIR, a novel attenuated total internal reflection (ATR) has been used to probe samples in the MIR [160]. The ATR has been used to probe samples since the 1960s [160–162] and has evolved with applications that span soil characterization, polymer studies, food quality control, and drug quality control [163]. ATR relies on the interaction of MIR light with the sample via the evanescent field through total internal reflection. The depth of penetration describes the optical pathlength of the evanescent field and the number of bounces to the crystal-sample surface per penetration depth defines the effective pathlength of the light. For low PSD traditional halogen lamps, a multi-bounce ATR leads to a low throughput leading to reduced SNR. Thus, SC sources with higher PSD makes it ideal for designing a multi-bounce ATR setup which enhances the weak interaction of the sample and light.

Whereas measured raw spectra contain information for analysis, requisite statistical and mathematical models need to be developed to make predictions out of the measured data. Chemometrics, is the branch of Chemistry that uses Mathematical tools to make raw data relevant for the extraction of useful information. It is extremely useful for analyzing and exploring large data sets that have lots of variables with complex inter-relations which are poorly understood [43]. The main idea of chemometrics is a reduction of dimensionality of the data set to differentiate real data from noise and redundant information while retaining the essential information [43]. One can describe patterns and relations between variables and make predictions and calibration models to this effect.

In this chapter, we present a supercontinuum based spectroscopic approach to

measure the absorption of protein and alcohol in water solution. We incorporate an ATR module to measure the high absorption region of the fundamental O-H stretches of water to utilize the low penetration depth of the evanescent field. We show the common problems that are encountered in ATR configuration especially in the high absorption region of water and low wavelength region. In the shorter wavelength, we use a variable pathlength cuvette cell to measure direct absorption of the same sample keeping all other measurement parameters constant. We analyze the proof of concept measurement by using principal component analysis and visualize the change in analyte concentrations both in the NIR and MIR.

6.2 Measurement Instrumentation

The schematic of the spectroscopic setup used in measuring the absorption spectrum is shown in 6.1. It comprises of an in-house built MIR SC source which is collimated with an off-axis parabolic mirror to approximately a beam diameter of 4mm^2 . The beam is then directed first onto the ATR module interface using two CaF_2 coated lenses. The ATR module is equipped with four silver-coated off-axis parabolic mirrors with two at the input and two at the output. It uses ZnSe crystal as the high refractive index material which is sandwiched between two metallic plates with a small opening between the crystal and the metallic plate. The small opening acts as the sample holder as schematically shown in 6.2.

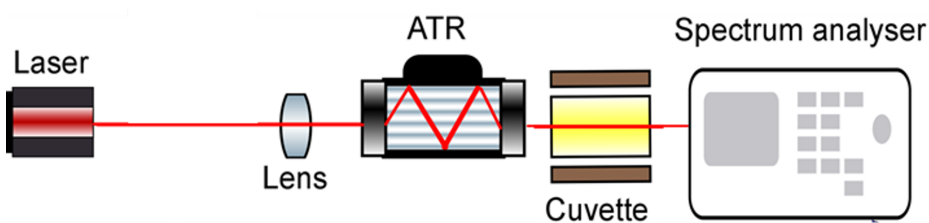


Figure 6.1: Basic instrumentation of the spectroscopic setup employing a supercontinuum as light source, variable pathlength cuvette (6 micron - 1mm cells) and ATR module as sample holders and an optical spectrum analyzer connected to a computer for measuring the absorption spectrum.

The configuration of the ATR module is such that the initially collimated light beam is focused on the input of the high index ZnSe interface. After exiting the output of the crystal, the light diverges which is then collimated with the other two off-axis parabolic mirrors. The ATR module is from Specac Inc. UK (GS11001) with a solid sample holder fitted with a trapezium shape 52 mm long, 20 mm wide, and 2mm thick with 45° angled facets ZnSe crystal. It has 25 bounces with the longer side of the trapezium having 13 bounces and the shorter side having 12 bounces. It

has a variable angle from 30° – 60° which can be altered through a knob located at the back of the sample holder which makes the penetration depth easily adjustable to suit different absorbing materials. The samples can be filled from two openings on top of the metallic material which closely holds the ZnSe crystal. The light from the

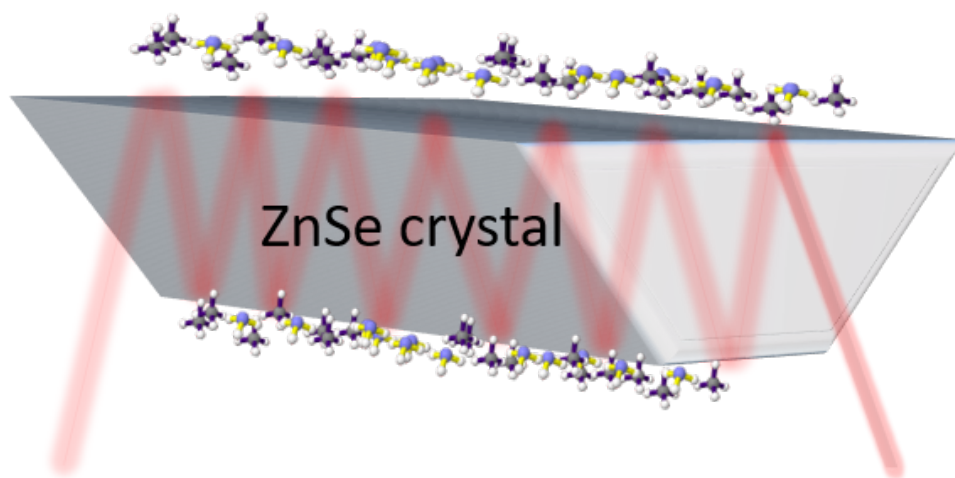


Figure 6.2: Schematic of ZnSe crystal with analytes at both interfaces of the crystal. The MIR light interacts on the crystal-analyte surface through the evanescent field of the light.

ATR module is then directed to a demountable cell with varying pathlength. The cuvette is also from Specac Inc. UK (GS20512). It is demountable and uses Mylar as spacers which can vary the pathlength from as short as 6 microns to as long as 1 mm. The spacers are sandwiched between two CaF_2 windows and held tightly by two metallic plates. One can alter the pathlength by changing the series of Mylar spacers that accompanies the cuvette which can easily be demounted and mounted and tightly screwed together.

The light from the cuvette is directly coupled into a scanning spectrometer from Instrument Systems (Spectro 320): The spectrometer's configuration is based on the asymmetric Czerny-Turner with a $2f$ configuration. It is fitted with four different gratings and three different detectors (silicon, Indium-gallium-arsenide, lead sulfide, and lead selenide). The gratings are mounted on a motorized stage which is controlled by an accompanying software. The gratings have different rulings which also define the resolution of the measured spectra. In general, the resolution decreases as wavelength increases.

6.2.1 Light source

The MIR light source used is an in-house built source which is based on the MOPA configuration described in the previous chapters. A directly modulated seed with low power is amplified in two stages and finally amplified at the booster stage. The amplification dynamics coupled with nonlinearity lead to the generation of a spectrum that spans 1400 nm - 2300 nm. The spectrum is further extended to about 2800 nm using about 30 cm long of a Tm/Ge codoped fiber. Using a ZBLAN as passive the spectrum is further extended to about 4000 nm as can be seen from Fig. 6.3 The

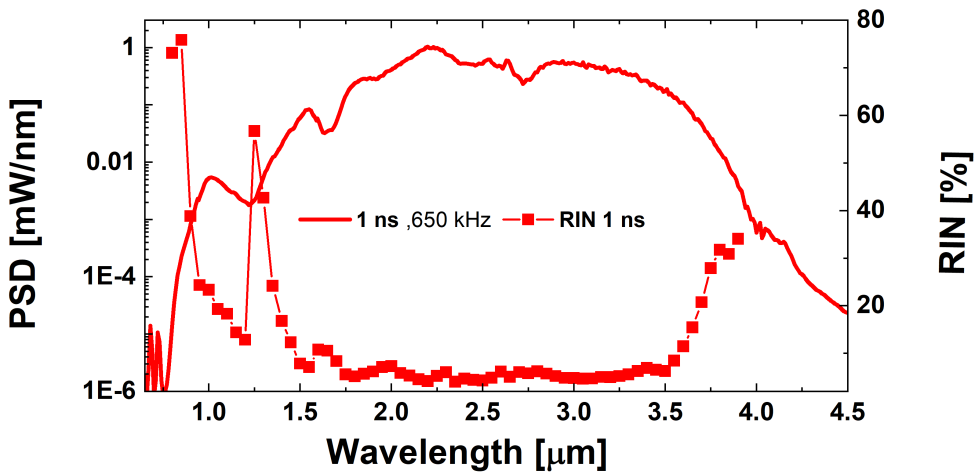


Figure 6.3: Overlay plot of the PSD and RIN curves of the MIR light source used in the experimental setup. The seed operates at a pulse duration of 1 ns, a repetition rate of 600 kHz and has a total average power of 650 mW.

MIR source operates at a repetition rate of 600 kHz and a pulse duration of 1 ns with a total average power of 650 mW. The dynamics leading to the generation of MIR SC sources are initiated by noise therefore most part of the spectrum fluctuates spectrally. The choice of a high repetition rate source and the long integration times of the scanning spectrometer (54 seconds) leads to averaging of the pulses which reduces the SNR. We have measured the RIN for the spectrum by spectrally filtering at every 50 nm step size as can be shown in Fig. 6.3. Our region of interest is around 1300 - 3600 nm. The spectra have a low RIN of less than 15 % within this region with the Tm/Ge absorption region. The spectra exhibit a high power of more than 0.01 mW/nm in the region of interest which compensates for losses posed by the ZnSe crystal and also the high absorption in the 2800 nm region. The MIR light source is unpolarized and as such has all components of the s and p polarized light.

6.2.2 Wavelength and angle dependence on penetration depth

We show in Fig. 6.4 the refractive index profile of water and ZnSe crystal used in the ATR module [164, 165]. It is the square root of the dielectric constant which is complex. The absorption of a medium has a contribution from the imaginary part of the refractive index. The refractive index is really useful in estimating the absorption, penetration depth, and effective pathlength that is achievable with our setup. The high refractive index of ZnSe compared to water (analyte) is also important in achieving total internal reflection between the crystal and the analyte interface. The

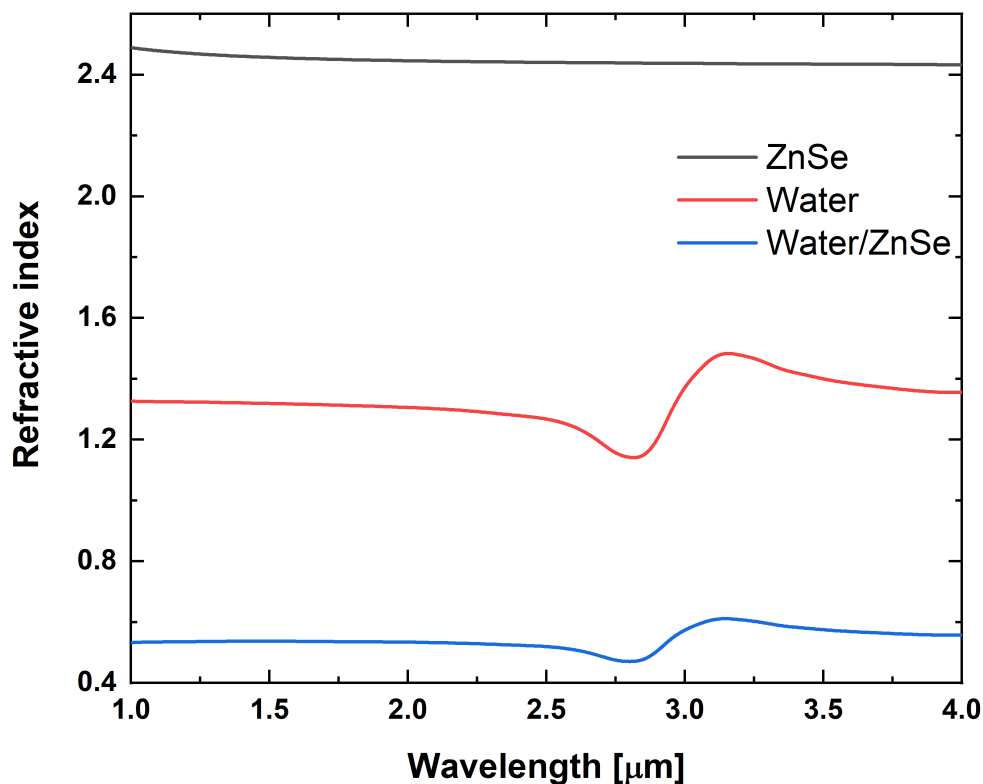


Figure 6.4: Refractive index profile between wavelengths 1000 - 4000 nm for ZnSe (black), water (red) and the ratio of the refractive index of water to ZnSe (blue). The data has been taken from [164, 165].

reflectance of the MIR source from the air- ZnSe crystal interface varies slightly from 4 % to 10 % for both polarization states and increases with increasing angle of incidence. Both polarization states will reflect all the light at the grazing angle. It is imperative to note that in our configuration, we were well below the grazing angle of

90° so we had reflections across the entire wavelength which was within the 4-10 % margin reflectivity. Moreover, the total internal reflection between the ZnSe crystal and the analyte is almost 100 % except for losses posed by absorption of the analyte and the crystal. Though a mirror can have the highest reflectivity and sometimes quoted to enhance this reflectivity, loss of intensity becomes apparent under multiple reflections. On the other hand total, internal reflection is truly total as can be seen in optical fibers where light can travel several kilometers with losses only imposed by the material properties of the fiber.

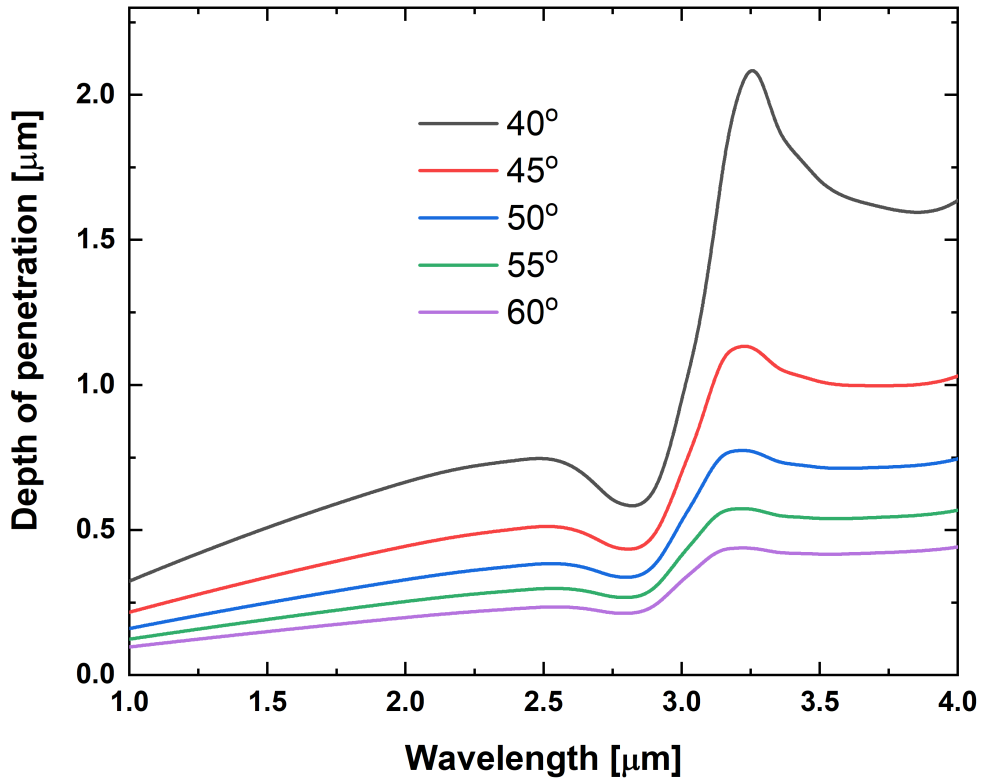


Figure 6.5: Plot of penetration depth variation with wavelength for varying angles of incidence (40, 45, 50, 55, 60°).

The approximate solution for the penetration depth of the evanescent field for the s and p polarized components of light can be derived from Fresnel's equations of reflection as

$$d_s = \frac{\lambda}{n_1} \cdot \frac{n_{21} \cos(\theta)}{\pi(1 - n_{21}^2) \sqrt{\sin^2(\theta) - n_{21}^2}} \quad (6.1)$$

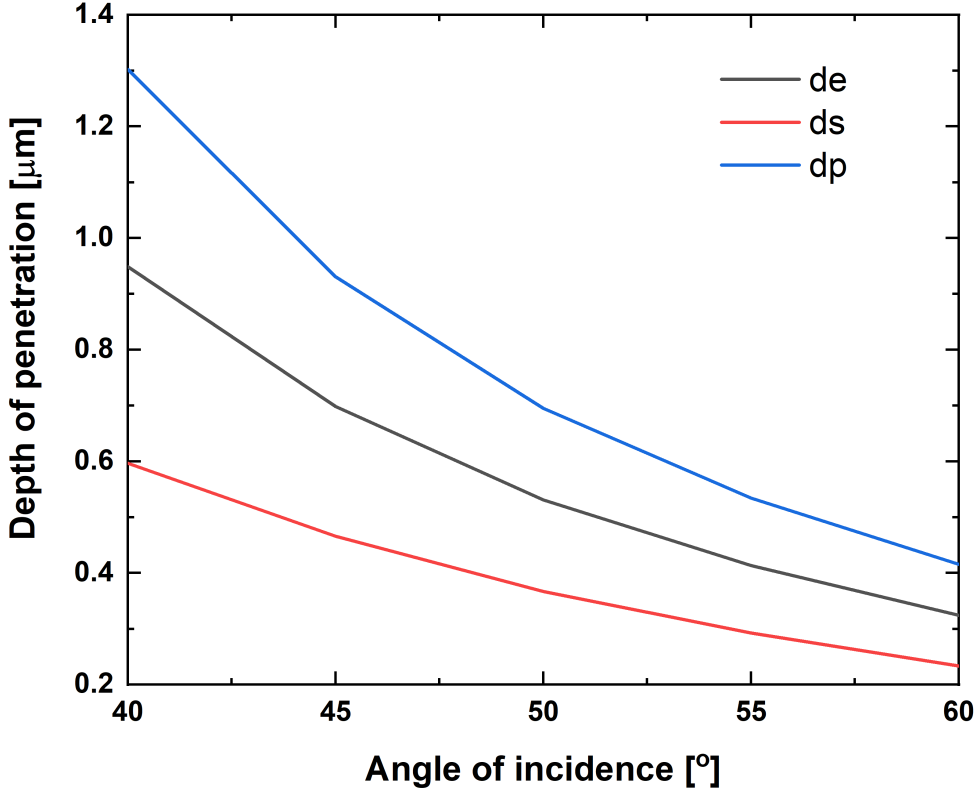


Figure 6.6: Penetration depth variation with respect to the angle of incidence at a fixed wavelength of 2970 nm. At this wavelength, water has its highest peak of the fundamental absorption.

$$d_p = \frac{\lambda}{n_1} \cdot \frac{n_{21} \cos(\theta) [2 \sin^2(\theta) - n_{21}^2]}{\pi(1 - n_{21}^2) [(1 + n_{21}^2) \sin^2(\theta) - n_{21}^2] \sqrt{\sin^2(\theta) - n_{21}^2}} \quad (6.2)$$

For an unpolarized light source like the one used in our setup, the effective penetration depth is then given by

$$d_e = \frac{d_s + d_p}{2} \times N \quad (6.3)$$

where λ is the wavelength of light, θ is the angle of incidence, n_1 is the refractive index of the sample being probed, and n_{21} is the ratio of the refractive indices of the ZnSe crystal and the sample and N is the number of bounces of the ZnSe crystal. Using information of the refractive indices plot in Fig 6.4 and a few selected angles of

incidence, we plot how the penetration depth varies with wavelength and incidence angle. We could see that the penetration depth increases slightly at longer wavelengths and also for the smaller degrees of angle of incidence. With this, we could optimize our setup such that for weak absorption spectra we could choose smaller angles of incidence to enhance the SNR. For highly absorbing analytes which tends to degrade the SNR, we choose larger angles of incidence. The latter was what we encountered in our configuration so we set our angle of incidence of the ATR module to 60° for all MIR measurements. As explained earlier, water is highly absorbing in this region and therefore necessary to set our system at this angle. We show the variation in penetration depth in Fig. 6.5. From Fig. 6.6 we show the variation of penetration depth with the angle of incidence for both the s and p polarized components of the MIR light and the penetration depth of the average of them which depicts an unpolarized light. We see that as one goes to longer angles the penetration depth decreases. As we approach the critical angle, there is an exponential growth of the penetration depth and below this angle the penetration depth is imaginary. One would see infinite penetration depth values from the critical angle and almost getting to zero at the grazing angle of $\theta = 90^\circ$

6.3 Information in the near and mid-IR region

We show in Tab. 6.1 the concentrations of the constituents of the 22 analytes used in the experiment. They consist of either of water, ethanol, sucrose and protein or all or none. The amount used in each of the mixtures were not known before measurements were taken. The samples were prepared at the University of Copenhagen, Department of food Science.

Measurements were taken with the scanning spectrometer with a step size of 0.1 nm and a resolution of 1 nm for the region below 1700 nm, 4 nm for the region between 1700 - 2400 nm, and 10 nm for the region above 2400 nm. The resolution is defined by the grooves on the gratings. In all, 20 averages were taken for a single measurement leading to a total integration time of about 8 minutes. While the ATR module was filled when taking measurements in the MIR, the cuvette was empty. This was intentionally done so that the MIR signal was not degraded by the long pathlength cuvette. For the NIR measurement both the cuvette and ATR module were filled when taking the spectrum. By so doing, we corrected for the penetration length dependence on wavelength. The ATR module had 25 bounces on both sides of the crystal (12 on the shorter side and 13 on the longer side). In order not to degrade the MIR signal, only one side of the ZnSe crystal (side with 12 bounces) was filled during the experiment. Thus, the effective penetration depth at 60° incidence angle at 2970 nm was estimated to be about $4.9\mu\text{m}$ which conforms to pathlengths used by Hale et. al [165] to have measured the absorption of water in this region.

The absorbance was calculated using the Beers law as

$$\log_{10}\left(\frac{I_0}{I_s}\right) \quad (6.4)$$

Table 6.1: Concentration (g/mol) of the various constituents (ethanol, sucrose and protein) of the analytes and their volume of water.

Sample	H_2O	ETOH	SUCC	LPRO
1	4.00000	0.15149	0.00000	0.00000
2	3.00000	0.30298	0.00000	0.00000
3	2.00000	0.45446	0.00000	0.00000
4	1.00000	0.60595	0.00000	0.00000
5	4.00000	0.00000	0.42200	0.00000
6	3.00000	0.00000	0.84400	0.00000
7	2.00000	0.00000	1.26600	0.00000
8	1.00000	0.00000	1.68800	0.00000
9	0.00000	0.50496	0.00000	0.12167
10	1.00000	0.32462	0.00000	0.15643
11	0.00000	0.32462	0.00000	0.18250
12	1.00000	0.00000	0.46889	0.24333
13	1.00000	0.00000	0.30143	0.26071
14	0.00000	0.00000	0.23444	0.32444
15	3.00000	0.07574	0.42200	0.14600
16	2.00000	0.30298	0.21100	0.10950
17	3.00000	0.27543	0.38364	0.06636
18	4.00000	0.15149	0.63300	0.03650
19	0.00000	0.00000	0.00000	0.36500
20	0.00000	0.75744	0.00000	0.00000
21	0.00000	0.00000	2.11000	0.00000
23	5.00000	0.00000	0.00000	0.00000

where I_0 is the intensity of light when there is no sample in the sample holders and I_s is when the sample holders are filled. Measurements were taken under controlled temperature and monitored with a thermal camera. The large beam diameter at the sample interface also reduced the effect of local heating of the sample.

The absorption spectra exhibit the fundamental O-H stretching in the 2970 nm region and its first overtone in the 1450 nm region. A combination of this band and other bands is seen in the 1950 nm region. Besides these, there are C-H stretches in the 3400 nm and 2300 nm regions.

6.4 Multivariate modeling of IR data

All spectra in both the NIR and MIR were preprocessed using a second derivative Savtizky-Golay two-degree polynomial with a window size of 15. After preprocessing of the data, they were mean-centered before all other analyses were carried out. A PCA analysis was performed to see the common trends in the data and also to see

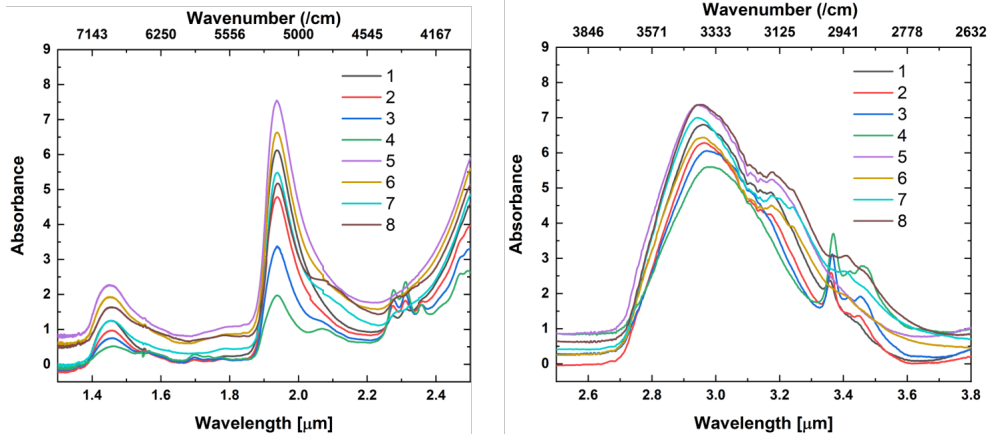


Figure 6.7: NIR and MIR spectra of the first 8 samples taken with a demountable liquid cell cuvette and the ATR module.

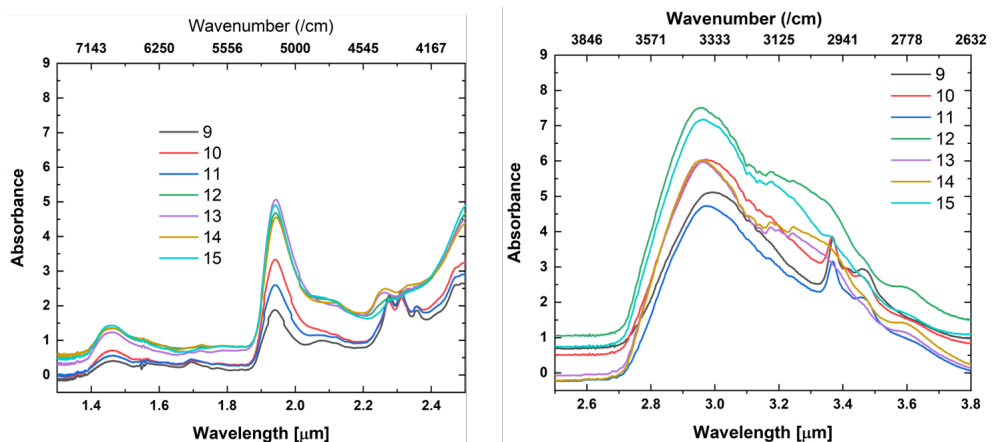


Figure 6.8: NIR and MIR spectra of the next 7 samples taken with a demountable liquid cell cuvette and the ATR module.

possible outliers. To determine the number of significant principal components that best explain the data, a scree test was performed. This is shown in Figs. 6.10. It can be seen from the Figs. that, up to the third principal component, the data is about 98.9 % explained for the NIR and about 97.9 % explained for the MIR

For the NIR region, the first principal component explains to about 89.1 % of the

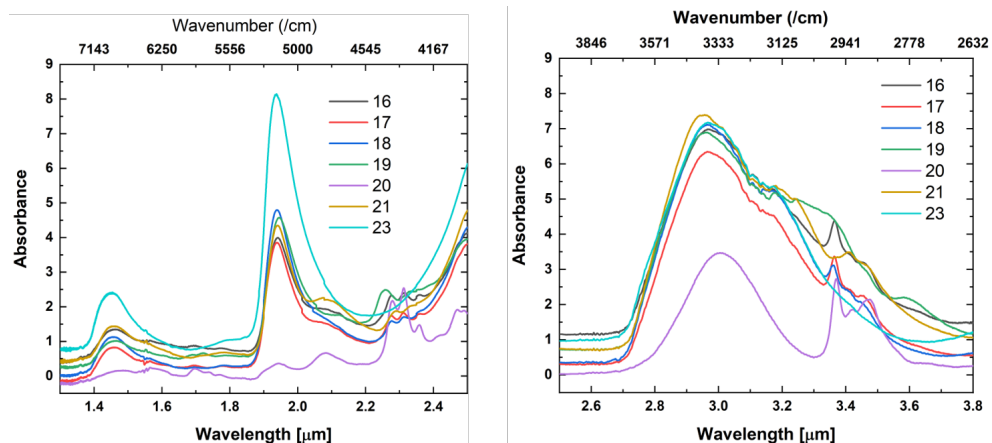


Figure 6.9: NIR and MIR spectra of the last 7 samples taken with a demountable liquid cell cuvette and the ATR module.

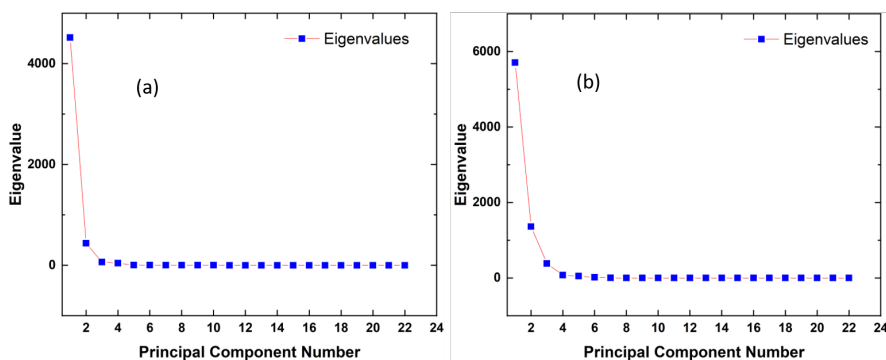


Figure 6.10: Scree plot of the Eigenvalues to the principal component number for both (a) NIR and (b) MIR.

data and the second principal component explains about 8.6 % whereas the third principal component only explains 1.3 % of the data. The situation is a little bit different from the MIR which has 74.9 % explanation from the first principal component, 17.9 % from the second principal component, and 5.1 % from the third principal component. This is explicitly shown in the loadings and scores plot in Figs. 6.11 and 6.12. It is clear from Fig. 6.12 that the samples with only ethanol (black dots) show the most uniform variation both in the NIR and MIR score plot compared to the other samples. Generally, there exists some overlap among the samples in the variance structure while there is a minimal separation of the center of gravity of the analytes.

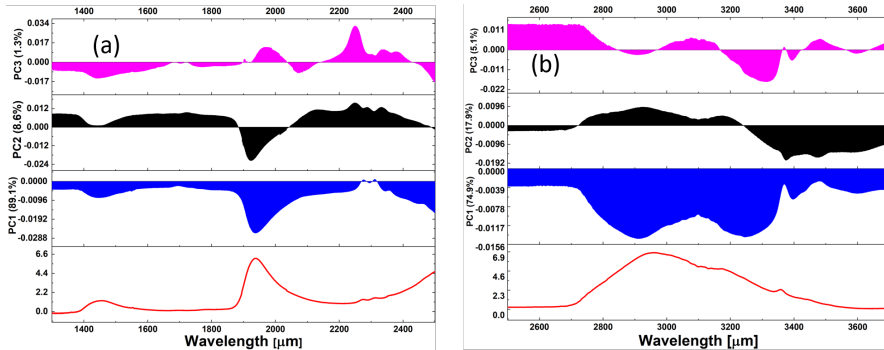


Figure 6.11: Loading plot of the NIR and MIR spectrum with the reference spectrum.

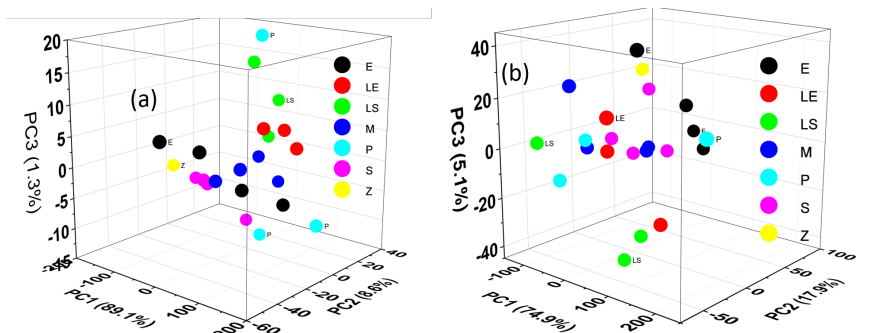


Figure 6.12: Score plot of the different mixtures categorized into 7 different sets for (a) NIR and (b) MIR. The data was pre-processed with Savitzky-Golay two-degree polynomial and mean-centered before mean centering. From 6.1 Samples 1-4 are labelled (E), 5-8 are labelled (S), 9-11 labelled (LE), 12-14 labelled (LS), 15-18 labelled (M), 19-21 labelled (P) and 23 labelled (Z).

No sample was found to be extreme within its group in both the NIR and MIR so no outlier was visualized.

Whiles, we acknowledge that the sample size is small for the numerous groups we have, a proof of concept experiment has been established and we could see variations in their structure. A robust data analysis would be increasing the sample size and correlating the measurements in the NIR region to that of the MIR region.

6.4.1 Summary

MIR SCG has become useful and is now being used in several applications. The high PSD across several bandwidths and the fact that all this PSD comes from the tip of a fiber make it ideal for configurations that require fewer optical components. But the generation of the SC is quite complicated and requires many nonlinear phenomena coupled with absorption/emission processes. Besides, the current technique in generating a compact, stable, high power SC relies on the cascading technique which involves concatenating several fibers in each case optimizing the various fiber parameters.

In this Chapter, we have incorporated an in-house built SC source with about 650 mW of average power, a repetition rate of 600 kHz, and a pulse duration of 1 ns into a spectroscopic setup. The high repetition rate operation of the laser helps in the mitigation of the inherent RIN associated with the SC generation through pulse averaging. We showed how a directed absorption measurement can then be taken with two different sample holders (a demountable cell and an ATR module). Each of these cells are important for specific regions of interest. While the low absorption in the NIR region require a longer pathlength cell, the MIR region requires a shorter pathlength cell. We thus, make use of the interaction of the evanescent field with samples which effectively sees a minute loss in the signal in this region. The setup is optimized to enhance the signal by considering the effect of the angle of incidence and wavelength on penetration depth. We measure the absorbance spectra of 22 samples which is a mixture of water, ethanol, sucrose, and protein. We perform a PCA analysis in both the NIR and MIR regions to see the variation in the changing concentrations of the mixture. We show that though it is a proof of concept experiment we see variations that are explained by the principal components.

CHAPTER 7

Conclusion and Outlook

MIR SCG requires a complete understanding of the nonlinear phenomena and the absorption/emission dynamics involved in the spectral broadening. While the coupled effects are still being investigated and quite complicated to understand, nevertheless, this novel way of generating spatially coherent broadband MIR light sources has to be looked into in-depth. The Ph.D. project was set out on developing an all-fiber, compact, high power MIR broadband source through the cascading scheme to monitor food adulteration. Initially, we were supposed to use a high power gain switch pump at 1064 nm to pump a series of PCF, Tm, and ZBLAN fibers. Such a source was to operate at a relatively high repetition rate to mitigate the inherent noise in the SC. This turned out a bit difficult to realize and a change of plan was made to use a directly modulated gain switch laser at 1550 nm to pump a series of step-index silica fibers, Tm, and ZBLAN fibers.

Whiles, we acknowledge the noise seeded MI that leads to the generation of the SC, a high repetition rate operation of the laser was anticipated to mitigate the noise through pulse averaging. Besides, an inherent way of reducing the noise through the SC configuration had to be employed. This compact SC source was to be integrated as part of a spectroscopic setup to monitor food adulteration, especially on milk samples. To address the concerns of making a low noise, a compact, an all-fiber source we first looked into the theory and mechanisms that lead to the SC generation. Starting from the basic concepts of optical fibers to the pulse propagation and the linear and nonlinear interactions that occur as a result of the pulse propagation. We also reviewed the absorption/emission processes specifically for the gain fibers used in our SC generation configuration. We also touched on the general theory and assumptions of an important technique for measuring the noise in broadband SC.

After looking through the theory, We first set out to build the SC source in collaboration with NKT Photonics who are part of the broad project SUPUVIR. A compact SC was realized with a tunable repetition rate from a few kHz to the MHz regime. By inherent engineering, we generated a broadband SC out of the third stage amplification known as in-amplifier SC. This technique significantly reduced the RIN of our source through what we term soliton spectral alignment. Since the noise of the cascading scheme and how it was transferred from one fiber to the other was of

importance, we built a noise measurement set-up at DTU and measured the noise at all stages of the MIR source. We found out that the noise was much reduced at the final output through the gain induced soliton spectral alignment when compared to commercial SC source (from NKT Photonics) of similar built. This result was published in the Nature Scientific reports.

Moreover, MIR SCG generation using the cascading scheme had normally been a try and error realization. To streamline the generation, we set out on how to understand various pulse combinations like repetition rate and pulse duration and how they affect the bandwidth, total average power, and the noise of the SC generated. We were able to demonstrate that longer pulses so long as they undergo MI has a better performance in terms of noise compared to relatively shorter pulses. As indicated earlier, one would want the source to operate at the highest repetition rate possible but this invariably reduces the peak power which will not lead to MI. Moreover, the use of a highly absorbing Tm/Ge co-doped fiber which reduced the residual pump so that soft and fragile fibers in the cascade were not damaged was of relevance to MIR SC generation. This demonstration saw a safe operation of our MIR source. This work has been done in collaboration with Nanyang University in Singapore which lead to a journal publication in Optics Letters.

In a similar contribution, we extended the spectrum by adding chalcogenide fibers to the cascade. We also optimized the parameters like fiber length to achieve the largest bandwidth and the highest average power. This has been one of the state-of-the-art source developed without using a dedicated thulium amplifier but only a short piece of Tm and Tm/Ge co-doped fibers which acted as a passive fiber only for redistributive purposes. The source operates at a record 3 MHz repetition rate and helps in pulse averaging to mitigate the noise for real time applications. High stability was achieved making this source viable for several applications. This source development was part of a project FLAIR where I had a contribution to the development. This work has a journal paper that is currently under review with Optics Letters.

A part of the project was to monitor food adulteration in milk. Thus, a spectroscopic setup was made at DTU which used the in-house developed MIR SC as the light source. A novel ATR module that uses the evanescent field of light to interact with the sample was incorporated to the setup to take measurements in the MIR region. Besides, a demountable pathlength cuvette was also incorporated to take measurements in the NIR region. A proof of concept measurements were taken on 22 samples which were obtained from the Copenhagen University (Department of Food Science). PCA visualization was used to see the variances in the spectra per the concentrations of the 22 mixtures. It must be stressed that measurements in both the NIR and MIR were done to develop a robust data analysis through correlation of the fundamental absorption and the recurring overtones. This is an ongoing project and hopefully, we can make a publication out of it.

It is imperative to note that scaling up the repetition rate, the bandwidth, and total average power are challenges that should be looked at in the future. The current state-of-the-art which has a dedicated thulium amplifier has an average power of 139mW and a bandwidth up to 11000 nm. There is more room for improvement in

these cases. Besides, making the source very small and compact to fit into commercial spectroscopic setups should also be delved into. Moreover, the nonlinear and amplification dynamics should be critically looked into. MIR SC generation is a promising field and needs a critical examination of the field.

A.1 Statistical Distribution of the RIN and Pulse repetition frequency

The statistical distribution for spectrally filtered spectra (10-12 nm FWHM) at the pump wavelength of 1064 nm and the red edge of 1800 nm of a PCF based SC source from NKT Photonics.

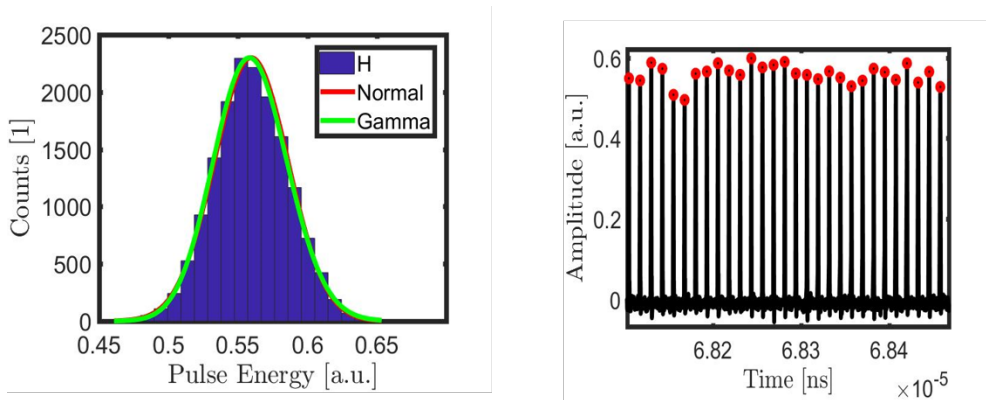


Figure A.1: Histograms of the pulse energy and the corresponding normal (red curve), Gaussian (blue curve), and gamma (green) distribution curves at the pump wavelength. The pulse repetition frequency indicating the pulse variation. At the pump wavelength there is the gradual increase of the FWHM and as such low values of RIN.

This way of computing the RIN can serve as an alternative to the difference between the maximum and minimum of each pulse and subsequent statistics on the train of pulses which has been adopted in this work.

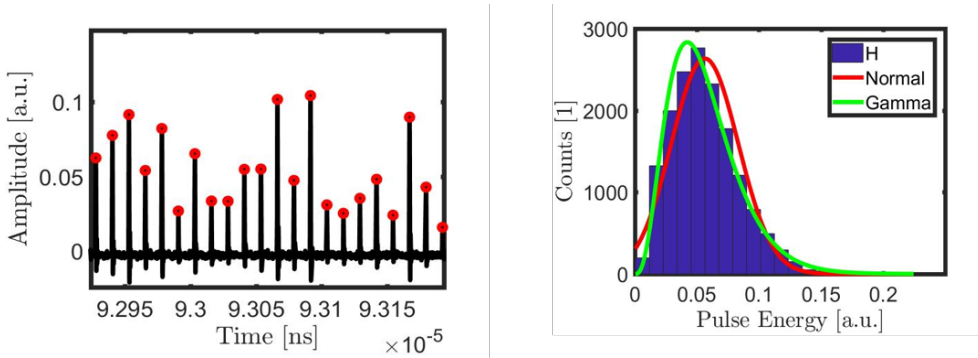


Figure A.2: The pulse repetition frequency indicating the pulse variation. Histograms of the pulse energy and the corresponding normal (red curve), Gaussian (blue curve), and gamma (green) distribution curves at the red edge of the spectrum. At the red edge there is a skewed distribution and as such high values of RIN..

A.2 Experimental setup for RIN measurement

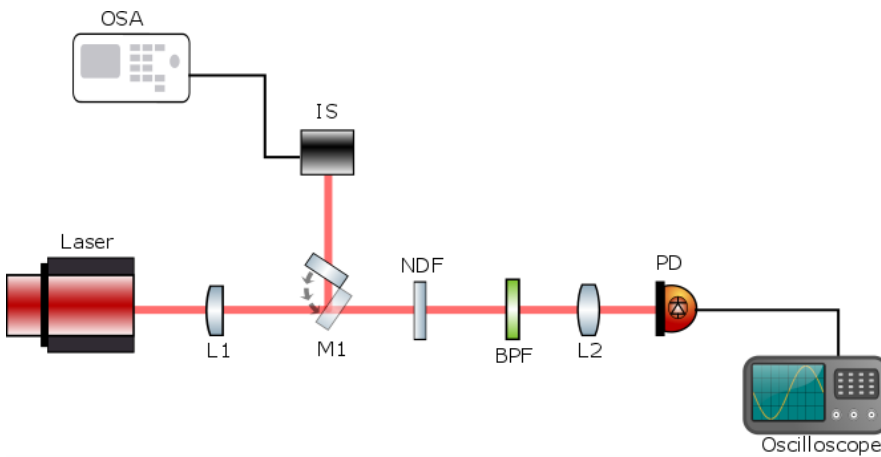


Figure A.3: Experimental setup for RIN measurement which has the light source and a set of interchangeable bandpass filters with FWHM 10-20 nm, a photodiode and a fast oscilloscope..

The experimental setup for the RIN measurement is shown. This configuration is different from the previous one since it uses commercially available interchangeable

bandpass filters from 400- 2350 nm. The filters have a bandpass between 10 - 20 nm FWHM depending on the wavelength of operation. All other components remain the same as in the previous setup except for the light source.

A.3 Splice loss optimization.

Careful optimization of splice parameters leads to low splice loss. For dissimilar fibers, this can be hard to achieve. Such parameters include hot push, hot push delay, on-time duration, pre-gap, and filament power. We show here for two silica fibers the parameters used and the splice loss achieved.

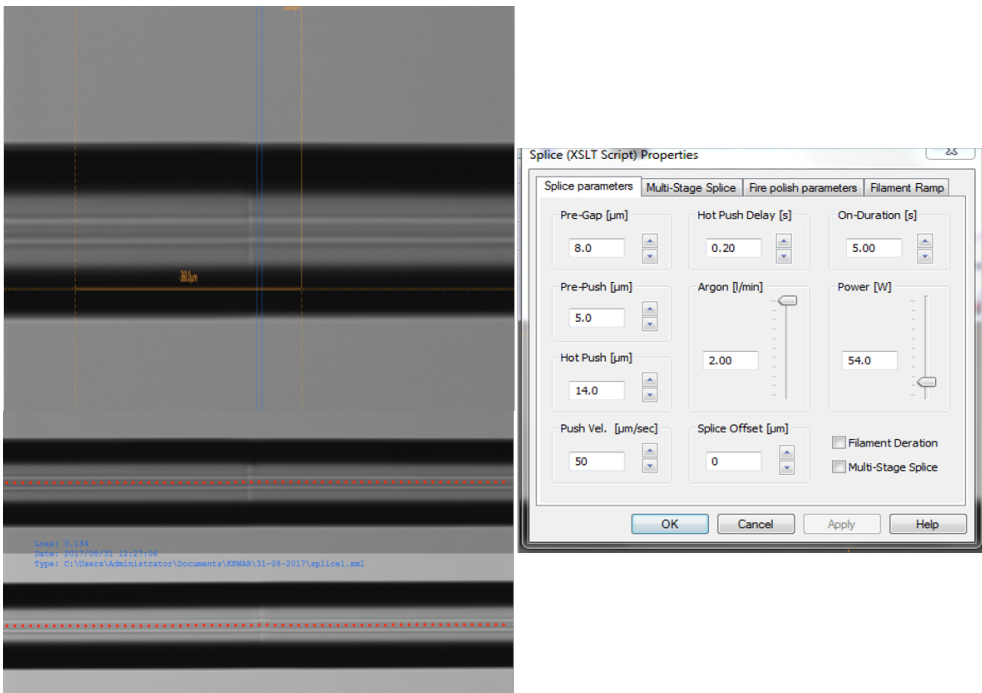


Figure A.4: Splice achieved between two silica fibers and the optimization of the splice parameters..

A.4 Direct absorption measurement of water using relatively long pathlength cuvettes.

Before settling on an ATR module we used a direct absorption measurement cell to optimize the absorption of water in the NIR and MIR region. While a $12\mu\text{m}$ cell pathlength cell still degraded the signal in the 2970 nm region, the first overtone and combination tones in 1450 and 1950 could not be revealed. On the other hand, a $50\mu\text{m}$ cell pathlength cell though revealed the recurring overtones the fundamental region signal was degraded.

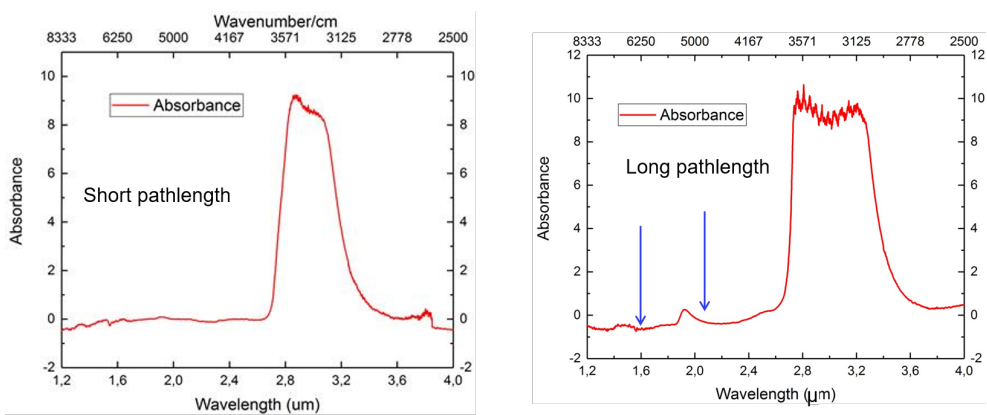


Figure A.5: NIR and MIR spectra of the last 7 samples taken with a demountable liquid cell cuvette and the ATR module..

A.5 Absorption measurement of different kinds of alcohol.

Using our spectroscopic setup we measure the O-H and C-H stretches of these alcohol. These measurements were taken with an ATR module with 12 bounces.

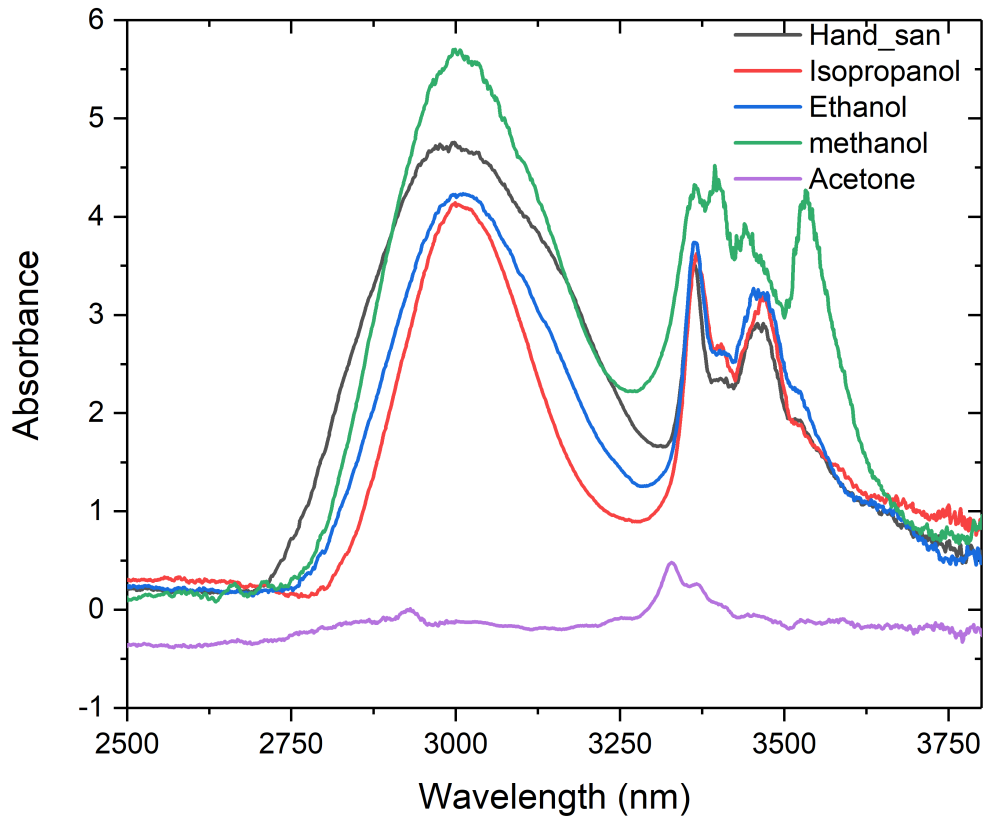


Figure A.6: Absorption measurement of commercial hand sanitizer (black), isopropanol (red), ethanol (blue), methanol (green), acetone (magenta)..

Bibliography

- [1] Christian Rosenberg Petersen et al. “Mid-infrared supercontinuum covering the 1.4–13.3 μm molecular fingerprint region using ultra-high NA chalcogenide step-index fibre.” In: *Nature Photonics* 8.11 (2014), page 830.
- [2] Christian Rosenberg Petersen et al. “Mid-infrared multispectral tissue imaging using a chalcogenide fiber supercontinuum source.” In: *Optics letters* 43.5 (2018), pages 999–1002.
- [3] Mohammed N Islam et al. “Femtosecond distributed soliton spectrum in fibers.” In: *JOSA B* 6.6 (1989), pages 1149–1158.
- [4] RR Alfano and SL Shapiro. “Emission in the region 4000 to 7000 \AA via four-photon coupling in glass.” In: *Physical Review Letters* 24.11 (1970), page 584.
- [5] PB Corkum, Claude Rolland, and T Srinivasan-Rao. “Supercontinuum generation in gases.” In: *Physical review letters* 57.18 (1986), page 2268.
- [6] Rasoul Raei, Majid Ebnali-Heidari, and Hamed Saghaei. “Supercontinuum generation in organic liquid-liquid core-cladding photonic crystal fiber in visible and near-infrared regions.” In: *JOSA B* 35.2 (2018), pages 323–330.
- [7] Kay Schaarschmidt et al. “Long-term stable supercontinuum generation and watt-level transmission in liquid-core optical fibers.” In: *Optics letters* 44.9 (2019), pages 2236–2239.
- [8] JC Knight et al. “All-silica single-mode optical fiber with photonic crystal cladding.” In: *Optics letters* 21.19 (1996), pages 1547–1549.
- [9] Philip Russell. “Photonic crystal fibers.” In: *science* 299.5605 (2003), pages 358–362.
- [10] Kyei Kwarkye et al. “In-amplifier and cascaded mid-infrared supercontinuum sources with low noise through gain-induced soliton spectral alignment.” In: *Scientific Reports* 10.1 (2020), pages 1–11.
- [11] Iván Bravo Gonzalo et al. “Polarization noise places severe constraints on coherence of all-normal dispersion femtosecond supercontinuum generation.” In: *Scientific reports* 8.1 (2018), pages 1–13.
- [12] Mariusz Klimczak et al. “Coherent supercontinuum generation up to 2.3 μm in all-solid soft-glass photonic crystal fibers with flat all-normal dispersion.” In: *Optics express* 22.15 (2014), pages 18824–18832.

- [13] Ramon A Martinez et al. “Mid-infrared supercontinuum generation from 1.6 to $> 11 \mu\text{m}$ using concatenated step-index fluoride and chalcogenide fibers.” In: *Optics letters* 43.2 (2018), pages 296–299.
- [14] John M Dudley, Goëry Genty, and Stéphane Coen. “Supercontinuum generation in photonic crystal fiber.” In: *Reviews of modern physics* 78.4 (2006), page 1135.
- [15] TA Birks, WJ Wadsworth, and P St J Russell. “Supercontinuum generation in tapered fibers.” In: *Optics letters* 25.19 (2000), pages 1415–1417.
- [16] NKT Photonics. *NKT: Supercontinuum lasers*. URL: <https://www.nktphotonics.com/lasers-fibers/product-category/supercontinuum-lasers/>. (accessed: 11.08.2020).
- [17] Weiqiang Yang et al. “High power all fiber mid-IR supercontinuum generation in a ZBLAN fiber pumped by a $2 \mu\text{m}$ MOPA system.” In: *Optics express* 21.17 (2013), pages 19732–19742.
- [18] Irnis Kubat et al. “Mid-infrared supercontinuum generation to $12.5 \mu\text{m}$ in large NA chalcogenide step-index fibres pumped at $4.5 \mu\text{m}$.” In: *Optics express* 22.16 (2014), pages 19169–19182.
- [19] Kyei Kwarkye et al. “Influence of pulse duration and repetition rate on mid-infrared cascaded supercontinuum.” In: *Optics Letters* 45.18 (2020), pages 5161–5164.
- [20] Benjamin J Eggleton, Barry Luther-Davies, and Kathleen Richardson. “Chalcogenide photonics.” In: *Nature photonics* 5.3 (2011), pages 141–148.
- [21] VS Shiryaev and MF Churbanov. “Trends and prospects for development of chalcogenide fibers for mid-infrared transmission.” In: *Journal of non-crystalline solids* 377 (2013), pages 225–230.
- [22] Guangming Tao et al. “Infrared fibers.” In: *Advances in Optics and Photonics* 7.2 (2015), pages 379–458.
- [23] Yi Yu et al. “ $1.8\text{--}10 \mu\text{m}$ mid-infrared supercontinuum generated in a step-index chalcogenide fiber using low peak pump power.” In: *Optics letters* 40.6 (2015), pages 1081–1084.
- [24] Irnis Kubat et al. “Thulium pumped mid-infrared $0.9\text{--}9 \mu\text{m}$ supercontinuum generation in concatenated fluoride and chalcogenide glass fibers.” In: *Optics express* 22.4 (2014), pages 3959–3967.
- [25] Chenan Xia et al. “Mid-infrared supercontinuum generation to $4.5 \mu\text{m}$ in ZBLAN fluoride fibers by nanosecond diode pumping.” In: *Optics letters* 31.17 (2006), pages 2553–2555.
- [26] Jacek Swiderski, Maria Michalska, and Gwenael Maze. “Mid-IR supercontinuum generation in a ZBLAN fiber pumped by a gain-switched mode-locked Tm-doped fiber laser and amplifier system.” In: *Optics express* 21.7 (2013), pages 7851–7857.

- [27] Mohammed N Islam. “Supercontinuum sources-all-fiber designs extend supercontinuum sources into the mid-ir region.” In: *Laser Focus World* 48.3 (2012), page 56.
- [28] Peter M Moselund et al. “Supercontinuum: broad as a lamp, bright as a laser, now in the mid-infrared.” In: *Laser Technology for Defense and Security VIII*. Volume 8381. International Society for Optics and Photonics. 2012, 83811A.
- [29] Christian Agger et al. “Nonlinear soliton matching between optical fibers.” In: *Optics letters* 36.13 (2011), pages 2596–2598.
- [30] Zhijian Zheng et al. “Scaling all-fiber mid-infrared supercontinuum up to 10 W-level based on thermal-spliced silica fiber and ZBLAN fiber.” In: *Photonics Research* 4.4 (2016), pages 135–139.
- [31] Ke Yin et al. “Highly stable, monolithic, single-mode mid-infrared supercontinuum source based on low-loss fusion spliced silica and fluoride fibers.” In: *Optics Letters* 41.5 (2016), pages 946–949.
- [32] G Stevens and T Woodbridge. “Development of low loss robust soft-glass fiber splices.” In: *Workshop on Specialty Optical Fibers and Their Applications*. Optical Society of America. 2013, W3–21.
- [33] U Møller and Ole Bang. “Intensity noise in normal-pumped picosecond supercontinuum generation, where higher-order Raman lines cross into anomalous dispersion regime.” In: *Electronics Letters* 49.1 (2013), pages 63–65.
- [34] DR Solli et al. “Optical rogue waves.” In: *Nature* 450.7172 (2007), page 1054.
- [35] Kristan L Corwin et al. “Fundamental noise limitations to supercontinuum generation in microstructure fiber.” In: *Physical review letters* 90.11 (2003), page 113904.
- [36] Rasmus Dybbro Engelsholm and Ole Bang. “Supercontinuum noise reduction by fiber undertapering.” In: *Optics express* 27.7 (2019), pages 10320–10331.
- [37] Simon Toft Sørensen et al. “The role of phase coherence in seeded supercontinuum generation.” In: *Optics express* 20.20 (2012), pages 22886–22894.
- [38] Jakob Kilgus et al. “Diffraction limited mid-infrared reflectance microspectroscopy with a supercontinuum laser.” In: *Optics express* 26.23 (2018), pages 30644–30654.
- [39] DR Solli et al. “Fluctuations and correlations in modulation instability.” In: *Nature Photonics* 6.7 (2012), page 463.
- [40] Benjamin Wetzal et al. “Real-time full bandwidth measurement of spectral noise in supercontinuum generation.” In: *Scientific reports* 2 (2012), page 882.
- [41] Romdhane Karoui, Gerard Downey, and Christophe Blecker. “Mid-infrared spectroscopy coupled with chemometrics: a tool for the analysis of intact food systems and the exploration of their molecular structure- quality relationships- a review.” In: *Chemical reviews* 110.10 (2010), pages 6144–6168.

- [42] Jan U Porep, Dietmar R Kammerer, and Reinhold Carle. "On-line application of near infrared (NIR) spectroscopy in food production." In: *Trends in Food Science & Technology* 46.2 (2015), pages 211–230.
- [43] Søren Balling Engelsen. "Near infrared spectroscopy—a unique window of opportunities." In: *NIR news* 27.5 (2016), pages 14–17.
- [44] Tony Woodcock, Gerard Downey, and Colm P O'Donnell. "Better quality food and beverages: the role of near infrared spectroscopy." In: *Journal of Near Infrared Spectroscopy* 16.1 (2008), pages 1–29.
- [45] Vincent Baeten and Pierre Dardenne. "Spectroscopy: developments in instrumentation and analysis." In: *Grasas y aceites* 53.1 (2002), pages 45–63.
- [46] Cristina Alamprese et al. "Detection of minced beef adulteration with turkey meat by UV–vis, NIR and MIR spectroscopy." In: *LWT-Food Science and Technology* 53.1 (2013), pages 225–232.
- [47] Walter Lindberg, Jan-Åke Persson, and Svante Wold. "Partial least-squares method for spectrofluorimetric analysis of mixtures of humic acid and lignin sulfonate." In: *Analytical Chemistry* 55.4 (1983), pages 643–648.
- [48] Graciela M Escandar et al. "A review of multivariate calibration methods applied to biomedical analysis." In: *Microchemical Journal* 82.1 (2006), pages 29–42.
- [49] Fangjun Kuang et al. "A novel SVM by combining kernel principal component analysis and improved chaotic particle swarm optimization for intrusion detection." In: *Soft Computing* 19.5 (2015), pages 1187–1199.
- [50] JE Jackson and A Edward. "User's guide to principal components. John Wiley Sons." In: *Inc., New York* (1991), page 40.
- [51] Christian R Petersen et al. "Towards a table-top synchrotron based on super-continuum generation." In: *Infrared Physics & Technology* 91 (2018), pages 182–186.
- [52] Wolfgang Demtröder. *Laser spectroscopy: basic concepts and instrumentation*. Springer Science & Business Media, 2013.
- [53] Fred O Libnau et al. "Spectra of water in the near-and mid-infrared region." In: *Vibrational spectroscopy* 7.3 (1994), pages 243–254.
- [54] Peter Snoer Jensen, Jimmy Bak, and Stefan Andersson-Engels. "Influence of temperature on water and aqueous glucose absorption spectra in the near-and mid-infrared regions at physiologically relevant temperatures." In: *Applied spectroscopy* 57.1 (2003), pages 28–36.
- [55] Lisa M Miller and Randy J Smith. "Synchrotrons versus globars, point-detectors versus focal plane arrays: Selecting the best source and detector for specific infrared microspectroscopy and imaging applications." In: *Vibrational spectroscopy* 38.1-2 (2005), pages 237–240.

- [56] AW Snyder and JD Love. "Optical Waveguide Theory Chapman and Hall." In: *New York* (1983), page 66.
- [57] Correspondent Jeff Hecht and Jeff Hecht. *City of light: the story of fiber optics*. Oxford University Press on Demand, 1999.
- [58] John A Buck. *Fundamentals of optical fibers*. Volume 50. John Wiley & Sons, 2004.
- [59] Govind P Agrawal. *Nonlinear Fiber Optics [recurso Electrónico] c*. Academic, 2013.
- [60] Niels Asger Mortensen et al. "Modal cutoff and the V parameter in photonic crystal fibers." In: *Optics letters* 28.20 (2003), pages 1879–1881.
- [61] Tim A Birks, Jonathan C Knight, and P St J Russell. "Endlessly single-mode photonic crystal fiber." In: *Optics letters* 22.13 (1997), pages 961–963.
- [62] D Mogilevtsev, Tim A Birks, and P St J Russell. "Group-velocity dispersion in photonic crystal fibers." In: *Optics Letters* 23.21 (1998), pages 1662–1664.
- [63] L Cohen. "Comparison of single-mode fiber dispersion measurement techniques." In: *Journal of lightwave technology* 3.5 (1985), pages 958–966.
- [64] Shreesha Rao DS et al. "Ultra-low-noise supercontinuum generation with a flat near-zero normal dispersion fiber." In: *Optics letters* 44.9 (2019), pages 2216–2219.
- [65] Karen Marie Hilligsøe et al. "Supercontinuum generation in a photonic crystal fiber with two zero dispersion wavelengths." In: *Optics Express* 12.6 (2004), pages 1045–1054.
- [66] Stephen B Alexander. *Optical communication receiver design*. 37. IET, 1997.
- [67] Katsusuke Tajima et al. "Ultralow loss and long length photonic crystal fiber." In: *Journal of Lightwave Technology* 22.1 (2004), page 7.
- [68] Tengchao Huang et al. "Study on thermal splicing of ZBLAN fiber to silica fiber." In: *Optical Engineering* 55.10 (2016), page 106119.
- [69] Andrew D Yablon and Ryan T Bise. "Low-loss high-strength microstructured fiber fusion splices using GRIN fiber lenses." In: *IEEE Photonics Technology Letters* 17.1 (2004), pages 118–120.
- [70] Zheng Zhi-Jian et al. "An effective thermal splicing method to join fluoride and silica fibers for a high power regime." In: *Chinese Physics Letters* 32.11 (2015), page 114206.
- [71] E Snitzer. "Proposed fiber cavities for optical masers." In: *Journal of Applied Physics* 32.1 (1961), pages 36–39.
- [72] Charles J Koester and Elias Snitzer. "Amplification in a fiber laser." In: *Applied optics* 3.10 (1964), pages 1182–1186.
- [73] Michel JF Dignonnet. *Rare-earth-doped fiber lasers and amplifiers, revised and expanded*. CRC press, 2001.

- [74] Brian G Wybourne and Lidia Smentek. *Optical spectroscopy of lanthanides: magnetic and hyperfine interactions*. CRC press, 2007.
- [75] B James Ainslie. “A review of the fabrication and properties of erbium-doped fibers for optical amplifiers.” In: *Journal of Lightwave Technology* 9.2 (1991), pages 220–227.
- [76] JL Wagener et al. “Effects of concentration and clusters in erbium-doped fiber lasers.” In: *Optics letters* 18.23 (1993), pages 2014–2016.
- [77] HW Gandy, RJ Ginther, and JF Weller. “Stimulated emission of Tm³⁺ radiation in silicate glass.” In: *Journal of Applied Physics* 38.7 (1967), pages 3030–3031.
- [78] J Sanz, R Cases, and R Alcalá. “Optical properties of Tm³⁺ in fluorozirconate glass.” In: *Journal of Non-Crystalline Solids* 93.2-3 (1987), pages 377–386.
- [79] WL Barnes and JE Townsend. “Highly tunable and efficient diode pumped operation of Tm³⁺ doped fibre lasers.” In: *Electronics letters* 26.11 (1990), pages 746–747.
- [80] DC Hanna et al. “Efficient and tunable operation of a Tm-doped fibre laser.” In: *Optics Communications* 75.3-4 (1990), pages 283–286.
- [81] RW Hellwarth. “Third-order optical susceptibilities of liquids and solids.” In: *Progress in Quantum Electronics* 5 (1977), pages 1–68.
- [82] TK Gustafson et al. “Self-modulation, self-steepening, and spectral development of light in small-scale trapped filaments.” In: *Physical Review* 177.1 (1969), page 306.
- [83] Fujio Shimizu. “Frequency broadening in liquids by a short light pulse.” In: *Physical Review Letters* 19.19 (1967), page 1097.
- [84] YR Shen and Michael MT Loy. “Theoretical interpretation of small-scale filaments of light originating from moving focal spots.” In: *Physical Review A* 3.6 (1971), page 2099.
- [85] SA Akhmanov, RV Khokhlov, and AP Sukhorukov. “Laser Handbook, vol. 2.” In: *Eds FT Arecchi, EO Schulz-Dubois, Amsterdam: North-Holland* (1972).
- [86] RW Boyd and BR Masters. “Nonlinear Optics 3rd edn (New York: Academic).” In: (2008).
- [87] JA Armstrong et al. “Interactions between light waves in a nonlinear dielectric.” In: *Physical review* 127.6 (1962), page 1918.
- [88] M Schubert and B Wilhelmi. *Nonlinear optics and quantum electronics*. 1986.
- [89] R Stolen. “Phase-matched-stimulated four-photon mixing in silica-fiber waveguides.” In: *IEEE Journal of Quantum Electronics* 11.3 (1975), pages 100–103.
- [90] VI Karpman. “Self-modulation of nonlinear plane waves in dispersive media.” In: *JETPL* 6 (1967), page 277.

- [91] VI Bespalov and VI Talanov. “Filamentary structure of light beams in nonlinear liquids.” In: *JETPL* 3 (1966), page 307.
- [92] Dan Anderson and Mietek Lisak. “Modulational instability of coherent optical-fiber transmission signals.” In: *Optics letters* 9.10 (1984), pages 468–470.
- [93] B Hermansson and D Yevick. “Modulational instability effects in PSK modulated coherent fiber systems and their reduction by optical loss.” In: *Optics communications* 52.2 (1984), pages 99–102.
- [94] Mohammed N Islam, SP Dijaili, and James P Gordon. “Modulation-instability-based fiber interferometer switch near 1.5 μm .” In: *Optics letters* 13.6 (1988), pages 518–520.
- [95] Victor A Vysloukh and NA Sukhotskova. “Influence of third-order dispersion on the generation of a train of picosecond pulses in fiber waveguides due to self-modulation instability.” In: *Soviet Journal of Quantum Electronics* 17.11 (1987), page 1509.
- [96] Chandrasekhara Venkata Raman. “A new radiation.” In: (1928).
- [97] E Woodbury and W Nag. “First demonstration of stimulated Raman scattering.” In: *Proc. IRE* 50.6 (1962), page 2347.
- [98] J Herrmann et al. “Experimental evidence for supercontinuum generation by fission of higher-order solitons in photonic fibers.” In: *Physical Review Letters* 88.17 (2002), page 173901.
- [99] P Beaud et al. “Ultrashort pulse propagation, pulse breakup, and fundamental soliton formation in a single-mode optical fiber.” In: *IEEE journal of quantum electronics* 23.11 (1987), pages 1938–1946.
- [100] C Lafargue et al. “Direct detection of optical rogue wave energy statistics in supercontinuum generation.” In: *Electronics Letters* 45.4 (2009), pages 217–219.
- [101] Simon Toft Sørensen et al. “Describing supercontinuum noise and rogue wave statistics using higher-order moments.” In: *Optics Communications* 285.9 (2012), pages 2451–2455.
- [102] Mengjie Yu et al. “Mode-locked mid-infrared frequency combs in a silicon microresonator.” In: *Optica* 3.8 (2016), pages 854–860.
- [103] Albert Schliesser, Nathalie Picqué, and Theodor W Hänsch. “Mid-infrared frequency combs.” In: *Nature photonics* 6.7 (2012), page 440.
- [104] Günter Steinmeyer and Julia S Skibina. “Supercontinua: Entering the mid-infrared.” In: *Nature Photonics* 8.11 (2014), page 814.
- [105] Maria Maragkou. “Supercontinuum: Reaching the mid-infrared.” In: *Nature Photonics* 8.10 (2014), page 746.
- [106] Neetesh Singh et al. “Midinfrared supercontinuum generation from 2 to 6 μm in a silicon nanowire.” In: *Optica* 2.9 (2015), pages 797–802.

-
- [107] Darren D Hudson et al. “Toward all-fiber supercontinuum spanning the mid-infrared.” In: *Optica* 4.10 (2017), pages 1163–1166.
- [108] Sergey Vasilyev et al. “Super-octave longwave mid-infrared coherent transients produced by optical rectification of few-cycle 2.5- μm pulses.” In: *Optica* 6.1 (2019), pages 111–114.
- [109] Steven A Miller et al. “Low-loss silicon platform for broadband mid-infrared photonics.” In: *Optica* 4.7 (2017), pages 707–712.
- [110] Tine Ringsted et al. “Near-infrared spectroscopy using a supercontinuum laser: application to long wavelength transmission spectra of barley endosperm and oil.” In: *Applied spectroscopy* 70.7 (2016), pages 1176–1185.
- [111] Jeff Chiles et al. “Multi-functional integrated photonics in the mid-infrared with suspended AlGaAs on silicon.” In: *arXiv preprint arXiv:1905.01380* (2019).
- [112] Christian Rosenberg Petersen et al. “Spectral-temporal composition matters when cascading supercontinua into the mid-infrared.” In: *Optics Express* 24.2 (2016), pages 749–758.
- [113] Christian Agger et al. “Supercontinuum generation in ZBLAN fibers—detailed comparison between measurement and simulation.” In: *JOSA B* 29.4 (2012), pages 635–645.
- [114] Uffe Møller et al. “Power dependence of supercontinuum noise in uniform and tapered PCFs.” In: *Optics express* 20.3 (2012), pages 2851–2857.
- [115] DR Solli, C Ropers, and B Jalali. “Active control of rogue waves for stimulated supercontinuum generation.” In: *Physical review letters* 101.23 (2008), page 233902.
- [116] Simon Toft Sørensen et al. “Influence of pump power and modulation instability gain spectrum on seeded supercontinuum and rogue wave generation.” In: *JOSA B* 29.10 (2012), pages 2875–2885.
- [117] Michael Maria et al. “Q-switch-pumped supercontinuum for ultra-high resolution optical coherence tomography.” In: *Optics letters* 42.22 (2017), pages 4744–4747.
- [118] Johan Hult, Rosalynne S Watt, and Clemens F Kaminski. “High bandwidth absorption spectroscopy with a dispersed supercontinuum source.” In: *Optics express* 15.18 (2007), pages 11385–11395.
- [119] Mariusz Klimczak et al. “Direct comparison of shot-to-shot noise performance of all normal dispersion and anomalous dispersion supercontinuum pumped with sub-picosecond pulse fiber-based laser.” In: *Scientific reports* 6 (2016), page 19284.
- [120] Anupamaa Rampur et al. “Ultra low-noise coherent supercontinuum amplification and compression below 100 fs in an all-fiber polarization-maintaining thulium fiber amplifier.” In: *Optics Express* 27.24 (2019), pages 35041–35051.

- [121] A Kudlinski et al. “Control of pulse-to-pulse fluctuations in visible supercontinuum.” In: *Optics express* 18.26 (2010), pages 27445–27454.
- [122] Jacob Ramsay, S Dupont, and S R Keiding. “Pulse-to-pulse noise reduction in infrared supercontinuum spectroscopy: polarization and amplitude fluctuations.” In: *Laser Physics Letters* 11.9 (2014), page 095702.
- [123] Carsten Thirstrup, Yuan Shi, and Bera Palsdottir. “Pump-induced refractive index modulation and dispersions in Er/sup 3+/-doped fibers.” In: *Journal of lightwave technology* 14.5 (1996), pages 732–738.
- [124] Bahaa EA Saleh and Malvin Carl Teich. *Fundamentals of photonics*. John Wiley & Sons, 2019.
- [125] Shaoxiang Chen et al. “Ultra-short wavelength operation of thulium-doped fiber amplifiers and lasers.” In: *Optics Express* 27.25 (2019), pages 36699–36707.
- [126] Dean E McCumber. “Theory of phonon-terminated optical masers.” In: *Physical review* 134.2A (1964), A299.
- [127] Bernard Dussardier, Wilfried Blanc, and Pavel Peterka. “Tailoring of the local environment of active ions in rare-earth-and transition-metal-doped optical fibres, and potential applications.” In: *Selected Topics on Optical Fiber Technology*. IntechOpen, 2012.
- [128] Guillaume Canat et al. “Dynamics of high-power erbium–ytterbium fiber amplifiers.” In: *JOSA B* 22.11 (2005), pages 2308–2318.
- [129] Andrew Malinowski, Jonathan HV Price, and Michalis N Zervas. “Overlapped pulsed pumping of tandem pumped fiber amplifiers to increase achievable pulse energy.” In: *IEEE Journal of Quantum Electronics* 53.2 (2017), pages 1–8.
- [130] Miroslav Kolesik, Ewan M Wright, and Jerome V Moloney. “Simulation of femtosecond pulse propagation in sub-micron diameter tapered fibers.” In: *Applied Physics B* 79.3 (2004), pages 293–300.
- [131] Etienne Genier et al. “Amplitude noise and coherence degradation of femtosecond supercontinuum generation in all-normal-dispersion fibers.” In: *JOSA B* 36.2 (2019), A161–A167.
- [132] Pavel Peterka et al. “Theoretical modeling of fiber laser at 810 nm based on thulium-doped silica fibers with enhanced 3 H 4 level lifetime.” In: *Optics express* 19.3 (2011), pages 2773–2781.
- [133] Niels M Israelsen et al. “Real-time high-resolution mid-infrared optical coherence tomography.” In: *Light: Science & Applications* 8.1 (2019), page 11.
- [134] Niels Møller Israelsen et al. “The value of ultrahigh resolution OCT in dermatology-delineating the dermo-epidermal junction, capillaries in the dermal papillae and vellus hairs.” In: *Biomedical optics express* 9.5 (2018), pages 2240–2265.

- [135] Malay Kumar et al. “Stand-off detection of solid targets with diffuse reflection spectroscopy using a high-power mid-infrared supercontinuum source.” In: *Applied Optics* 51.15 (2012), pages 2794–2807.
- [136] Manoj Kumar Dasa et al. “High-pulse energy supercontinuum laser for high-resolution spectroscopic photoacoustic imaging of lipids in the 1650-1850 nm region.” In: *Biomedical optics express* 9.4 (2018), pages 1762–1770.
- [137] Manoj Kumar Dasa et al. “Multispectral photoacoustic sensing for accurate glucose monitoring using a supercontinuum laser.” In: *JOSA B* 36.2 (2019), A61–A65.
- [138] Hoa Phuoc Trung Nguyen et al. “Highly coherent supercontinuum in the mid-infrared region with cascaded tellurite and chalcogenide fibers.” In: *Applied optics* 57.21 (2018), pages 6153–6163.
- [139] Maria Michalska et al. “Mid-infrared, super-flat, supercontinuum generation covering the 2–5 μm spectral band using a fluoroindate fibre pumped with picosecond pulses.” In: *Scientific reports* 6 (2016), page 39138.
- [140] NV Kiritchenko et al. “Effect of ytterbium co-doping on erbium clustering in silica-doped glass.” In: *Laser Physics* 25.2 (2015), page 025102.
- [141] AA Popov et al. “Powerful mid-infrared light emitting diodes for pollution monitoring.” In: *Electronics Letters* 33.1 (1997), pages 86–88.
- [142] Khalil Eslami Jahromi et al. “Mid-infrared supercontinuum-based upconversion detection for trace gas sensing.” In: *Optics Express* 27.17 (2019), pages 24469–24480.
- [143] RH Wilson and HS Tapp. “Mid-infrared spectroscopy for food analysis: recent new applications and relevant developments in sample presentation methods.” In: *TrAC Trends in Analytical Chemistry* 18.2 (1999), pages 85–93.
- [144] Ramon A Martinez et al. “Active mid-wave to long-wave supercontinuum FTIR sensor for standoff chemical detection.” In: *Journal of Lightwave Technology* 37.14 (2019), pages 3626–3636.
- [145] Angela B Seddon. “Mid-infrared (IR)—A hot topic: The potential for using mid-IR light for non-invasive early detection of skin cancer in vivo.” In: *physica status solidi (b)* 250.5 (2013), pages 1020–1027.
- [146] Sune Dupont et al. “IR microscopy utilizing intense supercontinuum light source.” In: *Optics express* 20.5 (2012), pages 4887–4892.
- [147] Mingjie Zhang et al. “Mid-infrared supercontinuum generation in chalcogenide fibers with high laser damage threshold.” In: *Optics express* 27.20 (2019), pages 29287–29296.
- [148] Tonglei Cheng et al. “Mid-infrared supercontinuum generation spanning 2.0 to 15.1 μm in a chalcogenide step-index fiber.” In: *Optics letters* 41.9 (2016), pages 2117–2120.

- [149] Zheming Zhao et al. “1.5–14 μm midinfrared supercontinuum generation in a low-loss Te-based chalcogenide step-index fiber.” In: *Optics letters* 41.22 (2016), pages 5222–5225.
- [150] Christian Rosenberg Petersen et al. “Increased mid-infrared supercontinuum bandwidth and average power by tapering large-mode-area chalcogenide photonic crystal fibers.” In: *Optics express* 25.13 (2017), pages 15336–15348.
- [151] Uffe Møller et al. “Multi-milliwatt mid-infrared supercontinuum generation in a suspended core chalcogenide fiber.” In: *Optics express* 23.3 (2015), pages 3282–3291.
- [152] Christopher L Hagen, Joachim W Walewski, and Scott T Sanders. “Generation of a continuum extending to the midinfrared by pumping ZBLAN fiber with an ultrafast 1550-nm source.” In: *IEEE Photonics Technology Letters* 18.1 (2005), pages 91–93.
- [153] Sébastien Venck et al. “2–10 μm Mid-Infrared Fiber-Based Supercontinuum Laser Source: Experiment and Simulation.” In: *Laser & Photonics Reviews* (2020), page 2000011.
- [154] Deepak Jain et al. “Record power, ultra-broadband supercontinuum source based on highly GeO₂ doped silica fiber.” In: *Optics express* 24.23 (2016), pages 26667–26677.
- [155] EJ Milton. “Review article principles of field spectroscopy.” In: *Remote Sensing* 8.12 (1987), pages 1807–1827.
- [156] Frank A DeThomas and Paul J Brimmer. “Monochromators for Near-Infrared Spectroscopy.” In: *Handbook of vibrational spectroscopy* (2006).
- [157] Lidia Esteve Agelet and Charles R Hurburgh Jr. “A tutorial on near infrared spectroscopy and its calibration.” In: *Critical Reviews in Analytical Chemistry* 40.4 (2010), pages 246–260.
- [158] Lidia Esteve Agelet and Charles R Hurburgh Jr. “Limitations and current applications of Near Infrared Spectroscopy for single seed analysis.” In: *Talanta* 121 (2014), pages 288–299.
- [159] Carsten Kötting, Jörn Güldenhaupt, and Klaus Gerwert. “Time-resolved FTIR spectroscopy for monitoring protein dynamics exemplified by functional studies of Ras protein bound to a lipid bilayer.” In: *Chemical Physics* 396 (2012), pages 72–83.
- [160] NJ Harrick. “Surface chemistry from spectral analysis of totally internally reflected radiation.” In: *The Journal of Physical Chemistry* 64.9 (1960), pages 1110–1114.
- [161] J Fahrenfort. “Attenuated total reflection: A new principle for the production of useful infra-red reflection spectra of organic compounds.” In: *Spectrochimica Acta* 17.7 (1961), pages 698–709.

-
- [162] NJ Harrick. “Electric field strengths at totally reflecting interfaces.” In: *JOSA* 55.7 (1965), pages 851–857.
- [163] Milan Milosevic. “Internal reflection and ATR spectroscopy.” In: *Applied Spectroscopy Reviews* 39.3 (2004), pages 365–384.
- [164] DTF Marple. “Refractive index of ZnSe, ZnTe, and CdTe.” In: *Journal of Applied Physics* 35.3 (1964), pages 539–542.
- [165] George M Hale and Marvin R Query. “Optical constants of water in the 200-nm to 200- μ m wavelength region.” In: *Applied optics* 12.3 (1973), pages 555–563.